Evaluation of Zero-Dimensional Furnace Models for Biomass-Fired Boilers with the Aid of CFD and Plant Measurements

Prepared by:

Tinashe Kadakure

KDKTIN001

Department of Mechanical Engineering

University of Cape Town

Supervisor:

Professor Pieter Rousseau

Co-Supervisor:

Professor Ryno Laubscher

4 November 2024

Submitted to the Department of Mechanical Engineering at the University of Cape Town in partial fulfilment of the academic requirements for a Master of Science degree in Mechanical Engineering.

University of Cape Town

The copyright of this thesis vests in the author. No quotation from it or information derived from it is to be published without full acknowledgement of the source. The thesis is to be used for private study or non-commercial research purposes only.

Published by the University of Cape Town (UCT) in terms of the non-exclusive license granted to UCT by the author.

University of Cape Town

Plagiarism Declaration

I know the meaning of plagiarism and declare that all the work in the document, except for that which is properly acknowledged, is my own. This thesis/dissertation has been submitted to the Turnitin module, and I confirm that my supervisor has seen my report, and any concerns raised by the report have been addressed with my supervisor.

Document Author:		
Surname	**Name**	**Student Number**
Kadakure	Tinashe	KDKTIN001

Date	4 November 2024
Signature	Signed by candidate

Acknowledgements

I would like to express gratitude to my supervisors, Prof. Pieter Rousseau and Prof. Ryno Laubscher. Their unwavering support and insightful guidance throughout this entire project were truly invaluable. The depth of knowledge I gained from both of them profoundly shaped my research journey. Their mentorship not only contributed to the success of this project but also inspired me to push the boundaries of my potential.

I am grateful to my parents for their unwavering support during my studies and their continuous encouragement. Their love and belief in me served as a constant source of strength, motivating me to keep striving for excellence.

I am grateful to the ATProM research unit for their valuable contributions, which greatly enriched my research experience. It was a true privilege to be surrounded by such dedicated and talented individuals. Their willingness to engage in discussions and provide feedback created a supportive environment that significantly enhanced my learning and growth throughout this journey.

A special thanks goes to John Thompson for providing essential data on the boilers and for their financial support for this project. I would also like to extend my appreciation to MerSETA, the Dutkiewicz family, and the John Davidson Educational Trust for their financial support. Completing my studies would not have been possible without their support.

Lastly, and most importantly, I give thanks to the Lord Almighty for this incredible master's experience and for granting me the strength to work hard and persevere.

Abstract

Biomass combustion is an important and renewable source of energy, and its efficient utilisation has become an area of active research. Modelling biomass boilers is critical for optimising their design, performance, and control. A key challenge is accurately predicting waterwall heat uptake, furnace exit gas temperature (FEGT), and direct radiation impinging on downstream heat exchangers under varying operational conditions.

Although radiation heat transfer is highly dependent on three-dimensional geometry, one-dimensional process models that integrate zero-dimensional (0-D) furnace models are commonly used to predict boiler performance. 0-D models simplify complex systems by representing the furnace as a single control volume with averaged properties, rather than capturing spatial variations. These 0-D furnace models are typically based on a combination of fundamental and empirical relationships. However, it has been shown that the existing empirical relationships may not always capture the furnace performance with sufficient accuracy.

This study evaluates the predictive accuracy of two widely used 0-D semi-empirical furnace models, the direct method (Hottel) and the projected method (Gurvich/Blokh). These 0-D models were originally developed for large coal-fired boilers, and they are often applied to biomass-fired boilers without a thorough evaluation of their performance.

To address this gap, two case studies were conducted on a compact biomass-fired boiler and an industrial biomass-fired boiler, with steam flows of 45 t/h and 105 t/h, respectively. The accuracy of the 0-D furnace models was evaluated by comparing their predictions to validated CFD simulations at both full and reduced loads. Key performance indicators, including waterwall heat uptake and FEGT, were analysed to evaluate the predictive accuracy of the 0-D models.

For the smaller boiler, the 0-D models exhibited limitations in accurately predicting radiation heat transfer, especially at reduced loads. Although the projected method outperformed the direct method in some cases, neither model accurately captured the performance of the smaller boiler. In contrast, for the larger boiler, the direct method predicted waterwall heat uptake within 5.1% of the CFD results at full and reduced loads. The projected method, while exhibiting limitations in predicting waterwall heat uptake, performed better in predicting the FEGT, with errors of less than 5.4% across all load conditions.

This study highlights the limitations of 0-D furnace models when applied to biomass-fired boilers, particularly for smaller boilers and under reduced load conditions. This emphasises the need to refine these models for broader applicability beyond large coal-fired boilers.

Table of Contents

List of Figures

List of Tables

List of Nomenclature

General symbols

Symbol	Description	Units		Symbol	Description	Units
A	Area	m^2		n	Mole fractions	mol/mol_f
B_o	Boltzmann number	-		$\dot{Q}$	Heat transfer rate	W
c_p	Specific heat capacity	J/kg·K		r	Volume fraction	-
d_p	Particle (fly ash) diameter	µm		R	Thermal resistance	K/W
h	Enthalpy	J/kg		S	Mean beam length	m
h_i	Heat transfer coefficient	$W/m^2·K$		T	Temperature	K
k	Thermal conductivity	W/m·K		$\overline{VC}$	Overall heat capacity	J/kg·K
M	Molar mass	kg/mol		x	Angular coefficient	-
M_{fl}	Flame modification factor	-		X	Mole fraction	-
$\dot{m}$	Mass Flow Rate	kg/s		Y	Mass fraction	kg/kg_f

Greek symbols

Symbol	Description	Units		Symbol	Description	Units
α	Excess air ratio	-		ε	Emissivity	-
ψ	Furnace efficiency factor	-		$\propto$	Absorptivity	-
φ	Heat preservation coefficient	-		ϕ	Optical thickness	-
η	Non-uniformity factor	-		β	Reradiation factor	-
ξ	Fouling factor	m^2K/W		ρ	Density	kg/m^3
σ_o	Stefan-Boltzmann Constant	W/m^2K^4		w	Specific Humidity	kg/kg_a

Subscripts

Subscript	Description		Subscript	Description
aft	Adiabatic flame temperature		hx	Heat exchanger
ba	Bottom ash		ms_e	Main steam exit
ca	Combustion air		p	Products
da	Distribution air (spreader air)		pa	Primary air
f	Fuel		r	Reactants
fa	Fly ash		rad	Radiation
fe	Furnace exit		react	Reaction (combustion)
fg	Flue gas		rf	Refractory
fw_i	Feed water inlet		sa	Secondary air
fur	Furnace		w	Wall (furnace)
gp	Gas-particle suspension		ww	Waterwall)

Acronyms and abbreviations

Acronym	Description		Acronym	Description
AFR	Air-fuel ratio		HHV	Higher heating value
AF	Ash free		LCV	Lower calorific value
AR	As received		M	Moisture
CFD	Computational fluid dynamics		UA	Overall heat transfer coefficient
DPM	Discrete phase model		UC	Unburnt carbon
FEGT	Furnace exit gas temperature		0-D	Zero-dimensional
FGR	Flue gas ratio		1-D	One-dimensional

1. Introduction

1.1 Background

Biomass is an important and renewable source of energy, and its efficient utilisation is an area of active research [1]. As the world aims to reduce its carbon footprint and transition to renewable energy sources, biomass boilers are seen as a key technology in achieving these goals. Biomass boilers use organic materials such as wood and agricultural residues to generate heat and electricity, which can be a sustainable and renewable alternative to fossil fuels [1]. Biomass is particularly relevant in regions like Africa, where biofuels and waste make up a significant portion of the energy supply. Figure 1.1 shows that biofuels and waste contribute substantially to the overall energy supply, especially in Africa, where they are the dominant energy source. This makes biomass boilers a promising solution for renewable energy generation in these areas.

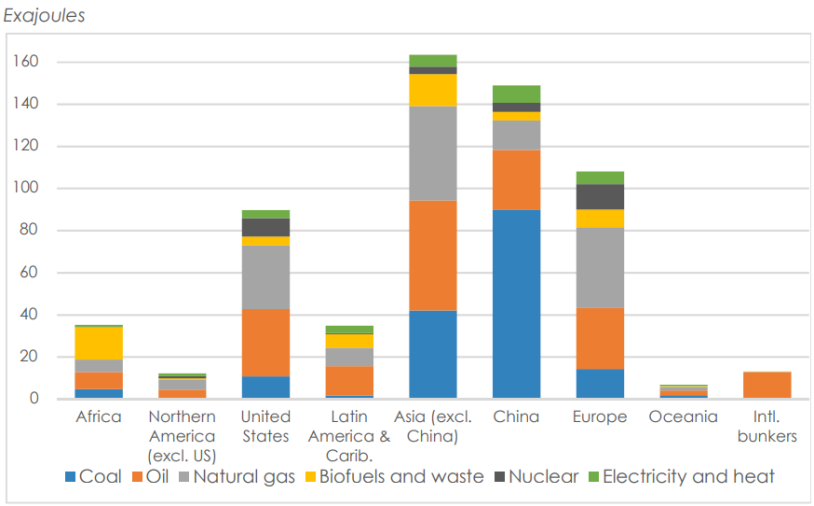

Figure 1.1: *Total energy supply by source, 2019 [2].*

Modelling of biomass boilers is an important tool used in the design, optimisation, and control of the system. The models can be used to make predictions about the performance of the system under different operating conditions, identify potential problems or areas for improvement, and optimise the efficiency and emission of the system [3]. Accurate modelling is especially important for predicting key performance parameters such as waterwall heat uptake, furnace exit gas temperature (FEGT), and the direct radiation impinging on the downstream radiant heat exchangers. These factors directly impact the thermal efficiency of the boiler and overall reliability, making them important in both the design and operation phases.

Three dimensional (3-D) CFD simulations are widely recognised for their ability to provide detailed insights into the flow and combustion processes occurring within a boiler, enabling accurate

predictions of the performance of the boiler. However, the detailed nature of CFD simulations presents a significant drawback: they require extensive computational resources and long processing times, often ranging from several hours to days, depending on the complexity of the model and specifications of the available hardware [3, 4]. Although computational power is becoming more affordable, the inherent complexity of CFD simulations still demands significant investments in both hardware and time. This complexity renders them unsuitable for rapid design iterations and real-time analysis. As a result, their practical application for biomass boiler design and optimisation is often limited. To reduce the costs and the time needed to carry out the simulations, different numerical tools for combustion behaviour analysis are becoming popular with the advances of computational resources and technologies [3].

A viable alternative for simulating the behaviour of biomass boilers is the use of one-dimensional (1-D) process models that integrate zero-dimensional (0-D) furnace models. Even as computational power becomes less expensive, 1-D models that integrate 0-D furnace models will remain highly useful for comparing with CFD models, particularly during the design phase when validation data may not be accessible.

In biomass boilers, radiation heat transfer dominates in the furnace and since it is highly dependent on 3-D geometry, cannot readily be reduced to lower-dimensional analyses. Despite this complexity, 0-D furnace models are integrated into 1-D process models to predict furnace performance. The 1-D model captures variations along a single dimension in temperature, pressure, and concentration, while the 0-D model represents the furnace as a single control volume, accounting for complex radiative heat transfer and turbulent combustion, where spatial resolution is impractical. These 0-D models significantly influence the accuracy of both steady-state and dynamic integrated system performance.

The 0-D furnace models are typically based on empirical correlations that simplify the relationships between key factors such as fuel properties, boiler design parameters, and operating conditions [3, 5]. By leveraging these correlations, 0-D models offer a more efficient means of predicting boiler performance without the computational demands of full-scale CFD simulations. However, the empirical correlations used in 0-D models are derived from limited datasets, and may not fully capture the variability and complexity of biomass fuels [5].

Two prominent 0-D semi-empirical furnace models are the direct method (Hottel) [5-7] and the projected method (Gurvich/Blokh) [7, 8]. These models were originally developed for large coal-fired boilers and are frequently applied to biomass-fired boilers without sufficient validation of their performance in this context. This practice can lead to significant uncertainties in one-dimensional process models that integrate 0-D furnace models. Therefore, there is a need to evaluate the uncertainties associated with these 0-D furnace models.

1.2 Research Aim

The aim of this research is to evaluate the impact of existing empirical correlations on the accuracy and uncertainty of 0-D furnace models applied to biomass boilers, specifically focusing on the direct and the projected methods. This will be accomplished through the use of Python-based 0-D models, detailed 3-D CFD simulations, and available site measurements. The study will focus on two case study boilers, Microgen-X and Ubombo, both of which are semi-suspension biomass-fired water tube boilers. These boilers feature distinct geometries, allowing for a comparative analysis of model performance across varying design configurations.

Furthermore, the research aims to assess the sensitivity of the 0-D furnace models to the empirical correlations and input parameters employed in their implementation. By identifying the specific parameters that significantly influence the models and contribute to variability in their predictions, this study will provide insights into the limitations and strengths of current modelling approaches. Although not included within the scope of this study, the findings will inform the development of more accurate and reliable 1-D process models that integrate 0-D furnace models, thereby enabling their confident application in the design, optimisation, and analysis of biomass boiler systems.

1.3 Research Questions

The specific research questions that this research intends to answer are the following:

a) How well do 0-D furnace models predict key performance indicators such as waterwall heat uptake and FEGT in biomass boilers, when compared to CFD simulation results?
b) What are the key sources of uncertainty in the 0-D furnace models, and how do they affect the accuracy of predictions?
c) What empirical correlations are employed in 0-D furnace models, and how do these correlations influence the accuracy and applicability of the models across different boiler sizes and operating conditions?
d) How sensitive are 0-D furnace models to variations in key empirical correlations and input parameters, and how does this affect model accuracy for heat transfer predictions?
e) How robust are the 0-D models when subjected to sensitivity analysis, and what does this reveal about their reliability for biomass boiler applications under varying load conditions?
f) What limitations do 0-D furnace models exhibit based on comparisons with CFD simulation results, and what are the potential areas for future research to improve these models for biomass-fired boiler applications

1.4 Objectives

The objectives of this research are:

A) To develop 0-D furnace models in Python of the Ubombo case study boiler using the existing MicroGen-X model as a framework. The Python model will include the direct and projected methods.

B) To analyse and compare results from existing CFD simulations of the MicroGen-X and Ubombo boilers with the data generated by the Python-based 0-D furnace models. This comparison will focus on key performance metrics such as the waterwall heat uptake and FEGT across different operational loads.

C) To quantify the uncertainty in the 0-D furnace models by comparing their results with the CFD models, and actual measurements where these are available.

D) To evaluate and compare the performance of the different semi-empirical correlations utilised in the 0-D models to determine which correlations yields the most accurate predictions for biomass boiler operations.

E) To conduct a sensitivity analysis on the 0-D furnace models to identify which input parameters significantly affect model predictions and contribute to variability, thus informing potential refinements to the modelling approach.

F) To identify the limitations of the 0-D models based on the comparison with CFD results and propose recommendations for future research aimed at improving the accuracy and applicability of these models for biomass boiler systems.

1.5 Report Roadmap

This report is organised into six chapters, each building upon the previous to provide a comprehensive analysis and discussion of the boiler case studies. The structure of the report is as follows:

a) The next chapter, Chapter 2, reviews the existing body of knowledge relevant to the study, covering previous research, theoretical frameworks, and key concepts related to boiler systems. The review highlights gaps in the current literature and establishes the context for the present study.
b) Chapter 3 outlines the development of the Python model, presenting the relevant theoretical frameworks and equations.
c) Chapter 4 presents a detailed case study of the two biomass-fired boilers under investigation. It provides an in-depth analysis of the design of the boilers, operation, and performance metrics.
d) Chapter 5 details the CFD modelling approach, including its validation using site data for both full-load and reduced-load conditions, as well as the post-processing techniques employed for data analysis.
e) Chapter 6 presents the findings from the case studies and interprets these results in the context of the research objectives.
f) The final chapter, Chapter 7, synthesises the findings and provides recommendations based on the study.

2. Literature Review

The objective of this literature review is to present an overview of existing research and establish the necessary framework to inform the current study. Specifically, the focus of this review is to explore the application of a 1-D process modelling approach to water-tube boilers, with a particular emphasis on employing a 0-D methodology for furnace heat transfer. It is worth noting that the existing literature on biomass modelling tends to focus on specific aspects of boiler systems, such as firing mechanisms, emissions, and fouling. Consequently, there is limited availability of papers that provide complete models for biomass-fired boilers. Considering this, the review will primarily draw upon the extensive literature on solid fuel boilers, which follows a similar fundamental procedure with only minor variations that will be discussed in subsequent chapters. By synthesising existing research and highlighting key findings, the review aims to contribute to the knowledge base in this area and provide a useful resource for researchers and practitioners working on boiler system analysis and optimisation.

2.1 Modelling Techniques for Boilers

The utilisation of modelling and simulation represents a cost-effective, dependable, and convenient strategy for acquiring a deeper understanding and knowledge of various processes. In the case of biomass boilers, numerous modelling techniques exist, encompassing 0-D, 1-D, 2-D, and 3-D approaches [8]. The choice of modelling technique is contingent upon the desired level of complexity and accuracy for effectively representing the boilers.

These modelling techniques have enabled the examination of plant behaviour and the derivation of conclusions that possess practical implications for real-world systems. The accurate modelling of heat transfer processes taking place within boiler furnaces holds significant importance, as it facilitates the optimisation of combustion, the improvement of thermal efficiency, and the mitigation of emissions. For example, Tzolakis et al. [9] successfully formulated a 1-D process model for a power plant, with the primary objective of maximising the overall efficiency of the facility. The model incorporated the superheater and reheaters, while considering the radiation effects originating from the furnace. To validate the model, it was compared against plant data, and the relative error for all components in terms of energy inlet and outlet remained below 4.39%. This indicates good agreement between the model predictions and the actual performance of the plant.

By applying optimisation techniques on the model, they achieved an increase of 1.42% in the overall efficiency of the power plant. Consequently, this improvement resulted in reduced fuel

consumption and subsequent decrease in flue gas emissions. It is worth noting that even a marginal enhancement in aspects such as efficiency, operating costs, or performance can significantly alleviate the strain on energy resources [7]. This study is just one example among many heat transfer analysis studies that highlight the benefits of using modelling and simulation techniques.

The boiler model encompasses multiple interconnected systems, rendering it a complex phenomenon. Three modes of heat transfer can be observed within the boiler: (i) radiation occurring between solid particles, tubes, and refractory material, as well as nonluminous gas radiation resulting from combustion byproducts; (ii) convection from gases to the furnace walls; and (iii) conduction through ash deposits on the tubes [5]. These principal heat transfer mechanisms occur simultaneously in a boiler.

The calculation of radiation introduces significant complexity. Therefore, the development of an accurate yet efficient model necessitates a delicate balance between complexity and simplicity. As a result, semi-empirical approaches have been devised to streamline this calculation process. The semi-empirical methods discussed herein employ a 0-D representation of the furnace to calculate the heat transfer due to radiation. Although semi-empirical, these approaches incorporate engineering models grounded in fundamental principles [5].

2.2 Zero-Dimensional Furnace Models

The furnace assumes a central role within the boiler system, by facilitating both the combustion process and the transfer of heat to the water [10]. The 0-D modelling technique simplifies the complexity of the furnace by assuming a single gas volume with uniform temperature distribution and heat transfer characteristics throughout its volume, together with a single surrounding surface exposed to radiation heat transfer that represents the water walls and furnace exit plane [8, 11]. It allows the calculation of the radiative heat flux to the water walls as well as the direct radiation through the furnace exit plane. This simplification significantly streamlines the modelling process, making it more manageable and computationally efficient. Consequently, researchers involved in the analysis and evaluation of boilers have widely adopted the 0-D furnace modelling approach.

Two prominent semi-empirical approaches, namely the direct method (also known as the Hottel method) [5-7] and the projected method (also known as the Gurvich/Blokh method) [7, 8], have gained widespread acceptance in 0-D modelling for solid fuel boilers. These methods offer simplified depictions of the intricate processes inherent in such boilers, drawing on the theoretical foundations of the Stefan-Boltzmann law. The direct and projected methods strive to obtain a favourable balance between accuracy and computational complexity, making them extensively employed in

scholarly papers and engineering studies. Moreover, 0-D models are extensively integrated into 1-D boiler models, alongside other components and phenomena, to enhance the representation of the complete boiler system. This integration highlights the considerable adoption and practical application of these models.

There is a wide range of literature available that discusses the implementation of 0-D models. These sources differ in the level of detail provided in their studies and the specific implementation approaches adopted. In the study by Hajebzadeh et al. [12], they developed an integrated steady-state mathematical model for a 320MW tangentially fired boiler. The main objective of their research was to evaluate the effects of various parameters on equipment operation and aging. They utilised the direct method to determine the radiation to the waterwall and superheaters. Empirically formulated view factors, which consider the dimensions of the heat exchangers, were employed to calculate the amount of radiant heat transfer to each superheater. No radiation was considered for the reheaters. The FEGT was determined using both the projected and direct methods, with a maximum difference of 2.02%. The direct method provided better insights into the energy distribution within the furnace.

Rousseau et al. [11] conducted a comprehensive analysis of various modelling approaches used in the study of boilers. They further demonstrated these approaches by applying them to two case study boilers with distinct geometries and firing systems, one fuelled by biomass and the other by coal. The furnace radiation was calculated using both the direct method and the projected method and compared to plant measurements. The comparison of results was done at 100% maximum continuous rating (MCR) for both case study boilers. In the case of the coal-fired boiler at 100% MCR, the projected method yielded a 3.5% overestimation of the evaporator heat load, whereas the direct method overestimated it by 7.6%. For the biomass case at the 100% operating condition, the projected method slightly overestimated the heat uptake of the waterwalls and evaporator bank by 1.7%, while the direct method underestimated it by 3%. Overall, the projected method provided better results compared to the direct method.

Trojan [13] developed a mathematical model specifically for a subcritical boiler, using the projected method to calculate the heat absorbed by the furnace surroundings. The assumption of uniform temperature in the combustion chamber led to the implication that the furnace exit temperature equalled the flame temperature. A comparison between the measured flue gas temperature at the outlet of the combustion chamber (1177.1 °C) and the calculated temperature (1176.0 °C) showed good agreement.

Laubscher and De Villiers [14] conducted a study on a 105 t/h biomass fired industrial water-tube boiler system. They utilised a 0-D furnace model based on the projected method to calculate the heat transfer to the waterwalls and the radiation escaping through the furnace exit. They

determined an area-weighted furnace efficiency factor, which depended on the geometry of the system and fouling level. The heat transfer that escaped the exit plane was computed by considering the furnace exit area, reradiation from downstream external surfaces, and a factor accounting for non-uniformity at the height of the exit plane. During the 100 t/h load case, the model-predicted flue gas temperature at the evaporator outlet was 705.9 K. When compared against the measured temperature of 712.2 K, this resulted in a relative error of 0.68%. Therefore, the applied 0-D model showed good accuracy in predicting furnace heat transfer.

Starkloff et al. [15] conducted a study on the dynamic simulation of large power plants. They used the direct method to determine the heat transfer within the furnace, which considers a radiation heat transfer coefficient accounting for emission and view factors. However, the authors did not explain in detail how this coefficient was derived. To evaluate their simulation model, they performed different steady-state simulations and compared the results with the design data. The maximum differences observed between the model predictions and the design data were 0.54% for enthalpy and 0.17% for pressure. These small deviations suggest that the simulation approach used by Starkloff et al. provides reasonably accurate results in simulating the behaviour of the power plant system.

Chantasiriwan [10] developed models for a conventional utility-scale boiler and its flue gas system, with a specific focus on optimising the placement of an air heater. Their model assumed that all radiation passing through the exit plane reached the superheaters and reheaters. The radiation heat transfer to the heat exchangers was calculated using the direct method, taking into account the radiative heat exchange area between the furnace and the heat exchanger. They also assumed a heat loss in the furnace equivalent to 4% of the fuel heating value. However, the model was not validated against plant data, which means that its accuracy and reliability were not tested through comparison with actual operational results.

Zima et al. [16] developed a computational model to calculate the thermal performance of a natural circulation boiler across a wide range of operating loads. In their model, the thermal load of the furnace chamber waterwalls was assumed to be distributed evenly along the height of the walls. To determine the heat flux absorbed by the furnace waterwalls, they used the projected method. The furnace wall efficiency was calculated by considering the radiation that bypasses the waterwall and the fouling caused by ash deposits, which hinder heat transfer. Additionally, they calculated a combined heat transfer coefficient to consider the radiation effects on the superheater and the first reheater. To verify the accuracy of their 0-D model, Zima et al. conducted CFD simulations. They compared the results of their model with those obtained from the CFD model, focusing specifically on the flue gas temperatures. The comparison showed that their model exhibited good agreement

with the CFD model, indicating that their approach accurately predicted the behaviour of the system, particularly in terms of flue gas temperatures.

2.3 Gas and Particle Radiation Properties

The intricate exchange of radiation within a furnace occurs through complex interactions involving emission, absorption, reflection, and scattering processes between the flue gas and the water walls [5, 6]. The primary constituents responsible for radiation in the flue gas are triatomic gases and suspended particles [7, 8]. Carbon dioxide and water vapor are the predominant triatomic gases that contribute to the radiation in the flue gas [6, 8]. These gases have distinct radiative properties and contribute significantly to the overall heat transfer within the furnace.

In addition to triatomic gases, the combustion process often involves the presence of particulate matter entrained within the combustion gases. These particles, commonly referred to as 'fly ash' or 'soot', have a substantial impact on radiation heat transfer due to their ability to interact with radiation [5-7]. The entrained particles can absorb, emit, and scatter radiation, altering the path and intensity of radiative heat transfer within the furnace. Their composition, size distribution, and concentration significantly influence the overall radiative behaviour of the flue gas. The concentration of dispersed particles in the flue gas, known as the load, determines the extent to which these particles affect the overall transfer of heat through radiation [7]. Higher particle concentrations result in increased scattering effects within the flue gas, which, in turn, directly impacts the rate of radiation heat transfer. The redistribution of heat flux due to scattering alters the spatial distribution of radiative energy within the furnace and affects the overall heat transfer efficiency [5, 6].

In the literature, various calculation procedures have been proposed to account for the influence of particle concentration on radiative heat transfer. Three distinct flue gas and particulate emissivity models, catering to different applications, are available for determining the emissivity of the particle load [6, 11]. These models include the standard model, the low ash model, and the high ash model. The standard model focuses on calculating the emissivity of the flue gas and particle suspension, without considering absorptivity [6, 11]. On the other hand, the low ash model provides a simple calculation of the effective emissivity and effective absorptivity of the flue gas and particle suspension, specifically suitable for fly ash densities less than 0.005 kg/m^3 of the flue gas volume [6, 11]. The high ash model follows a similar procedure to the low ash model but also considers the scattering effects.

The determination of radiative energy emitted by gaseous mixtures using these models relies on factors such as gas temperature, partial pressures of the constituents, and the gas radiation thickness, which is influenced by the shape and dimensions of the gas volume [5, 6]. A combined coefficient of radiant absorption is calculated, considering both the radiation absorbed by triatomic gases and ash particles [7].

Researchers have employed variations of these models in their studies. For example, Zima et al. [16] employed the standard model in their investigation of the natural circulation power boiler. They calculated radiation heat transfer by considering the emissivity of the flue gas but not its absorptivity. The temperature difference in the measured and calculated values of the flue gas was found to be less than 15K, with the highest difference observed at the 60% load case.

Trojan [13] also applied the standard model in their analysis of radiation heat transfer in a steam boiler, following a similar implementation as Zima et al. [16]. The calculated flue gas temperatures exhibited good agreement with the measured values, confirming the appropriate use of the model.

Similarly, other researchers have employed the high ash model and achieved positive results. Laubscher and De Villiers [14] employed the high ash model, despite the particle loading for the model being 0.0045 kg/m^3, a value lower than the threshold of 0.005 kg/m^3 at which thermal radiation exhibits significant scattering. To determine the emissivity of the tri-atomic gas, they employed the weighted sum of the grey gas model, which incorporates empirical coefficients. The effective emissivity of the gas-particulate dispersion in the furnace was calculated by considering the optical thickness of the gas-particulate mixture. Additionally, the scattering effects were considered by accounting for both particulate scattering and absorption through a scattering factor. The gas absorption coefficient was calculated based on the gas emissivity and the mean beam length in the furnace. The implementation closely resembles the approach presented by Kind et al. [6] in the VDI Heat Atlas textbook.

In the mathematical model of a 320MW tangentially fired boiler by Hajebzadeh et al. [12], absorption coefficients for the superheater, waterwall, and gas emissivity were determined based on Hottel's diagrams, considering the partial pressure of H_2O and CO_2. Chantasiriwan [10] used a weighted sum of grey gas model to calculate the emissivity and absorptivity of the flue gas. The model considered factors such as the partial pressure of H_2O and CO_2, mean beam length, and correlation constants referenced to [17].

In a notable study conducted by Rousseau et al. [11], the role of the flue gas and particulate emissivity model was examined. The standard model and the high ash model were compared in a process model analysis. The high ash model exhibited a 3.5% overprediction of furnace heat transfer rate, while the standard model overpredicted by 13.5%. Overall, the high ash model demonstrated

better performance compared to the standard model. These findings highlight the superiority of the high ash model, even in situations with low ash content, aligning with the recommendation proposed in the VDI Heat Atlas textbook [6] to utilise the high ash model regardless of the ash concentration.

2.4 One-Dimensional Boiler Models

1-D models that integrate a 0-D furnace model have been widely employed to investigate various phenomena. In literature, the prevalent practice is to integrate methods obtained from various textbooks [5-8, 18-20] when developing models for boiler systems. The 1-D model itself is based on the fundamental principles of mass, energy, and momentum conservation. By incorporating a 0-D furnace model, these models also calculate the radiative heat transfer that occurs within the furnace.

The predominant focus of research in the field of 1-D models integrated with 0-D furnace models revolves around predicting the temperature distribution and heat transfer within boilers. By accurately predicting the performance of the boiler, researchers can examine different hypothetical scenarios and assess their potential impact. This approach allows for a comprehensive analysis of the behaviour of the boiler under various conditions.

In the study conducted by Rousseau et al. [11], they simultaneously solved the mass, energy, and momentum balance equations for three networks: the flue gas, steam, and air networks. The furnace was considered as a component that transfers thermal radiation from the flue gas suspension to the surrounding water walls and through the furnace exit plane. To simplify the analysis, the water walls and steam drum were combined into a single evaporator component. The researchers developed a generic convective-radiative heat exchanger model that could be applied to various components such as superheaters, reheaters, economisers, and air heaters. This model considered the geometry of the heat exchangers. The effectiveness-NTU method was used to calculate the heat transfer in the heat exchangers, considering the radiation exchange between the heat exchanger and the flue gas through an overall heat transfer coefficient. The developed model was validated using plant data. They also demonstrated the applicability of the model under part-load conditions using the high ash model. The comparison between the model and the plant data showed good agreement, with a maximum relative error of 24% and a minimum relative error of 1%. These results indicate that the model provides reliable predictions of boiler performance.

The study conducted by Hajebzadeh et al. [12] focused on heat transfer surfaces in the boiler, including the superheater, reheater, economiser, gas recirculation in the furnace, and rotary

generative air heaters. The dimensions of these heat exchange surfaces were specified, and the model input data was obtained directly from the actual plant. The amount of heat transfer to the superheaters and reheaters was estimated using the Log Mean Temperature Difference (LMTD) method. The boiler model consisted of several sub-models, and the modified Newton-Raphson method was employed to numerically solve the equations of each sub-model. The temperatures obtained from the model were validated against corresponding measured temperatures from the power plant, with a maximum relative error of 8.72% and an average relative error of 1.29%.

Trojan [13] developed distributed parameter mathematical models for individual stages of the steam superheater, air heater, and economiser, taking into account the complex flow arrangement of all heat exchangers. The effectiveness-NTU method was used to calculate the flue gas and air temperatures in the air heater stages. Iterative calculations were performed for steam, flue gas, and air systems. The boiler operations were analysed for both clean and slagging-affected conditions. The calculated steam and flue gas temperatures after the various heat exchangers showed good agreement with the measured temperatures.

In their study, Laubscher and De Villiers [14] developed a model that captures the interaction among the air, flue gas, and steam networks. The model integrates the 0-D furnace model within the furnace control volume, where heat is transferred from the flue gas circuit, subsequently providing heat transfer to the water circuit. The water and gas cycles are treated as a coupled system, meaning that the heat transfer rates in one network directly affect the other, necessitating a simultaneous solution approach. To solve the convective heat transfer in the heat exchangers, the model utilises the LMTD method. The performance of the model was evaluated by comparing the average relative temperature prediction errors of the water cycle with plant data for different load cases: 100 t/h, 65 t/h, and 35 t/h. The relative temperature prediction errors for the water cycle were found to be 1.48%, 0.84%, and 5.31% for the respective load cases. Similarly, for the flue gas, the relative errors were 1.47%, 0.58%, and 4.84% for the corresponding load cases. These results highlight the capability of the model to predict heat transfer with reasonable accuracy, even at lower load conditions.

In an ideal scenario, a boiler functions optimally when operating at a consistent design load. However, it is also necessary for the boiler to accommodate off-design load conditions. These conditions arise due to changes in supply and demand, as well as the growing utilisation of renewable energy sources [21]. To meet the need for dynamic operation in power plants, researchers have conducted studies to comprehend the dynamic behaviour of boilers. Numerous investigations have concentrated on developing detailed boiler models, primarily validated under steady-state conditions.

For example, Castilla et al. [22] developed a dynamic model for a fluidised bed boiler using semi-empirical correlations derived from previous studies to describe fluid dynamics, fuel conversion, and heat transfer to furnace walls. The furnace heat transfer was modelled using the direct method, assuming a constant waterwall temperature equal to the waterside temperature. The model was validated against steady-state operational data and then calibrated for transient validation. It exhibited satisfactory agreement with measured data within an absolute error of less than 10% for operational loads ranging from 50% to 100%.

In their study, Zima et al. [16] developed a model that analysed heat transfer in a boiler by dividing it into main surfaces and additional surfaces. The main surfaces, including the superheater, reheater, and economiser, were modelled using the methodology proposed by Orlowski [23]. The additional surfaces encompassed other heat transfer surfaces present in the boiler. Heat flux distributions for these surfaces were calculated based on their respective surface areas. The calculations were performed iteratively for subsequent heated surfaces along the path of the combustion gas flow. The researchers varied the loads from 40% to 100% under steady-state conditions. To evaluate the accuracy of the model, the calculation results were compared with boiler process data, although specific details were not disclosed. The model demonstrated good performance, with temperature differences remaining within a few Kelvins.

Taler et al. [24] developed a mathematical model for a steam boiler evaporator to propose a quick start-up procedure from a cold state. They used a 0-D approach based on the projected method to model heat transfer from the flue gas to the boiler evaporator. In this method, the calculated radiation heat transfer is considered as the heat supplied to the evaporator. Furthermore, the projected method was employed to determine the flame temperature. While the authors did not elaborate on the specific modelling techniques used for the other components, they conducted validation experiments, which showed satisfactory agreement between the model predictions and the experimental results.

In their study, Starkloff et al. [15] utilised a 1-D modelling approach to analyse the interactions between water and flue gas in a power plant. The model encompassed the air, flue gas, and water cycles. Convective heat transfer in the boiler was calculated by incorporating an empirical convective heat transfer coefficient that considered plant-specific geometries and the gas mass flow rate. The state properties were determined as the average between the inlet and outlet, while flow-related variables were computed at the boundary between two connecting control volumes. The 1-D partial differential equations were solved using the finite volume solution method implemented in Advanced Process Simulation (APROS). Prior to conducting dynamic simulations, various steady-state simulations were performed. The comparison between the model and the design data revealed a maximum relative deviation of 0.53% for enthalpy and 0.17% for pressure.

Oko and Wang [25] developed a dynamic model for a 500 MWe sub-critical boiler. They employed a simplified 0-D furnace model based on the projected method. The effective gas temperature was determined by taking a weighted average of the adiabatic flame temperature and the temperature of the gases leaving the furnace. A notable aspect of their approach was the incorporation of an attenuation coefficient, which differed from the conventional method. In the conventional approach, factors like furnace emissivity and efficiency are considered to account for fouling and angular effects. However, in their model, an attenuation coefficient was used instead. It is important to note that their model did not include the consideration of energy losses in the overall energy balance. Validation of the model was conducted for loads ranging from 70% to 100%, and it reasonably predicted plant performance with a relative error of less than 5%.

Chandrasekharan [26] developed a mathematical model using MATLAB to represent the economiser unit, drum unit, and superheater unit of a boiler. The model considers the feed water flow rate and heat flow rate from the furnace as inputs. To simplify the model, certain assumptions were made, such as treating parallel water tubes in the economiser and superheater as a single tube and considering the three stages of superheating as a single unit. The accuracy of the model was validated by comparing it against plant data, with the mean square error method used to analyse the error. The findings demonstrated good agreement between the model and plant data, indicating the reliability of the model.

1-D models have also been developed to explore various operational scenarios in power plants, including flue gas recirculation and post-combustion processing. Lawal et al. [18] created a 1-D model using the General Process Modelling System (gPROMS) software to study the design and operation of full-scale post-combustion CO_2 capture in a 500MWe sub-critical power plant. The authors employed the projected method to model radiation heat transfer, although they did not provide detailed information on the evaluation of certain variables in this method. The effective gas temperature was calculated as a weighted average of the adiabatic flame temperature and the furnace exit gas temperature. The steady-state model was compared with measured data, demonstrating satisfactory agreement. After validating the power plant model, it was coupled with the CO_2 capture model.

Marx-Schubach and Schmitz [27] developed a detailed model of a post-combustion CO_2 plant using the Modelica language. This model was coupled with a power plant model to investigate the integrated process. To determine heat transfer to the waterwall, the direct method was employed, specifically based on the methodology outlined in the VDI Heat Atlas [19], which incorporates the Hottel method for analysis. The emissivity of the suspension and the weight factors of the weighted sum of the grey gas model were also computed in accordance with the procedures described in [19]. Heat transfer from the flue gas to the tube bundles in the superheater, reheater, and economiser

was characterised by a combined convection and radiation approach. The contribution of radiation heat exchange in the heat exchangers was calculated by considering factors such as tube fouling, surface area, suspension absorbance, and the emissivity of the heat exchanger. The model is capable of simulating start-up, shutdown, and regular operation processes.

In the study by Chantasiriwan [12], a counterflow heat exchanger model was employed to simulate the behaviour of the superheater and reheater in a boiler. The model utilised overall heat transfer calculations based on the work of Kakaç [17]. Negligible conduction resistance was assumed for the tube walls of the superheater and reheater. By establishing equations that describe the interactions among different boiler components, an iterative solution approach was employed. The study revealed that placing a flue gas dryer after an additional air heater resulted in lower total installation costs compared to placing it before. Furthermore, the installation of an appropriately sized air heater was found to increase boiler efficiency from 84.2% to 85.7%.

Zhang et al. [28] investigated the influence of flue gas recirculation on reheat steam temperature, boiler efficiency, and thermal efficiency. They employed the Gurvich (projected) method to calculate furnace heat transfer, considering the effects of flue gas recirculation. In their calculations, they employed the standard model, which disregards absorption effects within the furnace. Furthermore, they took into consideration the radiant effects on the superheaters by assessing both the bypass radiation from the preceding superheater and the direct radiation incident on the specific superheater of interest. The calculated results of the model without flue gas recirculation closely matched the measured data under different load conditions, indicating the reliability of the proposed model.

Previous studies described in the literature have provided evidence that the use of 1-D models has been highly influential in advancing research on boilers. The models developed in these studies integrated a 0-D furnace model to develop comprehensive boiler models for their research purposes. This highlights the widespread use of 0-D furnace models in various applications documented in the literature.

2.5 CFD Combined with One-Dimensional Modelling

The combination of CFD and 1-D modelling has been utilised in diverse ways. CFD has been particularly useful in predicting temperatures for boiler models, where on-site measurements are challenging. Additionally, researchers have conducted studies that integrate CFD models with 1-D models to enhance the accuracy of the latter. Laubscher and De Villiers [14] validated their model further in their study of the 105t/h bagasse fired boiler system by comparing it to results obtained from a validated CFD model of the bagasse boiler. The comparison revealed that the model results were in good agreement with those from the CFD model.

Díez et al. [3] developed a model for monitoring and simulating large utility boilers. The aim was to enhance performance by integrating off-line CFD predictions. The model considered radiation to the superheaters and employed the direct method to calculate furnace heat transfer. The gas emissivity was determined using the method introduced by Kakaç [18]. CFD was utilised to determine particle flow rates through each zone, improving the online monitoring technique. The model was validated against 60 operating conditions, and the simulation results exhibited excellent agreement with the measured data, with a maximum temperature prediction error of less than 5%.

Zima et al. [16] adopted a process modelling approach to perform thermal calculations on a natural circulation power boiler. The furnace calculations were conducted using the direct method. The predicted heat fluxes and exit flue gas temperatures were verified using a CFD model under steady-state conditions spanning load ranges from 40% to 100%. The highest temperature difference observed during the analysis of operating loads was 15K.

Rousseau and Laubscher [29] developed a novel 1-D thermofluid model for the membrane walls of a pulverised boiler to determine unknown temperatures across the membrane wall. Detailed CFD results were employed to validate the model. The overall heat transfer coefficient of the model was found to be within 1% of the CFD results.

Madejski et al. [30] developed a mathematical model to simulate the thermal and flow processes in a steam superheater operating within a large-scale coal-fired boiler under both steady-state and transient conditions. The model integrated a 0-D model of the circulating fluidised bed, a 1-D model of steam flow, and a 2-D model of the superheater tube wall. Radiative heat from the furnace was accounted for using a 0-D modelling approach, and the radiative heat transfer coefficient of the flue gas was determined through the direct method. CFD was employed to calculate the convective heat transfer coefficient. The developed model exhibited high accuracy while maintaining a reasonable computational time.

2.6 Summary

1-D modelling that integrates 0-D furnace models offer a promising approach for simulating the behaviour of solid fuel boilers. The literature review showed that 1-D modelling coupled with a 0-D furnace model has emerged as a valuable tool for studying and optimising the combustion processes in biomass boilers. Researchers from diverse fields have dedicated their efforts to developing and refining these models, ultimately contributing to a deeper understanding of the intricate mechanisms involved in solid fuel combustion. Furthermore, the reviewed literature highlighted the successful application of these models in optimising solid fuel boiler designs, enhancing thermal efficiency, reducing emissions, and improving operational performance. The insights gained from these studies have provided valuable guidance for engineers and designers in developing more efficient and sustainable biomass boiler systems.

It is worth noting that despite the advancements made in 1-D modelling of biomass boilers, there are still some challenges that need to be addressed. Most of the models are applied without a systematic evaluation of the underlying principles of the 0-D approach and their suitability for integration. Most of the integrated 0-D models are sourced from textbooks and incorporated into the 1-D models without assessing the uncertainty associated with them. Further research is still needed to refine the models, integrate more detailed sub-models, and validate them with a wide range of solid fuel boilers under different operating conditions. With further research and development, these models hold immense potential for advancing sustainable energy generation through solid fuel combustion.

The following section will outline the modelling methodology for the 0-D furnace models.

3. Methodology

The primary focus of this study is to analyse the performance of the furnace, with a particular emphasis on the specific 0-D furnace models used in the investigation, rather than the comprehensive 1-D boiler process model. Rousseau et al. [11] present the comprehensive 1-D boiler process model, which integrates the 0-D furnace model explored in this research.

Evaluating the performance of the furnace involves conducting essential calculations to understand various operational aspects. Key calculations include determining the steam mass and energy balance, combustion species mass balance, boiler mass and energy balance, adiabatic flame temperature, as well as gas and particle emissivity and absorptivity. The emissivity and absorptivity of gases and particles can be determined using either the standard method [8] or the high ash method [31]. The low ash method has been excluded due to the demonstrated superiority of the high ash method [6], even in conditions where ash content is low. These calculations will enable an evaluation of furnace performance using either the direct method or the projected method.

To ensure accurate prediction of system performance, it is essential to consider various inlet and outlet conditions. The process flow diagram, depicted in Figure 3.1, outlines the sub-models integral to both the projected and direct method for determining furnace performance. Detailed discussions on these sub-models will be presented in Sections 3.1 through to 3.6.

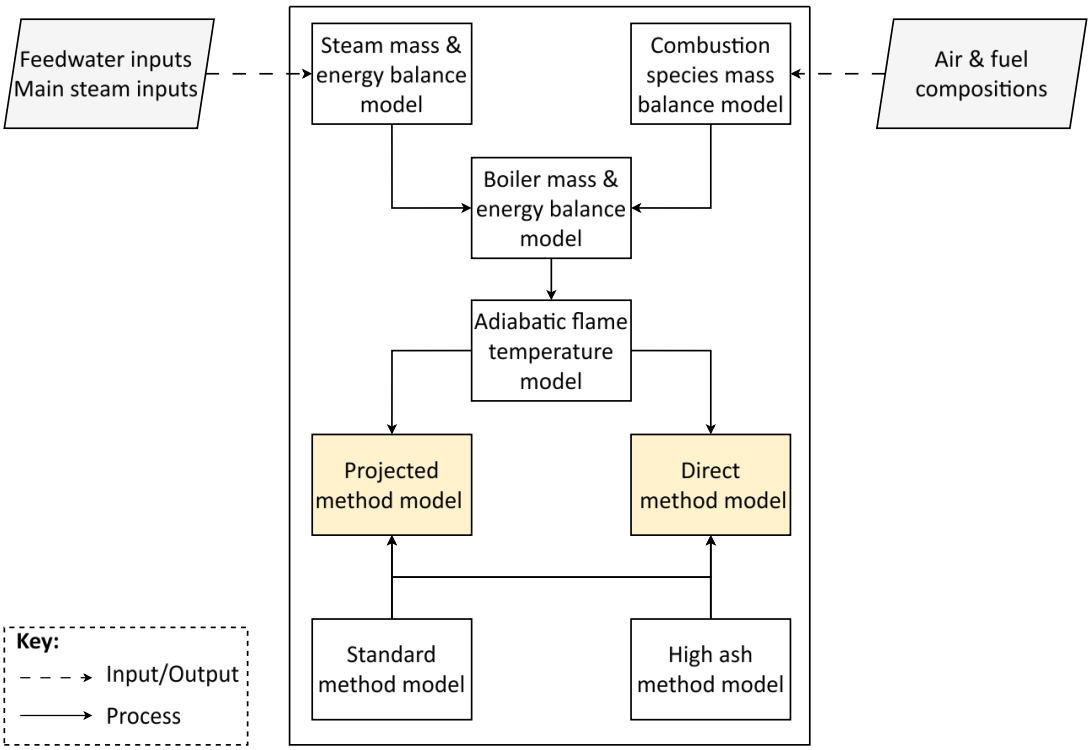

***Figure 3.1**: Process flow diagram – 0-D furnace model.*

3.1 Combustion Species Mass Balance

The combustion of fuel in a boiler furnace releases a large amount of energy, which heats up the products of combustion (flue gas) to high temperatures. A species mass balance is then performed to determine the composition of the flue gas. The species mass balance necessitates prior knowledge of the fuel composition, air composition, and the quantity of air used during combustion.

The methodology for performing the combustion species mass balance is based on the approach presented by Rousseau et al. [11] and further detailed in the University of Cape Town course notes on Power Plant Boilers [32].

Biomass consists of varying proportions of carbon (C), hydrogen (H), oxygen (O), nitrogen (N), sulphur (S), moisture (M) and ash. Each fuel type has a unique combination of these elements and compounds. The mass fraction composition of a solid fuel is typically represented in an as-received analysis, expressed in kilograms per kilogram of fuel. It is important to note that the summation of all mass fractions should equate to one, representing the entirety of the fuel composition, as shown in Equation 3.1. Here, $Y_{i_{AR}}$ denotes the as-received (AR) mass fraction of element (i) in the fuel, including moisture $(Y_{M_{AR}})$ and ash $(Y_{ash_{AR}})$.

$$Y_{AR} = Y_{C,UC_{AR}} + Y_{H_{AR}} + Y_{O_{AR}} + Y_{N_{AR}} + Y_{S_{AR}} + Y_{M_{AR}} + Y_{ash_{AR}} = 1.000 \quad 3.1$$

In the fuel mass fractions in Equation 3.1, $Y_{C,UC_{AR}}$ includes the unburnt carbon. Therefore, it is convenient to represent only the fraction of carbon actively involved in combustion, which then excludes unburnt carbon $(Y_{UC_{AR}})$ present in the as-received values, as shown in Equation 3.2.

$$Y_{C_{AR}} = Y_{C,UC_{AR}} - Y_{UC_{AR}} \quad 3.2$$

Since ash consists of non-combustible materials, it passes through the process without participating in combustion, making it convenient to perform the species mass balance on an ash-free (AF) basis. The ash-free fuel composition $(Y_{i_{AF}})$ and its mass flow rate $(\dot{m}_{f_{AF}})$ are derived from the as-received values as in Equations 3.3 and 3.4, respectively, where $\dot{m}_{f_{AR}}$ represents the as-received mass flow rate of the fuel.

$$Y_{i_{AF}} = \frac{Y_{i_{AR}}}{1 - Y_{ash}} \quad 3.3$$

$$\dot{m}_{f_{AF}} = (1 - Y_{ash}) \cdot \dot{m}_{f_{AR}} \quad 3.4$$

The normalised ash free fuel mass fractions $(Y_{i_{AF}})$ in Equation 3.3 encompass all constituents including the unburnt carbon, but exclude the ash, as shown in Equation 3.5.

$$Y_{AF} = Y_{C_{AF}} + Y_{H_{AF}} + Y_{O_{AF}} + Y_{N_{AF}} + Y_{S_{AF}} + Y_{M_{AF}} + Y_{UC_{AF}} = 1.000 \quad 3.5$$

The chemical formula of the fuel is generally expressed as $C_{n_{fC}}H_{n_{fH}}O_{n_{fO}}N_{n_{fN}}S_{n_{fS}}M_{n_{fM}}$, which serves as a general representation for the composition of any fuel. Here, n_{f_i} denotes the moles of the fuel constituents (C, H, O, N, S, M) in one kilomole of fuel, determined using Equation 3.6. The molecular mass of each constituent is denoted by M_i, and the mean molecular mass of the ash-free fuel mixture $M_{f_{AF}}$ is determined using Equation 3.7.

$$n_{f_i} = \frac{Y_{i_{AF}}}{M_i} \cdot M_{f_{AF}} \quad 3.6$$

$$M_{f_{AF}} = \left(\sum_i \frac{Y_{i_{AF}}}{M_i} \right)^{-1} \quad 3.7$$

The principle of mass balance requires the conservation of total mass for each element throughout a chemical reaction, while molar balance ensures the conservation of total moles of each element during the reaction. Therefore, a generic chemical equation can be formulated to represent the combustion of fuel with air, denoted by Equation 3.8. This equation assumes instantaneous and complete combustion. A detailed derivation of Equation 3.8 is presented in Appendix A.

$$\begin{aligned} &C_{n_{fC}}H_{n_{fH}}O_{n_{fO}}N_{n_{fN}}S_{n_{fS}}M_{n_{fM}} + n_{r_{O_2}} \cdot O_2 + n_{r_{N_2}} \cdot N_2 + n_{r_{H_2O}} \cdot H_2O \\ &\rightarrow n_{p_{CO_2}} \cdot CO_2 + n_{p_{N_2}} \cdot N_2 + n_{p_{SO_2}} \cdot SO_2 + n_{p_{H_2O}} \cdot H_2O + n_{p_{O_2}} \cdot O_2 \end{aligned} \quad 3.8$$

In this equation, n_{r_i} and n_{p_i} represent the moles of the reactants and products in one kilomole of fuel, respectively. The detailed calculations for the moles of the reactants are outlined in Equations 3.9, 3.11 and 3.12.

To begin with, Equation 3.9 calculates the moles of oxygen in the supplied air.

$$n_{r_{O_2}} = \alpha \cdot n_{st_{O_2}} \quad 3.9$$

Here, $n_{st_{O_2}}$ represents the stoichiometric oxygen, which is the minimum amount of oxygen required for complete combustion. The calculation of stoichiometric oxygen is shown in Equation 3.10 and its derivation is provided in Appendix A.

$$n_{st_{O_2}} = n_{fC} + \frac{1}{4}n_{fH} - \frac{1}{2}n_{fO} + n_{fS} \quad 3.10$$

In practical combustion scenarios, more than the theoretical amount of air is typically required to achieve complete combustion. Consequently, excess air is supplied, which is quantified by the excess air ratio, α. This ratio indicates the proportion of oxygen in the supplied air relative to the stoichiometric oxygen.

Next, Equation 3.11 calculates the moles of nitrogen in the supplied air, based on the stoichiometric ratio of nitrogen to oxygen in air. The factor 3.7619 reflects this ratio.

$$n_{r_{N_2}} = 3.7619 \cdot \alpha \cdot n_{st_{O_2}} \tag{3.11}$$

Finally, Equation 3.12 determines the moles of water vapor present in the humid air used for combustion. The factor 4.7619 is derived from the stoichiometric ratio of nitrogen to oxygen in air. The molecular masses of air (M_{air}) and water (M_{H_2O}) are utilised to convert the specific humidity (w), defined as the mass of moisture per kilogram of dry air, into molar terms.

$$n_{r_{H_2O}} = 4.7619 \cdot \alpha \cdot w \cdot \frac{M_{air}}{M_{H_2O}} \cdot n_{st_{O_2}} \tag{3.12}$$

The moles of the products are given by Equations 3.13 to 3.17. First, Equation 3.13 calculates the moles of carbon dioxide produced, which are directly proportional to the carbon content in the fuel.

$$n_{p_{CO_2}} = n_{fC} \tag{3.13}$$

Next, Equation 3.14 calculates the moles of nitrogen in the flue gas, including nitrogen from both the fuel and the air.

$$n_{p_{N_2}} = \frac{1}{2} \cdot n_{fN} + 3.7619 \cdot \alpha \cdot n_{st_{O_2}} = \frac{1}{2} \cdot n_{fN} + n_{r_{N_2}} \tag{3.14}$$

Following this, Equation 3.15 calculates the moles of sulphur dioxide produced, which are directly proportional to the sulphur content in the fuel.

$$n_{p_{SO_2}} = n_{fS} \tag{3.15}$$

Subsequently, Equation 3.16 calculates the moles of water vapor in the flue gas, including moisture from both the fuel and the humid air.

$$n_{p_{H_2O}} = n_{f_M} + \frac{1}{2} \cdot n_{fH} + 4.7619 \cdot \alpha \cdot w \cdot \frac{M_{air}}{M_{H_2O}} \cdot n_{st_{O_2}} = n_{f_M} + \frac{1}{2} \cdot n_{fH} + n_{r_{H_2O}} \tag{3.16}$$

Lastly, Equation 3.17 calculates the moles of excess oxygen remaining in the flue gas after combustion.

$$n_{p_{O_2}} = (\alpha - 1) \cdot n_{st_{O_2}} \quad 3.17$$

Once the combustion species mass balance is complete, the air-fuel ratio (AFR) can be calculated. This ratio is essential for determining the required mass flow rate of combustion air, which will be calculated in Section 3.3, after the mass flow rate of fuel has been calculated from the boiler mass and energy balance. The air-fuel ratio is defined as the ratio of the mass of humid air to the as-received mass of fuel, as shown in Equation 3.18. It is important to note that the conventional air-fuel ratio is defined as the ratio of dry combustion air to the as-received fuel flow rate.

$$AFR = \frac{\dot{m}_{ca}}{\dot{m}_{f_{AR}}} \quad 3.18$$

The mass flow rate of humid combustion air ($\dot{m}_{ca}$) is determined by the sum of the mass flow rates of oxygen ($\dot{m}_{r_{O_2}}$), nitrogen ($\dot{m}_{r_{N_2}}$), and water vapor ($\dot{m}_{r_{H_2O}}$), as shown in Equation 3.19.

$$\dot{m}_{ca} = \dot{m}_{r_{O_2}} + \dot{m}_{r_{N_2}} + \dot{m}_{r_{H_2O}} \quad 3.19$$

The mass flow rate of any constituent (i) in the reactants and the products can be calculated using Equation 3.20. This equation determines the mass flow rate of each constituent based on its molar quantity, molecular mass, and the mass flow rate of ash-free fuel.

$$\dot{m}_i = n_i \cdot M_i \cdot \frac{\dot{m}_{f_{AF}}}{M_{f_{AF}}} \quad 3.20$$

Substituting the individual mass flow rates in Equation 3.19 using Equation 3.20, we obtain Equation 3.21.

$$\dot{m}_{ca} = \left(n_{r_{O_2}} M_{O_2} + n_{r_{N_2}} M_{N_2} + n_{r_{H_2O}} M_{H_2O}\right) \frac{\dot{m}_{f_{AF}}}{M_{f_{AF}}} \quad 3.21$$

After substituting Equation 3.4 to express the ash-free fuel flow rate in terms of the as-received flow rate, and manipulating Equation 3.21 to describe the mass flow rate of air relative to the as-received fuel, we deduce Equation 3.22, which defines the AFR.

$$AFR = \left(n_{r_{O_2}} M_{O_2} + n_{r_{N_2}} M_{N_2} + n_{r_{H_2O}} M_{H_2O}\right) \frac{(1 - Y_{ash})}{M_{f_{AF}}} \quad 3.22$$

Similarly, the flue gas ratio (FGR) is defined as the mass flow rate of flue gas $(\dot{m}_{fg})$ to the as-received mass flow rate of the fuel, expressed in Equation 3.23.

$$FGR = \frac{\dot{m}_{fg}}{\dot{m}_{f_{AR}}} \tag{3.23}$$

The mass flow rate of flue gas comprises the sum of the mass flow rates of carbon dioxide ($\dot{m}_{p_{CO_2}}$), nitrogen ($\dot{m}_{p_{N_2}}$), sulphur dioxide ($\dot{m}_{p_{SO_2}}$), water vapor ($\dot{m}_{p_{H_2O}}$), and oxygen ($\dot{m}_{p_{O_2}}$), as detailed in Equation 3.24.

$$\dot{m}_{fg} = \dot{m}_{p_{CO_2}} + \dot{m}_{p_{N_2}} + \dot{m}_{p_{SO_2}} + \dot{m}_{p_{H_2O}} + \dot{m}_{p_{O_2}} \tag{3.24}$$

The equation above utilises the mass flow rates of individual flue gas compounds ($\dot{m}_{p_i}$), obtained through calculations detailed in Equation 3.19. By substituting these values into Equation 3.24, we obtain Equation 3.25.

$$\dot{m}_{fg} = \left(n_{p_{CO_2}} M_{CO_2} + n_{p_{N_2}} M_{N_2} + n_{p_{SO_2}} M_{SO_2} + n_{p_{H_2O}} M_{H_2O} + n_{p_{O_2}} M_{O_2}\right) \frac{\dot{m}_{f_{AF}}}{M_f} \tag{3.25}$$

After substituting Equation 3.4 to express the ash-free fuel flow rate in terms of the as-received flow rate, and manipulating Equation 3.25 to describe the mass flow rate flue gas relative to the as-received fuel, we deduce Equation 3.26, which defines the FGR.

$$FGR = \left(n_{p_{CO_2}} M_{CO_2} + n_{p_{N_2}} M_{N_2} + n_{p_{SO_2}} M_{SO_2} + n_{p_{H_2O}} M_{H_2O} + n_{p_{O_2}} M_{O_2}\right) \frac{(1 - Y_{ash})}{M_f} \tag{3.26}$$

The ash-free mass fractions of the flue gas (Y_{fg_i}) per kilogram of fuel can be expressed using Equation 3.27.

$$Y_{fg_i} = \frac{\dot{m}_{fg_i}}{\dot{m}_{f_{AF}}} = \frac{n_{p_i} M_i}{M_{f_{AF}}} \tag{3.27}$$

Finally, the molar mass of the flue gas (M_{fg}) can then be determined using Equation 3.28.

$$M_{fg} = \left(\sum_i \frac{Y_{fg_i}}{M_i}\right)^{-1} = \frac{\sum_i n_{p_i} \cdot M_i}{\sum_i n_{p_i}} \tag{3.28}$$

These equations collectively provide a comprehensive framework for understanding and calculating crucial parameters that govern combustion and emission characteristics in boiler systems, under the assumption of complete combustion.

3.2 Steam Mass and Energy Balance

The steam mass and energy balance facilitates the calculation of the heat added to the steam, thereby enabling the determination of the required fuel mass flow rate. In a boiler, water is heated through various heat exchangers; some are used for steam generation, while others heat the fluid in a single phase. The cumulative heat transferred to the boiler, referred to as the heat load ($\dot{Q}_{steam}$), represents the heat necessary from the flue gas to produce steam at its final conditions. In scenarios where there are no reheaters and blowdown is absent, the control volume of the steam cycle can be represented as shown in Figure 3.2.

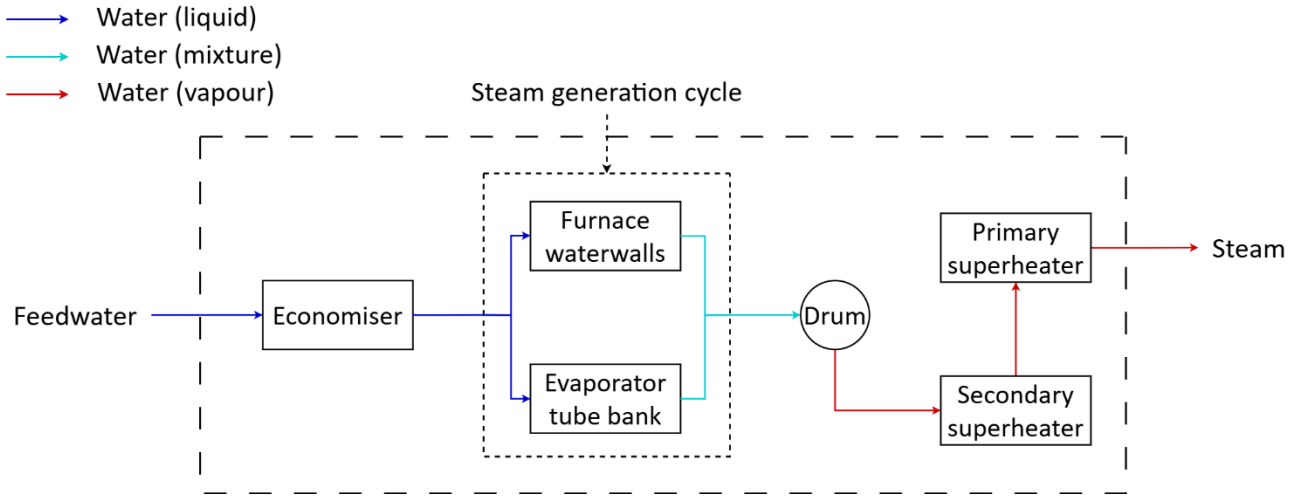

Figure 3.2: *Control volume – Steam mass and energy balance.*

Based on this control volume, the steam load can be calculated using Equation 3.29.

$$\dot{Q}_{steam} = \dot{m}_{ms_e} h_{ms_e} - \dot{m}_{fw_i} h_{fw_i} \tag{3.29}$$

In the equation, $\dot{m}_{ms_e}$ and h_{ms_e} denote the mass flow rate and enthalpy of the main steam at the final superheater stage, respectively. Conversely, $\dot{m}_{fw_i}$ and h_{fw_i} denote the mass flow rate and enthalpy of the feedwater. These parameters are typically known in advance and serve as boundary conditions within the boiler model. The calculated steam heat load is then utilised in the subsequent section of the boiler mass and energy balance to determine the required mass flow rate of fuel.

3.3 Boiler Mass and Energy Balance

Once the required water heat load is calculated and the species mass balance is performed, the fuel and air mass flow rates can be determined by performing a mass and energy balance calculation of the boiler control volume. Figure 3.3 illustrates the specific boundaries and components encompassed within the boiler control volume that are under examination in this analysis.

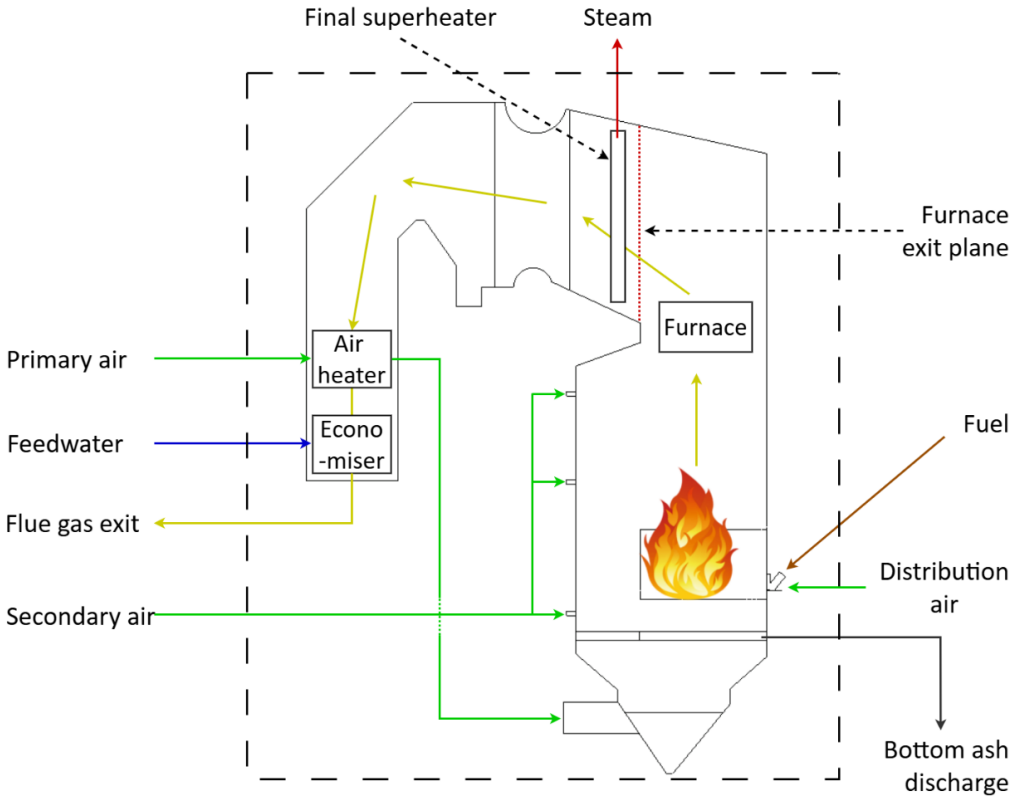

Figure 3.3: *Control volume – Boiler mass and energy balance.*

The energy balance is expressed by Equation 3.30, where the left-hand side represents the energy inputs, and the right-hand side represents the energy outputs. Here, the energy inputs include the sensible energy of the fuel ($\dot{Q}_{fuel_s}$), the heat released due to the combustion of the fuel ($\dot{Q}_{react}$), and the heat of the total supplied combustion air ($\dot{Q}_{ca}$). The energy outputs and losses are represented by $\dot{Q}_{fg_e}$, the heat leaving the boiler through the flue gas at the final heat exchanger, and ($\dot{Q}_{losses}$), the various heat losses that occur in the boiler.

$$\dot{Q}_{fuel_s} + \dot{Q}_{react} + \dot{Q}_{ca} = \dot{Q}_{steam} + \dot{Q}_{losses} + \dot{Q}_{fg_e} \qquad 3.30$$

Post-combustion, the ash in the fuel, along with some unburnt carbon, is extracted from the bottom of the furnace, while another portion is conveyed by the flue gas as fly ash. The mass flow rates of these constituents are described by Equation 3.31. In these equations, $\dot{m}_{UC}, \dot{m}_{ash}, \dot{m}_{fa}, \dot{m}_{ba}$ are the

mass flow rates of unburnt carbon, ash, fly ash, and bottom ash, respectively. The fractions f_{fa} and f_{ba} represent the proportions of fly ash and bottom ash in the unburnt carbon and ash.

$$\begin{aligned} \dot{m}_{UC} &= \dot{m}_{f_{AR}} \cdot Y_{UC_{AR}} \\ \dot{m}_{ash} &= \dot{m}_{f_{AR}} \cdot Y_{ash_{AR}} \\ \dot{m}_{fa} &= f_{fa} \cdot (\dot{m}_{ash} + \dot{m}_{UC}) \\ \dot{m}_{ba} &= f_{ba} \cdot (\dot{m}_{ash} + \dot{m}_{UC}) \end{aligned} \quad 3.31$$

The energy inputs can be expressed as shown in Equation *3.32*, where h_{f_s}, h_{ash} and h_{ca} are the enthalpies of fuel (sensible), ash, and combustion air, respectively. h_{ca} is the enthalpy of combustion air at ambient air temperature before any air is preheated in the air heater. The higher heating values (HHV) of the fuel and carbon are denoted as HHV_f and HHV_C.

$$\begin{aligned} \dot{Q}_{fuel_s} &= \dot{m}_{f_{AR}} \cdot h_{f_s} \\ \dot{Q}_{react} &= \dot{m}_{f_{AR}} \cdot HHV_f - \dot{m}_{UC} \cdot HHV_C \\ \dot{Q}_{ca} &= \dot{m}_{ca} \cdot h_{ca} \end{aligned} \quad 3.32$$

The boiler loses energy through the fly ash $(\dot{Q}_{fa})$ and bottom ash $(\dot{Q}_{ba})$. Additionally, the boiler may lose energy to the surroundings via radiation, convection, or conduction through its casing $(\dot{Q}_{radloss})$. The energy losses and outputs are represented by Equation *3.33*, where $f_{radloss}$ is the fraction of combustion heat lost and h_{fg_e} is the enthalpy of flue gas at the final heat exchanger.

$$\begin{aligned} \dot{Q}_{fa} &= \dot{m}_{fa} \cdot h_{fa} \\ \dot{Q}_{ba} &= \dot{m}_{ba} \cdot h_{ba} \\ \dot{Q}_{radloss} &= f_{radloss} \cdot \dot{Q}_{react} \\ \dot{Q}_{fg_e} &= \dot{m}_{fg} \cdot h_{fg_e} \end{aligned} \quad 3.33$$

By rearranging the equations in 3.32 and 3.33, and using the equations in 3.31 to express them as functions of the as-received mass flow rate of fuel, the mass flow rate is then calculated as shown in Equation 3.34.

$$\dot{m}_{f_{AR}} = \frac{\dot{Q}_{steam}}{\begin{array}{c}\left(h_{f_s} + HHV_f - Y_{UC_{AR}} \cdot HHV_C \cdot + AFR \cdot h_{ca}\right) \\ - \left(f_{fa} \cdot (Y_{ash_{AR}} + Y_{UC_{AR}}) \cdot h_{fa} + f_{ba} \cdot (Y_{ash_{AR}} + Y_{UC_{AR}}) \cdot h_{ba}\right. \\ \left. + f_{radloss} \cdot (HHV_f - Y_{UC_{AR}} \cdot HHV_C) + FGR \cdot h_{fg_e}\right)\end{array}} \quad 3.34$$

In combustion analysis, calculating the enthalpies of combustion products requires a common reference state because fluid compositions change significantly from the beginning to the end of the process. Thermodynamic analysis typically focuses on changes in properties $(\Delta u, \Delta h, \Delta s)$ rather than their absolute values (u, h, s). Standard thermodynamic tables, such as ideal-gas tables, set property values to zero at a chosen reference temperature T_{ref}. Any property values at other states are calculated as differences from this reference state, i.e., $h - h_{ref}$, where $h_{ref} = 0$.

For combustion analysis the chosen common reference state, known as the standard reference state, is set at $T_{ref} = 25°C$ and pressure $p_{ref} = 101.325kPa$ [33]. Existing property tables can be used by subtracting the enthalpy values at this reference state from the values of the current state. Note that the enthalpy at the standard reference state can differ for the different constituents.

The total heat released at the standard reference state is termed the heating value of the fuel, which accounts for the net effect of the enthalpies of formation of all reactants and products. This value is typically expressed per kilogram of fuel, including ash. The heating value varies based on the phase of H_2O in the products: it is the lower heating value (LHV) when H_2O is in vapour form and the higher heating value (HHV) when H_2O is in liquid form. Relevant to combustion analysis, LHV excludes the heat used to vaporise water in the fuel and combustion air, while HHV accounts for the latent heat of vaporisation of water in combustion products. These two values are related by Equation *3.35*.

$$HHV_f = LHV_f + \frac{\dot{m}_{p_{H_2O}}}{\dot{m}_f}\left(h_{fg_{H_2O}}\right)_{25^0C} \quad 3.35$$

Utilising real gas property functions from resources like CoolProp [34] (an open-source fluid properties database), which incorporate latent energy within the vapour phase of water, requires that HHV must be used in combustion energy balance equations.

The enthalpies of the fuel, fly ash and bottom ash at the standard reference state can be calculated using Equations 3.36-3.38 respectively. Here c_{p_f} and $c_{p_{ash}}$ represent the specific heat capacities of fuel and ash, respectively, while T_f, T_{fg} and T_{ba} are the temperatures of the fuel, flue gas and bottom ash, respectively. For simplicity, we assume that the specific heat capacities of both fuel and ash remain constant throughout the boiler.

$$h_{f_s} = c_{p_f}(T_f - T_{ref}) \quad 3.36$$

$$h_{fa} = c_{p_{ash}}(T_{fg} - T_{ref}) \quad 3.37$$

$$h_{ba} = c_{p_{ash}}(T_{ba} - T_{ref}) \quad 3.38$$

When using real gas properties for the gas mixture, it is important to apply the mixing law correctly. This involves evaluating the real gas enthalpy of each constituent at the mixture temperature (T) and its partial pressure (p_i), rather than at the mixture pressure (p). The mixing law for enthalpy is the mass-weighted average [33]. The enthalpy of the flue gas or air, with mass fractions Y, temperature T, and pressure p, can be calculated using Equation 3.39, where $h_i(T,p)$ is the enthalpy of constituent (i) at the specified temperature and pressure from property tables.

$$h_{fg/ca} = \sum_{i=1}^{k} Y_{fg/ca_i} \cdot (h_i(T,p_i) - h_i(T_{ref},p_{ref})) \quad 3.39$$

The partial pressure of each constituent of the flue gas depends on its mole fraction, as described by Dalton's law of additive pressures [33], shown in Equation 3.40. The mole fractions (X_i) can be calculated from mass fractions as shown in Equation 3.41.

$$p_i = X_i \cdot p \quad 3.40$$

$$X_i = \frac{Y_{fg/ca_i}}{M_i} M_{fg/ca} \quad 3.41$$

The boiler mass and energy balance allows for the calculation of the fuel mass flow rate. By combining this with the species mass balance, the mass flow rates of flue gas and air can be determined. Using these values, the adiabatic flame temperature can be calculated, which will be discussed in the following section.

3.4 Adiabatic Flame Temperature Model

The adiabatic flame temperature ($T_{fg_{aft}}$) is the highest theoretical temperature that the flue gas mixture can achieve at the outlet of the combustion zone, assuming no heat loss occurs to the surroundings or surfaces. This is illustrated in Figure 3.4, which outlines the control volume of the combustion zone.

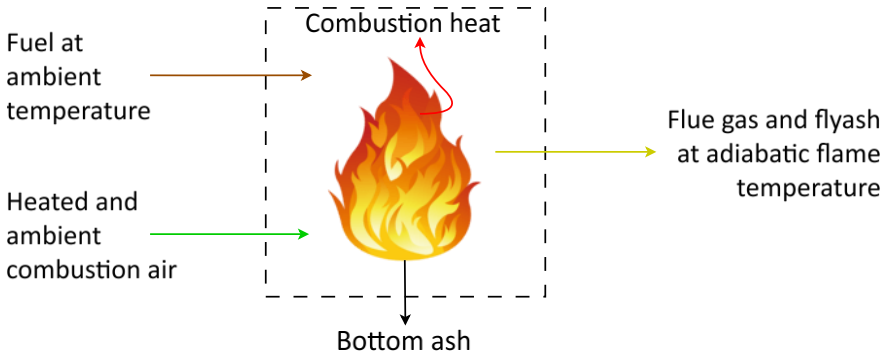

Figure 3.4: *Control volume – Combustion zone.*

The steady-state energy balance for the adiabatic combustion zone is expressed in Equation 3.42. The left-hand side represents the incoming energy, while the right-hand side represents the outgoing energy. In this equation, $\dot{Q}_{pa}$, $\dot{Q}_{sa}$ and $\dot{Q}_{da}$ are the heat inputs from the primary air, secondary air, and distribution air, respectively. $\dot{Q}_{fg_{aft}}$ and $\dot{Q}_{fa_{aft}}$ represent the heat content of the flue gas and fly ash at the adiabatic flame temperature.

$$\dot{Q}_{fuel_s} + \dot{Q}_{react} + \dot{Q}_{pa} + \dot{Q}_{sa} + \dot{Q}_{da} = \dot{Q}_{fg_{aft}} + \dot{Q}_{fa_{aft}} + \dot{Q}_{ba} \qquad 3.42$$

Equation 3.42 can be simplified to Equation 3.43 by writing the various heats as a function of their mass flow rates and enthalpies. Here, $\dot{m}_{pa}, \dot{m}_{sa}$, and $\dot{m}_{da}$ denote the mass flow rates of the primary air, secondary air, and distribution air, respectively, while h_{pa}, h_{sa} and h_{da} represent their enthalpies.

$$\dot{m}_{f_{AR}} \cdot h_{f_s} + \left(\dot{m}_{f_{AR}} \cdot HHV_f - \dot{m}_{UC} \cdot HHV_C\right) + \dot{m}_{pa} \cdot h_{pa} + \dot{m}_{sa} \cdot h_{sa} + \dot{m}_{da} \cdot h_{da} = \dot{m}_{fg} \cdot h_{fg_{aft}} + \dot{m}_{fa} \cdot h_{fa_{aft}} + \dot{m}_{ba} \cdot h_{ba} \qquad 3.43$$

Determining the enthalpy of the products, $h_{fg_{aft}}$ and $h_{fa_{aft}}$, presents a challenge because the initial temperature of the products is unknown. Therefore, determining the adiabatic flame temperature requires an iterative approach. This iterative process involves using Equations 3.39 and 3.43, where an initial temperature guess initiates the computation of enthalpies, followed by verification of the

energy balance, iterative adjustment of temperature until convergence is achieved, as illustrated in Figure 3.5.

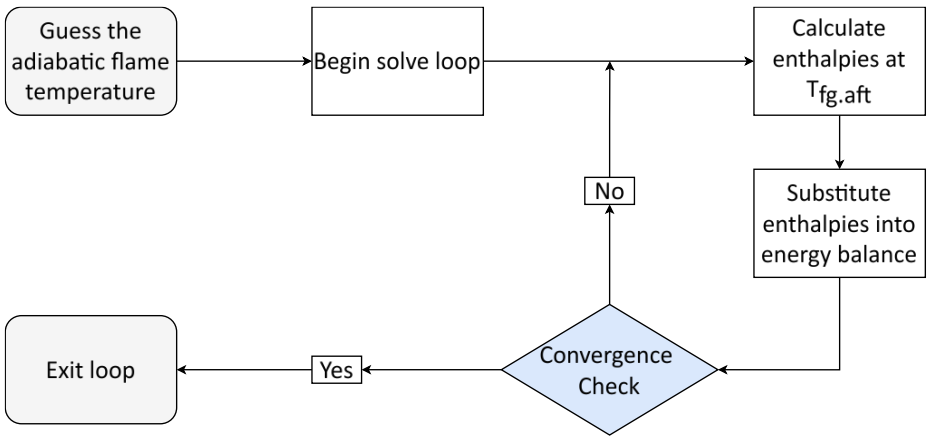

***Figure 3.5**: Solve loop – Adiabatic flame temperature.*

The figure illustrates the iterative procedure used to compute the adiabatic flame temperature, highlighting the sequential steps involved in achieving convergence. For practical implementation, the Python tool 'fsolve' is employed to automate this iterative solution process, facilitating efficient computation and convergence.

Determining the adiabatic flame temperature enables the formulation of the energy balance for the furnace, which is pivotal for evaluating furnace performance. This crucial aspect will be explored further in the subsequent section.

3.5 Zero-Dimensional Furnace Models

Figure 3.6 illustrates the relationship between the adiabatic flame temperature control volume and the 0-D model control volume. The adiabatic flame temperature facilitates the determination of the furnace exit temperature and various heat transfers.

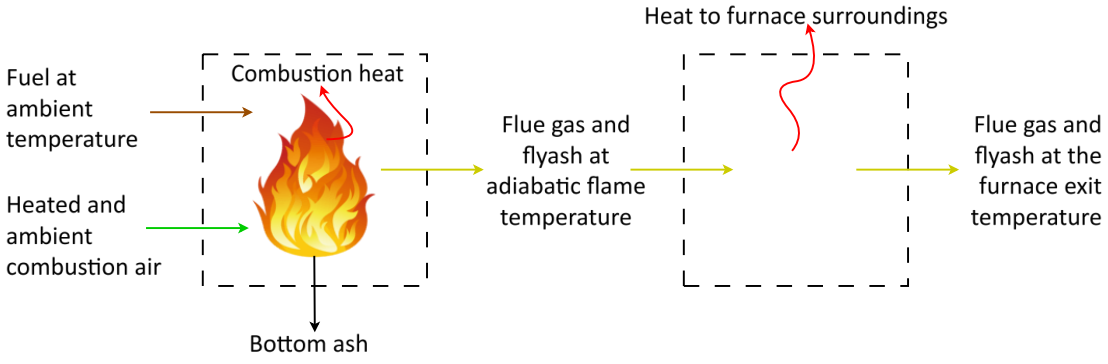

***Figure 3.6:** Control volume – 0-D furnace model.*

The 0-D furnace model serves to compute the radiation heat generated within the furnace. This radiation heat is calculated using either the direct method or the projected method, both of which assume radiation as the sole mode of heat transfer within the furnace. This simplification is justified as radiation typically accounts for approximately 95% of total heat transfer within the furnace, primarily due to the low gas velocities observed in conventional boiler systems [7].

The total heat transfer in the furnace ($\dot{Q}_{fg_{fur}}$), which is considered to be purely radiative, can be calculated by considering the total transfer from the flue gas mixture. This computation involves establishing an energy balance for gas and particle suspensions within the furnace, utilising the control volume framework depicted in Figure 3.6. The resulting equation is shown below as Equation 3.44.

$$\dot{Q}_{fg_{fur}} = \dot{m}_{fg_{fur}} \left(h_{fg_{aft}} - h_{fg_{fe}} \right) + \dot{m}_{fa} \left(h_{fa_{aft}} - h_{fa_{fe}} \right) \quad 3.44$$

The overall furnace energy balance can be expressed using Equation 3.45. Here, $\dot{Q}_{rad}$ is the total absorbed radiation within the furnace, including the radiation through the furnace exit. The coefficient φ, is the heat preservation coefficient which accounts for the heat losses from the furnace. It is calculated as $\varphi = 1 - f_{rad_{loss}}$.

$$\dot{Q}_{rad} = \varphi \dot{Q}_{fg_{fur}} \quad 3.45$$

In Equation 3.44, the enthalpy at the imaginary furnace exit plane is unknown. The enthalpy at the furnace exit depends on the mass fractions of flue gases, along with their temperature and pressure at that point, expressed as $h_{fg_{fe}} = f\left(Y_{fg}, T_{fg_{fe}}, p_{fe}\right)$. This enthalpy can be determined using Equation 3.41 once the furnace exit temperature is established. Similarly, the enthalpy of the fly ash at the furnace exit, which is contingent upon the furnace exit temperature ($h_{fa_{fe}} = f\left(T_{fg_{fe}}\right)$), can be calculated using Equation 3.37. Since the furnace exit temperature is currently unknown and cannot be directly determined, 0-D methods are employed to calculate the radiation heat transfer to the surrounding furnace surfaces, in conjunction with Equations 3.44 and 3.45.

The following sections will investigate 0-D methodologies and their practical uses. Subsection 3.5.1 will assess the projected method, focusing on its foundational assumptions and its implementation. Subsection 3.5.2 will examine the empirical correlations employed within the projected method. Subsection 3.5.3 will explore the practical application and theoretical basis of the direct method.

3.5.1 Projected Method

The net emitted radiation heat in the furnace from the flue gas to the waterwall $\left(\dot{Q}_{rad_e}\right)$ is calculated using Equation 3.46, with the detailed derivation provided in Appendix C. This equation considers the overall furnace emissivity (ε_{fur}), which depends on the state of the gas, and the Stefan-Boltzmann constant (σ_o). The total surrounding projected area (A_{rad}) includes the waterwall area, refractory area, and furnace exit plane area. Additionally, T_{fg} represents the effective gas temperature.

$$\dot{Q}_{rad_e} = \varepsilon_{fur}\sigma_o A_{rad}{T_{fg}}^4 \tag{3.46}$$

The waterwall is not a perfect blackbody and is often fouled, which impacts its ability to absorb heat. Therefore, the heat absorbed by the waterwall and the heat passing through the furnace exit plane represent only a portion of the incident radiation. To account for this, a coefficient, ψ, known as the furnace efficiency factor, is introduced to define the fraction of outgoing radiation absorbed by the heat surfaces of the wall. The calculation of ψ will be addressed in Section 3.5.2. The total net radiative heat $(\dot{Q}_{rad})$, which is the heat absorbed by the furnace and furnace exit plane, is determined using Equation 3.47. It is important to note that this value corresponds to the radiation heat described in Equation 3.47.

$$\dot{Q}_{rad} = \psi \cdot Q_{rad_e} = \psi\varepsilon_{fur}\sigma_o A_{rad}{T_{fg}}^4 \tag{3.47}$$

The overall furnace emissivity can be calculated as shown in Equation 3.48, where ε_{gp} is the effective emissivity of the flue gas and particle suspension. The calculation of A_{rad} and ε_{gp} will be discussed in Sections 3.5.2 and 3.6, respectively.

$$\varepsilon_{fur} = \frac{\varepsilon_{gp}}{\varepsilon_{gp} + (1 - \varepsilon_{gp})\psi} \tag{3.48}$$

The majority of the furnace radiation heat is absorbed by the waterwall $(\dot{Q}_{rad_{ww}})$, while a small portion is absorbed by the refractory $(\dot{Q}_{rad_{rf}})$. The remaining heat is radiated to the downstream heat exchanger through the furnace exit plane $(\dot{Q}_{rad_{fe}})$. Consequently, Equation 3.47 can be expanded into a more detailed breakdown, as shown in Equation 3.49. This expanded equation accounts for the distinct contributions of the waterwall, refractory, and the furnace exit plane to the overall heat radiation distribution within the furnace system.

$$\dot{Q}_{rad_{ww}} + \dot{Q}_{rad_{rf}} + \dot{Q}_{rad_{fe}} = \dot{Q}_{rad} = \varphi\dot{Q}_{fg_{fur}} \tag{3.49}$$

The furnace energy balance can also be expressed as in Equation 3.50, where $\overline{VC}$ is the mean overall heat capacity based on the fuel flow rate.

$$\dot{Q}_{fg_{fur}} = \dot{m}_f \overline{VC} (T_{fg_{aft}} - T_{fg_{fe}}) \quad 3.50$$

By equating Equations 3.44 and 3.50, the mean overall heat capacity is calculated as shown in Equation 3.51.

$$\overline{VC} = \frac{\dot{m}_{fg} \left(h_{fg_{aft}} - h_{fg_{fe}} \right) + \dot{m}_{fa} c_{p_{ash}} \left(T_{fg_{aft}} - T_{fg_{fe}} \right)}{\dot{m}_f \left(T_{fg_{aft}} - T_{fg_{fe}} \right)} \quad 3.51$$

The furnace energy balance can then be rewritten as shown in Equation 3.52, by combining Equations 3.44, 3.47, and 3.50.

$$\varphi \dot{m}_f \overline{VC} (T_{fg_{aft}} - T_{fg_{fe}}) = \psi \varepsilon_{fur} \sigma_o A_{rad} {T_{fg}}^4 \quad 3.52$$

Equation 3.52 then provides a relationship between $T_{fg_{fe}}$ and T_{fg}. Therefore, by solving for $T_{fg_{fe}}$, we can calculate the furnace radiation using Equations 3.44 or 3.50, and consequently determine the effective flue gas temperature using Equation 3.52. The projected method adopts a specific approach outlined in Equation 3.53 to calculate $T_{fg_{fe}}$, building upon the foundational principles presented in the furnace energy balance equation (Equation 3.52). This empirical method, widely referenced in literature [7, 8, 11, 14], leverages an empirical expression derived from the energy balance within the furnace, facilitating the determination of steady-state furnace exit temperatures. The derivation for the equation is shown in Appendix B.

$$\frac{T_{fg_{fe}}}{T_{fg_{aft}}} = \frac{{B_o}^{0.6}}{M_{fl} \cdot {\varepsilon_{fur}}^{0.6} + {B_o}^{0.6}} \quad 3.53$$

In Equation 3.53, the parameter B_o denotes the Boltzmann number, defined explicitly by Equation 3.56, while M_{fl} represents the flame modification factor, an empirical constant discussed comprehensively in Section 3.5.2. At this juncture, the direct determination of the furnace exit temperature remains unresolved due to the dependencies of B_o and ε_{fur} on $T_{fg_{fe}}$.

$$B_o = \frac{\varphi \dot{m}_f \overline{VC}}{\sigma_o \psi A_{rad} {T_{fg,aft}}^3} \quad 3.54$$

The determination of $T_{fg_{fe}}$ employs an iterative approach, utilising the adiabatic flame temperature model to establish essential parameters, $T_{fg_{aft}}$ and $h_{fg_{aft}}$. Subsequently, these parameters are

integrated with Equations 3.39, 3.48, 3.51, 3.53 and 3.54 to iteratively solve for $T_{fg_{fe}}$. Figure 3.7 illustrates the process flow diagram that outlines this iterative technique.

The iterative process commences with an initial estimation of $T_{fg_{fe}}$. This initial guess initiates the computation of ε_{fur} using Equation 3.48, followed by the determination of $h_{fg_{fe}}$ using Equation 3.39. The mean overall heat capacity is subsequently calculated using Equation 3.51, followed by the determination of the Boltzmann number via Equation 3.54. Equation 3.53 is then applied iteratively to refine $T_{fg_{fe}}$ until the convergence criteria are satisfied. For practical computational applications, the iterative solution for $T_{fg_{fe}}$is implemented using the 'fsolve' function from the scientific python (SciPy) library.

Upon achieving convergence of $T_{fg_{fe}}$, Equation 3.44 or 3.50 is employed to compute $\dot{Q}_{fg_{fur}}$. The subsequent section will discuss the empirical correlations relevant to the projected method. These correlations are instrumental in determining the distribution of heat across the surrounding surfaces.

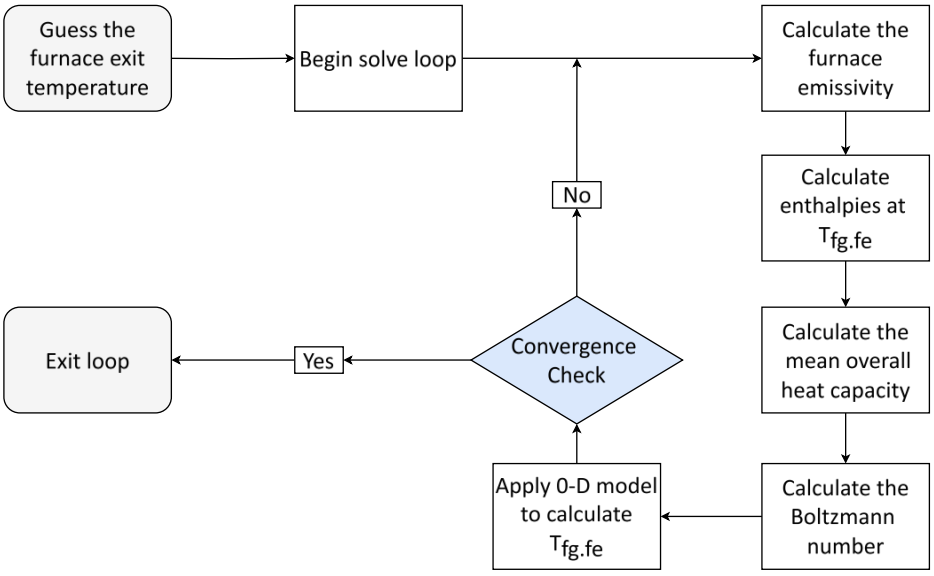

Figure 3.7: *Solve loop – Projected method.*

3.5.2 Empirical Correlations – Projected Method

The projected method utilises a combination of empirical and semi-empirical correlations aimed at calculating the furnace radiation. Central to this approach is Equation 3.53, which incorporates a flame modification factor aimed at accounting for the temperature distribution along the height of the furnace. This factor is contingent upon the type of firing system, the number of burners, and the type of fuel. The factor is determined using the empirical relationship outlined in Equation 3.55 [7].

$$M_{fl} = A' - B'(X_r + \Delta X) \quad 3.55$$

The equation above introduces ΔX as a correction factor for the actual position of the flame core. Coefficients A' and B' in the equation are parameters influenced by the type of fuel and the design of the furnace, while X_r denotes the relative height of the highest temperature zone in the furnace. For furnaces utilising travelling grate or stoker systems, typical values are $A' = 0.59$ and $B' = 0.5$, with $X_r + \Delta X = 0.14$ [7].

The furnace efficiency factor, integral to Equations 3.50 and 3.56, is another pivotal component of the projected method. It accounts for various factors, including the effect of ash deposits on tube surfaces, which diminish heat transfer efficiency due to the low thermal conductivity of ash [7]. Additionally, ψ considers variations in view factors between the hot gases and the furnace surroundings. This comprehensive analysis is consolidated into a single semi-empirical factor, as detailed in Equation 3.56. This equation represents an area-weighted average of the furnace efficiency factors of all surfaces surrounding the furnace, including those at the furnace exit plane.

$$\psi = \frac{\sum \psi_i A_{rad_i}}{A_{rad}} \quad 3.56$$

In Equation 3.56, ψ_i represents furnace efficiency factor specific to each surrounding surface, calculated using the expression $\psi_i = x_i\, \xi_i$, where x_i denotes the angular coefficient and ξ_i denotes the fouling factor. The total projected area surrounding the furnace is determined as $A_{rad} = \sum A_{rad_i}$, where A_{rad_i}denotes the specific projected area of each surrounding surface, calculated as $A_{rad_i} = x_i \cdot A_i$. Here, A_i refers to the surface area of the respective surface.

The angular coefficient x_i, utilised for membrane-type water walls, varies depending on tube spacing and diameter, and typically ranges between 0.9 and 1.0 [7]. Equation 3.57 details the calculation of this angular coefficient for membrane walls, where parameters b and d denote tube pitch and outside diameter respectively, measured in metres. Conversely, for water walls covered by refractory and the furnace exit plane, the angular coefficient is set to 1.0 [7].

$$x_w = 1.15484 \left(\frac{b}{d}\right)^{-8.50475E-1} \quad 3.57$$

The fouling factor is influenced by characteristics such as fuel properties, combustion conditions, and the design of the waterwall. It is specified as 0.6 for grate fuels, 0.1 for refractory surfaces, and 1.0 for the furnace exit [8]. Once the furnace efficiency factors for each individual surface have been calculated, Equation 3.58 can be applied to determine the radiation absorbed by the refractory ($\dot{Q}_{rad_{rf}}$) and the radiation emitted through the furnace exit plane ($\dot{Q}_{rad_{fe}}$).

$$\dot{Q}_{rad_i} = \eta_i \frac{\psi_i A_{rad_i}}{\psi A_{rad}} \dot{Q}_{rad} \quad 3.58$$

In the equation above, η_i represents the non-uniformity factor, which accounts for variations in the heat flux distribution within the furnace along its height, width, and depth. This factor depends on the assumed heat flux distribution along the furnace height and the specific location of each surface (i). A graphical representation of this distribution is typically shown in Figure 3.8, illustrating the heat flux profile across the furnace height.

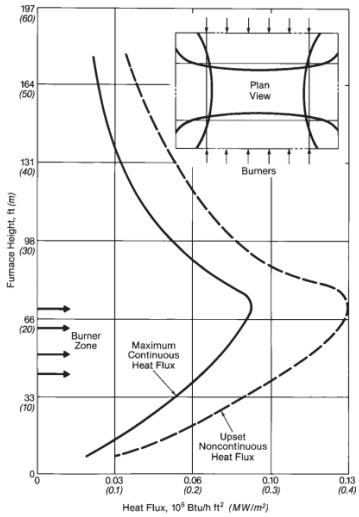

Figure 3.8: *Sample vertical furnace heat flux distribution [5].*

In the presence of a platen heating surface at the furnace exit, it is crucial to consider the coefficient of heat transfer, denoted as β (reradiation factor), between the platen and the furnace. This coefficient, as expressed in Equation 3.59, varies depending on the temperature of the flue gas at the furnace exit, and the type of fuel utilised. Its numerical value typically ranges between 0.5 and 1.0 [7].

$$\dot{Q}_{rad_{fe}} = \beta \eta_{fe} \frac{\psi_{fe} A_{rad_{fe}}}{\psi A_{rad}} \dot{Q}_{\mathrm{rad}} \quad 3.59$$

To ensure an overall energy balance for the furnace, the remainder of the heat transfer is allocated to the waterwall as shown in Equation 3.60.

$$\dot{Q}_{rad_{ww}} = \dot{Q}_{rad} - \dot{Q}_{rad_{fe}} - \dot{Q}_{rad_{rf}} \quad 3.60$$

The empirical correlations outlined in this section, combined with the foundational principles discussed in Section 3.5.1 of the projected method, facilitate the evaluation of furnace performance. The subsequent section will explore calculations using an alternative 0-D model approach.

3.5.3 Direct Method

The direct method evaluates the radiative heat transfer between the gas-solid mixture and the enclosing walls ($\dot{Q}_{rad_w}$) using Equation 3.61, with the detailed derivation provided in Appendix C. Here, ε_w denotes the emissivity of the waterwalls, typically ranging from 0.8 to 0.85 [11]. The symbol $\propto_{gp}$ represents the effective absorptivity of the flue gas and particle suspension at the wall temperature T_w. The calculation methodology for $\propto_{gp}$ will be expanded in Section 3.6. This method assumes spatial uniformity in gas temperature, density, and composition, requiring prior knowledge of gas emissivity and absorptivity for precise implementation.

$$\dot{Q}_{rad_w} = \frac{\varepsilon_w}{\propto_{gp} + \varepsilon_w - \propto_{gp} \varepsilon_w} \sigma_o (A_{rad_{ww}} + A_{rad_{rf}}) \left(\varepsilon_{gp} T_{fg}^4 - \propto_{gp} T_w^4\right) \quad 3.61$$

The radiant heat directly emitted from the furnace exit plane ($\dot{Q}_{rad_{fe}}$) and absorbed by the heat exchangers positioned downstream can be determined using Equation 3.62. Here, $\varepsilon_{w_{hx}}$ refers to the emissivity of the heat exchanger wall, while $\propto_{gp_{hx}}$ represents the gas absorptivity evaluated at the temperature of the heat exchanger wall ($T_{w_{hx}}$). This calculation assumes prior knowledge of the characteristics of the heat exchanger located after the furnace exit.

$$\dot{Q}_{rad_{fe}} = \frac{\varepsilon_{w_{hx}}}{\propto_{gp_{hx}} + \varepsilon_{w_{hx}} - \propto_{gp_{hx}} \varepsilon_{w_{hx}}} \sigma_o A_{rad_{fe}} \left(\varepsilon_{gp} T_{fg}^4 - \propto_{gp_{hx}} T_{w_{hx}}^4\right) \quad 3.62$$

Incorporating the thermal resistances associated with each surface within the furnace (refractory and water wall), the energy balance at the surrounding furnace wall is expressed by Equation 3.63. Here, T_{sat} denotes the saturation temperature of the water, and UA represents the overall heat transfer coefficient.

$$\dot{Q}_{rad_w} = UA(T_w - T_{sat}) = \frac{T_w - T_{sat}}{R_w} \quad 3.63$$

The overall heat transfer coefficient of the furnace wall is expressed in relation to the effective thermal resistance of the furnace wall (R_w), as shown in Equation 3.64, and is influenced by the specific geometric configuration of the system.

$$UA = \frac{1}{R_w} = \sum \frac{1}{R_i} \quad 3.64$$

In Equation 3.64 R_i denotes the thermal resistance associated with each physical surface (i). The thermal resistance for the waterwall and refractory can be determined using Equation 3.65.

$$R_i = \frac{1}{h_i A_i} + \frac{x_i}{k_i A_i} + \frac{\xi_i}{A_i} \quad 3.65$$

In Equation 3.65, h_i is the heat transfer coefficient for nucleate boiling, which is common in many industrial applications, the heat transfer coefficient is usually around $10\,000$ to $20\,000$ $\frac{W}{m^2 K}$ [5]. The thermal conductivity k_i is assumed to be 47 $\frac{W}{m \cdot K}$ for the waterwall and 1.4 $\frac{W}{m \cdot K}$ for the refractory [35]. A_i and x_i represent the area and thickness associated with each surface (i). The fouling factor (ξ) represents the additional thermal resistance introduced by fouling. For biomass-fired boiler waterwalls, a fouling resistance of $0.0018 \frac{m^2 K}{W}$ was assumed [6]. The heat transfer to each individual physical surface can be computed using Equation 3.66 for the waterwall and Equation 3.67 for the refractory.

$$\dot{Q}_{rad_{ww}} = \frac{T_w - T_{sat}}{R_{ww}} \quad 3.66$$

$$\dot{Q}_{rad_{rf}} = \frac{T_w - T_{sat}}{R_{rf}} \quad 3.67$$

The total heat transfer to the furnace walls is the sum of the heat transfer to the waterwalls plus that to refractory as shown in Equation 3.68.

$$\dot{Q}_{rad_w} = \dot{Q}_{rad_{ww}} + \dot{Q}_{rad_{rf}} \quad 3.68$$

Therefore, the total radiation heat in the furnace can be calculated using Equation 3.69, which has been included here for completeness and is identical to Equation 3.48.

$$\dot{Q}_{rad_w} + \dot{Q}_{rad_{fe}} = \dot{Q}_{rad} = \varphi \dot{Q}_{fg_{fur}} \quad 3.69$$

The solution of the radiative heat transfer using the direct method requires an iterative approach due to several unknowns: the effective gas temperature, the wall temperature, and the effective emissivity and absorptivity, which depend on the flue gas and wall temperatures, respectively. Given the indeterminate nature of T_{fg} and the absence of a direct or iterative means to determine it, Equations 3.61 and 3.62 are applied under the assumption that T_{fg} is equivalent to $T_{fg_{fe}}$ [6]. Therefore, by employing Equations 3.44, 3.61 - 3.63 and 3.69, iterative methods can be applied to solve for the furnace exit temperature and the wall temperature, as illustrated in Figure 3.9.

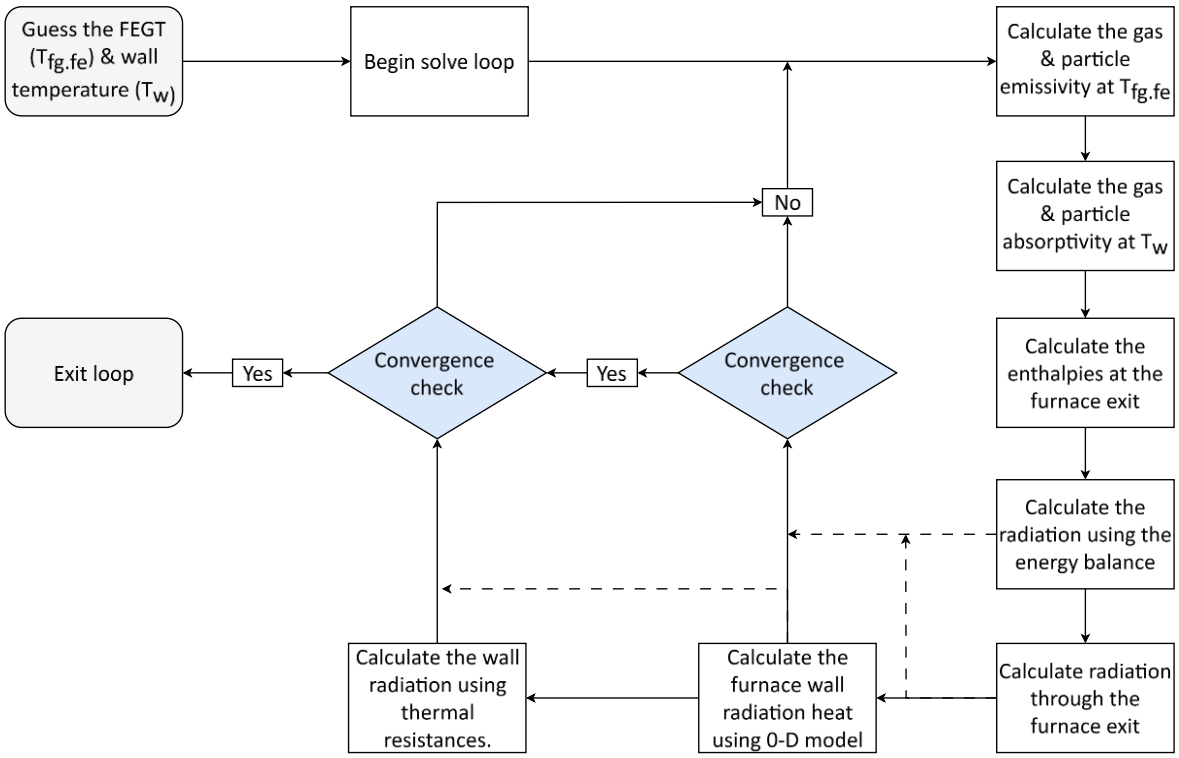

Figure 3.9: *Solve loop – Direct method.*

In Figure 3.9, two convergence checks ensure the energy balance of the furnace. The first convergence check, performed using Equation 3.69, involves calculating $\dot{Q}_{fg_{fur}}$ with Equation 3.44 and $\dot{Q}_{rad_w}$ with the 0-D model equation (Equation 3.61). The second convergence check compares the radiation to the wall, calculated using the 0-D model equation (Equation 3.61), to the value calculated from the idea of the thermal resistance of the wall (Equation 3.63). For a solution to be considered converged, both energy balances must be satisfied. These convergence checks ensure the accurate determination of the wall and furnace exit temperatures. The 'fsolve' function from the SciPy library was used in the Python model to facilitate efficient computation.

The direct method involves fewer empirical correlations compared to the projected method. However, as discussed above, it presents complexities such as the unknown effective gas temperature and the requirement for prior information regarding the heat exchanger located immediately after the furnace exit, thereby complicating the calculation process. The subsequent section will focus on determining the emissivity and absorptivity of the flue gas and particle suspension. These parameters are crucial for both the projected and direct methods of calculation.

3.6 Thermal Radiation Models for Gas-Solid Suspensions

The effective emissivity and absorptivity can be determined using the standard model, low ash model, or high ash model. The presence of fly ash in the combustion gas flow of a boiler significantly enhances the radiant energy emitted by the hot combustion gases due to scattering effects, thereby influencing the emissivity of the flue gas. The concentration of ash particles within the combustion gas, denoted as the particle load (L_p), is calculated according to Equation 3.70. A higher particle load results in greater scattering effects and more radiant energy emitted by the flue gas. These effects become significant at particle loads exceeding $0.005\ \frac{kg_{fa}}{m_{fg}^3}$, necessitating the use of the high ash model in such conditions [14].

$$L_p = \frac{\dot{m}_{fa}}{\left(\frac{\dot{m}_{fg}}{\rho_{fg}}\right)} \tag{3.70}$$

It is generally recommended to use the more advanced coupling calculation model, even in scenarios with low particle loads [6, 11]. Since the ash content of biomass is typically very low, the high ash model is not expected to perform better than the standard model in this case. Despite this, this study will compare the standard and high ash models, which will be detailed in sub-sections 3.6.1 and 3.6.2, respectively.

3.6.1 Standard Model

The model discussed in [7, 8] specifically concentrates on calculating the emissivity of flue gas and particle suspensions, excluding considerations for absorptivity. The emissivity is determined by Equation 3.71, where k_{fur} represents the effective coefficient of radiant absorption in units of $\frac{1}{m \cdot MPa}$, p_{fur} denotes the pressure of gases within the furnace in MPa, and S_{fur} denotes the mean beam length in metres.

$$\varepsilon_{gp} = 1 - e^{-k_{fur} p_{fur} S_{fur}} \tag{3.71}$$

The mean beam length is the average thickness of the radiating gas layer, which can be determined using Equation 3.72, which relates it to the furnace volume V_{fur} in cubic metres and the total surface area A_{fur} in square metres surrounding this volume. Thus, a thicker gas layer results in more intense radiation.

$$S_{fur} = 3.6\frac{V_{fur}}{A_{fur}} \quad 3.72$$

Equation 3.73 is employed for the computation of k_{fur}, integrating contributions from triatomic gas radiation ($k_g\, r_g$), absorption resulting from fly ash ($k_{fa}\, \mu_{fa}$), and radiation emitted by coke and carbon black particles ($10c_1\, c_2$).

$$k_{fur} = k_g\, r_g + k_{fa}\, \mu_{fa} + 10c_1\, c_2 \quad 3.73$$

The coefficients c_1 *and* c_2 are determined based on the type of fuel and firing method, respectively. For wood, $c_1 = 0.5$, and for grate firing, $c_2 = 0.03$ [7]. The coefficient k_g, expressed in units $\frac{1}{m \cdot MPa}$, represents the coefficient attributed to triatomic gas, and it can be computed using Equation 3.74. Here, r_g denotes the volume fraction of triatomic gas, where $r_g = r_{H_2O} + r_{CO_2} + r_{SO_2}$. The volume fractions of H_2O, CO_2 *and* SO_2 in the flue gas mixture are denoted by r_{H_2O}, r_{CO_2}, r_{SO_2}, respectively. The volume fraction (r_i) is equivalent to the mole fraction (X_i), which is determined using Equation 3.41. T_{fg} represents the gas temperature in Kelvin, and the furnace pressure is specified in MPa.

$$k_g = \left(\frac{7.8 + 1.6 r_{H_2O}}{3.16\sqrt{r_g p_{fur} S_{fur}}} - 1\right)\left(1 - 0.37\frac{T_{fg}}{1000}\right) \quad 3.74$$

The coefficient k_{fa} signifies the radiation absorption attributed to fly ash, determined by Equation 3.75. Here, ρ_{fg_n} denotes the density of flue gas under standard conditions ($101325\ kPa, 0\ ℃$), and d_p represents the average diameter of fly ash particles in micrometres μm. The parameter μ_{fa} represents the mass fraction of fly ash in the flue gas and particle suspension, calculated according to Equation 3.76.

$$k_{fa} = \frac{48350\rho_{fg_n}}{({T_g}^2 {d_p}^2)^{\frac{1}{3}}} \quad 3.75$$

$$\mu_{fa} = \frac{\dot{m}_{fa}}{\dot{m}_{fa} + \dot{m}_{fg}} \quad 3.76$$

The projected method does not incorporate absorptivity in its computations, whereas the direct method requires an absorptivity value. In this study, absorptivity calculations mirror those for emissivity, with the distinction that the gas temperature (T_{fg}) is substituted by the wall temperature (T_w).

3.6.2 High Ash Model

The total emissivity and absorptivity of the gas-solid mixture can be determined using Equations 3.77 and 3.78, respectively.

$$\varepsilon_{gp} = (1-\beta)\left(\frac{1-e^{-\phi_{\varepsilon gp}}}{1-\beta e^{-\phi_{\varepsilon gp}}}\right) \quad 3.77$$

$$\propto_{gp} = (1-\beta)\left(\frac{1-e^{-\phi_{\propto gp}}}{1-\beta e^{-\phi_{\propto gp}}}\right) \quad 3.78$$

Equations 3.77 and 3.78 define β as a function of the scattering factor γ, as indicated by Equation 3.79. The optical thicknesses for emission and absorption of the gas-particle mixture, denoted as $\phi_{\varepsilon_{gp}}$ and $\phi_{\propto_{gp}}$ respectively, are computed according to Equations *3.80* and *3.81*.

$$\beta = \frac{\gamma-1}{\gamma+1} \quad 3.79$$

$$\phi_{\varepsilon_{gp}} = (\bar{Q}_{abs} A_p L_p + K_{\varepsilon_g}) S_{fur} \quad 3.80$$

$$\phi_{\propto_{gp}} = (\bar{Q}_{abs} A_p L_p + K_{\propto_g}) S_{fur}\, \gamma \quad 3.81$$

In the equations above, γ is determined using Equation 3.82, where $\bar{Q}_{bsc}$ and $\bar{Q}_{abs}$ represent the mean relative efficiencies for backscattering and absorption, respectively. The particulate area A_p is calculated using Equation 3.83, where ρ_p denotes the ash particulate density and d_p is the mean particle diameter. The coefficients K_{ε_g} and $K_{\propto_g}$, which characterise the emission and absorption in the gas phase, are derived from definitions of emissivity (ε_g) and absorptivity $(\propto_g)$, as detailed in Equations 3.84 and 3.85, respectively.

$$\gamma = \left(1 + \frac{2\bar{Q}_{bsc}}{\bar{Q}_{abs}}\right)^{\frac{1}{2}} \quad 3.82$$

$$A_p = \frac{3}{2\rho_p d_p} \quad 3.83$$

$$K_{\varepsilon_g} = -\,ln\left(\frac{1-\varepsilon_g}{S_{fur}}\right) \quad 3.84$$

$$K_{\propto_g} = -\ln\left(\frac{1-\propto_g}{S_{fur}}\right) \quad 3.85$$

The emissivity of the flue gas mixture is calculated using the weighted sum of grey gases model (WSGGM) [6]. This model applies specifically to a gas mixture containing H_2O and CO_2 under a total pressure of $p = 1\ bar$, with a ratio of partial pressures $0.5 < \frac{p_{H_2O}}{p_{CO_2}} < 2$. Equation 3.86 provides the method to determine the emissivity of the flue gas mixture at temperature T_{fg} using the WSGGM.

$$\varepsilon_g(T_{fg}) = \sum_{i=1}^{3}\left[(b_{1_i} + b_{2_i}\frac{T_{fg}}{1000K})(1 - e^{-k_i(p_{H_2O}+p_{CO_2})S_{fur}})\right] \quad 3.86$$

The coefficients required for the calculations using the equation above are listed in Table 3-1 below.

Table 3-1: *Coefficients for the emissivity equation [6].*

$(\boldsymbol{i})$	$\boldsymbol{b_{1_i}}$	$\boldsymbol{b_{2_i}}$	$\boldsymbol{k_i\left(\frac{1}{m \cdot bar}\right)}$
1	0.130	0.000265	0
2	0.595	-0.00015	0.824
3	0.275	-0.000115	25.91

The absorption coefficients can be calculated using the same equation and coefficients, where the temperature of the emitting wall (T_w) is substituted instead of the temperature of the gas (T_{fg}), as shown in Equation 3.87.

$$\propto_g (T_w) = \sum_{i=1}^{3}\left[(b_{1_i} + b_{2_i}\frac{T_w}{1000K})(1 - e^{-k_i(p_{H_2O}+p_{CO_2})S_{fur}})\right] \quad 3.87$$

The quantities $\bar{Q}_{abs}$ and $\bar{Q}_{bsc}$ are determined using a two-flux model developed by Biermann and Vortmeyer [6], specifically designed for assessing particle emissivity while accounting for scattering effects. In this model, the total scattered radiation is divided into forward and backward fractions (backscattering). Forward scattering is considered to have no impact on radiation due to the assumption in the two-flux model that incident and scattered radiation share the same direction.

However, backward scattering reduces emissivity by redirecting radiation in the opposite direction. It was observed that nearly half of the listed fly ashes exhibit very similar optical properties. Consequently, representative curves were derived for fly ash, depicting mean relative efficiencies for absorption $\bar{Q}_{abs}$ and, more significantly, for backscattering $\bar{Q}_{bsc}$, as illustrated in Figure 3.10.

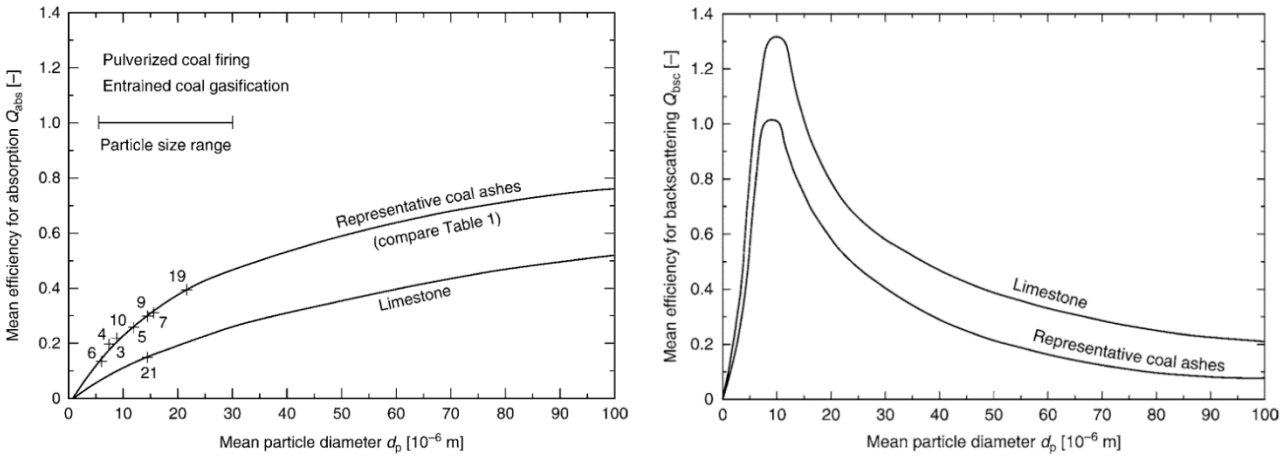

Figure 3.10: *Mean efficiency of absorption and backscattering graphs [6].*

For computational convenience, Laubscher and Rousseau [36] introduced correlations in Equations 3.88 and 3.89, which were derived from the data presented in Figure 3.10. These equations are applicable when the particle diameter d_p is expressed in micrometres (μm). It should be noted that these correlations are valid only within the range of mean particle diameters from $0\ \mu m$ to $100\ \mu m$.

$$\bar{Q}_{abs} = 0.275 d_p^{0.298} - 0.305 \tag{3.88}$$

$$\bar{Q}_{bsc} = \frac{6.2188 \cdot 10^{-3} - 1.0492 \cdot 10^{-2} \cdot d_p + 7.287 \cdot 10^{-3} \cdot d_p^2 - 2.1925 \cdot 10^{-5} \cdot d_p^3}{1.851 \cdot 10^{-1} - 2.0405 \cdot 10^{-3} \cdot d_p^2 + 6.254 \cdot 10^{-3} \cdot d_p^3} \tag{3.89}$$

Table 3-2 presents the computed mean relative efficiencies for absorption and backscattering corresponding to larger particle diameters. The values are provided as a function of the mean particle diameter.

For mean particle diameters exceeding $100\ \mu m$ and up to $500\ \mu m$, correlations were established using data from Table 3-2 to aid in computational calculations, detailed in Equations 3.90 and 3.91.

$$\bar{Q}_{abs} = 0.5888 + 2.120 \cdot 10^{-3} \cdot d_p - 2.834 \cdot 10^{-6} \cdot d_p^2 - 5.535 \cdot 10^{-9} \cdot d_p^3 + 1.050 \cdot 10^{-11} \cdot d_p^4 \tag{3.90}$$

$$\bar{Q}_{bsc} = 0.1788 - 0.001105 \cdot d_p + 1.516 \cdot 10^{-6} \cdot d_p^2 - 3.165 \cdot 10^{-9} \cdot d_p^3 - 6.095 \cdot 10^{-9} \cdot d_p^4 \quad 3.91$$

For mean particle diameters greater than $500\ \mu m$, the mean relative efficiencies for absorption and scattering were fixed at $\bar{Q}_{abs} = 0.906$ and $\bar{Q}_{bsc} = 0.020$. The high ash model can then be applied in a straightforward manner once d_p, T_w and T_{fg} are known.

Table 3-2: *Mean relative efficiencies for absorption and backscattering [6].*

Mean particle diameter $(\boldsymbol{\mu m})$	**Representative coal ashes**	
	$\bar{\boldsymbol{Q}}_{\boldsymbol{abs}}$	$\bar{\boldsymbol{Q}}_{\boldsymbol{bsc}}$
100	0.768	0.086
200	0.872	0.034
350	0.904	0.022
500	0.905	0.020
>1000	0.906	0.020

3.7 Summary

The methodology outlined the sub-models integral to the 0-D method. From the 0-D calculation procedure presented, it is evident that the process is quite complex. Among the different variations of 0-D methods, including low ash, high ash, and standard models, the discussion focused on the high ash and standard models. Implementing these 0-D models requires prior knowledge of boiler performance, specifically details such as the flue gas exit temperature at the final heat exchanger. This information can be directly measured or estimated based on typical boiler performance data.

The subsequent section will examine case studies where these 0-D models have been applied.

4. Case Study Boilers

This chapter presents a detailed examination of two biomass-fired boilers, which serve as case studies for analysing the 0-D furnace models presented in this research. These case study boilers have been analysed in studies by Rousseau and Laubscher, from which the geometrical and operational data have been sourced [11, 14, 35].

The first case study features a compact biomass-fired boiler, while the second focuses on a larger industrial biomass-fired boiler. Subsequent sections provide an in-depth look at each boiler, comparing their relative sizes, designs, and operational layouts.

4.1 Case Study 1 – Compact Biomass-Fired Boiler

The first case study examines the MicroGen-X boiler. Illustrated in Figure 4.1 is the MicroGen-V boiler, a model closely resembling the MicroGen-X. Developed by John Thompson, the MicroGen boiler (X and V) addresses the increasing demand for small to medium pressure power boilers suitable for biomass applications. The MicroGen-X is a compact industrial semi-suspension biomass-fired water-tube boiler, with a nominal steam capacity of 45 t/h and a net electrical output of 10 MWe [37]. The following sections detail the design of the boiler and key operating conditions.

Figure 4.1: *Image of the MicroGen boiler [37].*

4.1.1 Boiler Design

The compact boiler features a single drum configuration with a membrane wall furnace and an evaporator tube bank. The furnace design incorporates a continuous ash discharge (CAD) stoker and a pneumatic fuel spreader that feeds sugarcane bagasse onto a moving grate. This configuration supports suspension-firing of small, light biomass fractions while allowing heavier solid fuel particles to combust on the grate.

A schematic of the boiler layout is shown in Figure 4.2. The boiler is equipped with a comprehensive heat recovery tower, including a tubular air heater and extended surface economiser banks. Combustion air is supplied via distribution air for fuel spreading, primary air from below the grate, and secondary air injected into the freeboard from the rear wall and 12 interlacing sidewall nozzles. The secondary superheater is located just downstream of the furnace exit plane, followed by screen tubes, a large downward flow cavity, more screen tubes, the primary superheater, and two evaporator banks.

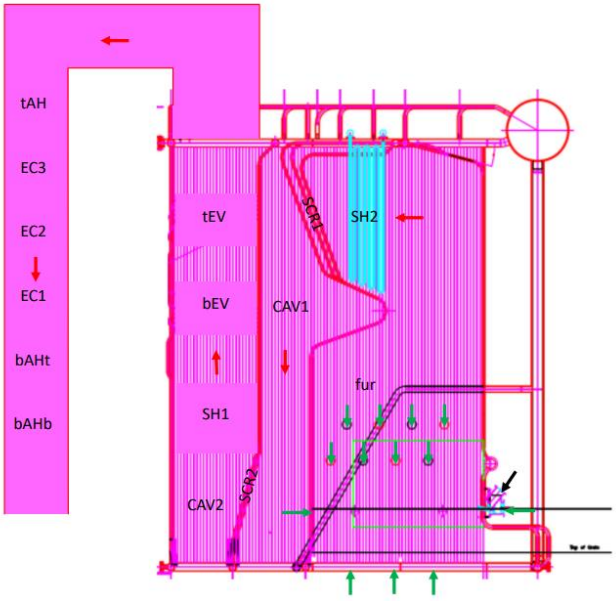

Figure 4.2: *Case study 1 – Boiler layout.*

The high moisture content of the fuel poses a challenge due to the significant latent heat of vaporisation, creating a large heat sink in the lower furnace and affecting combustion stability. To mitigate this, the lower furnace membrane walls are partially covered with castable refractory, and heated primary air is supplied to the lower furnace zone. These design features increase local gas temperatures, aiding fuel moisture evaporation and enhancing combustion stability. The total planar surface areas of the furnace membrane walls, and refractory-covered walls are approximately 152 m² and 27 m², respectively.

4.1.2 Boiler Operating Conditions

The boiler is designed to generate steam at 485°C and 6.8 MPa, with feedwater supplied at 130°C. Figure 4.3 presents the process flow diagram, illustrating the interactions among the air, water, and flue gas streams with various heat exchangers.

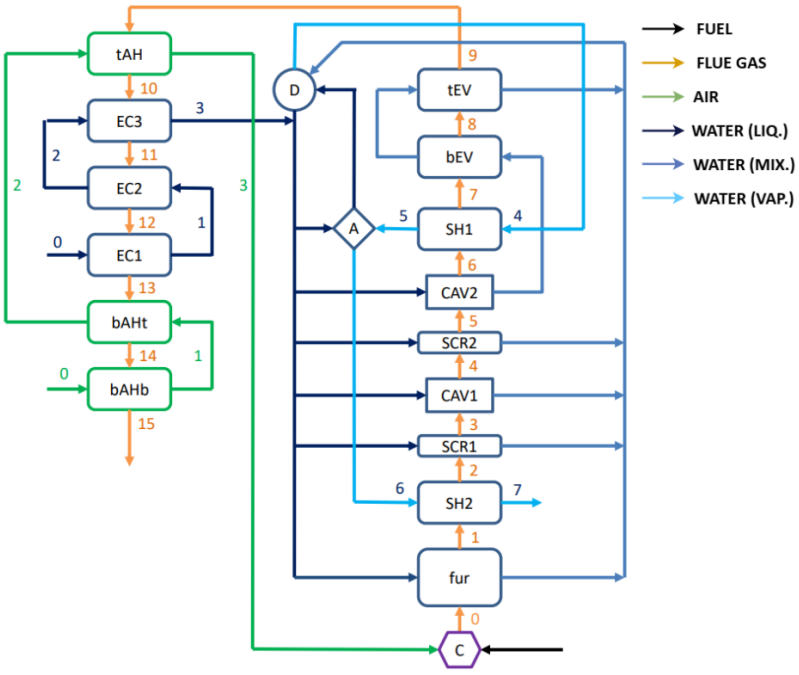

Figure 4.3: *Case study 1 – Process flow diagram.*

The fuel properties are summarised in Table 4-1, highlighting a significant moisture content of 50% and a HHV of 8.838 MJ/kg, as well as the low ash content of less than 5%.

Table 4-1: *Case study 1 – Fuel properties [37].*

Proximate analysis			**Ultimate analysis**	
Components	**Wt. (%)**		**Components**	**Wt. (%)**
Volatiles	39.5		C	47.88
Fixed carbon	5.8		H	5.91
Ash	4.7		O	45.82
Moisture	50.0		N	0.35
HHV [MJ/kg]	8.838		S	0.04

4.2 Case Study 2 – Industrial Biomass-Fired Boiler

The second case study examines the Ubombo boiler, depicted in Figure 4.4. Also developed by John Thompson, this boiler supplies process steam and power to a sugarcane mill, with excess power exported to the national grid. The boiler is a semi-suspension biomass-fired water-tube boiler with a nominal steam capacity of 105 t/h. The following sections detail the design of the boiler and key operating conditions.

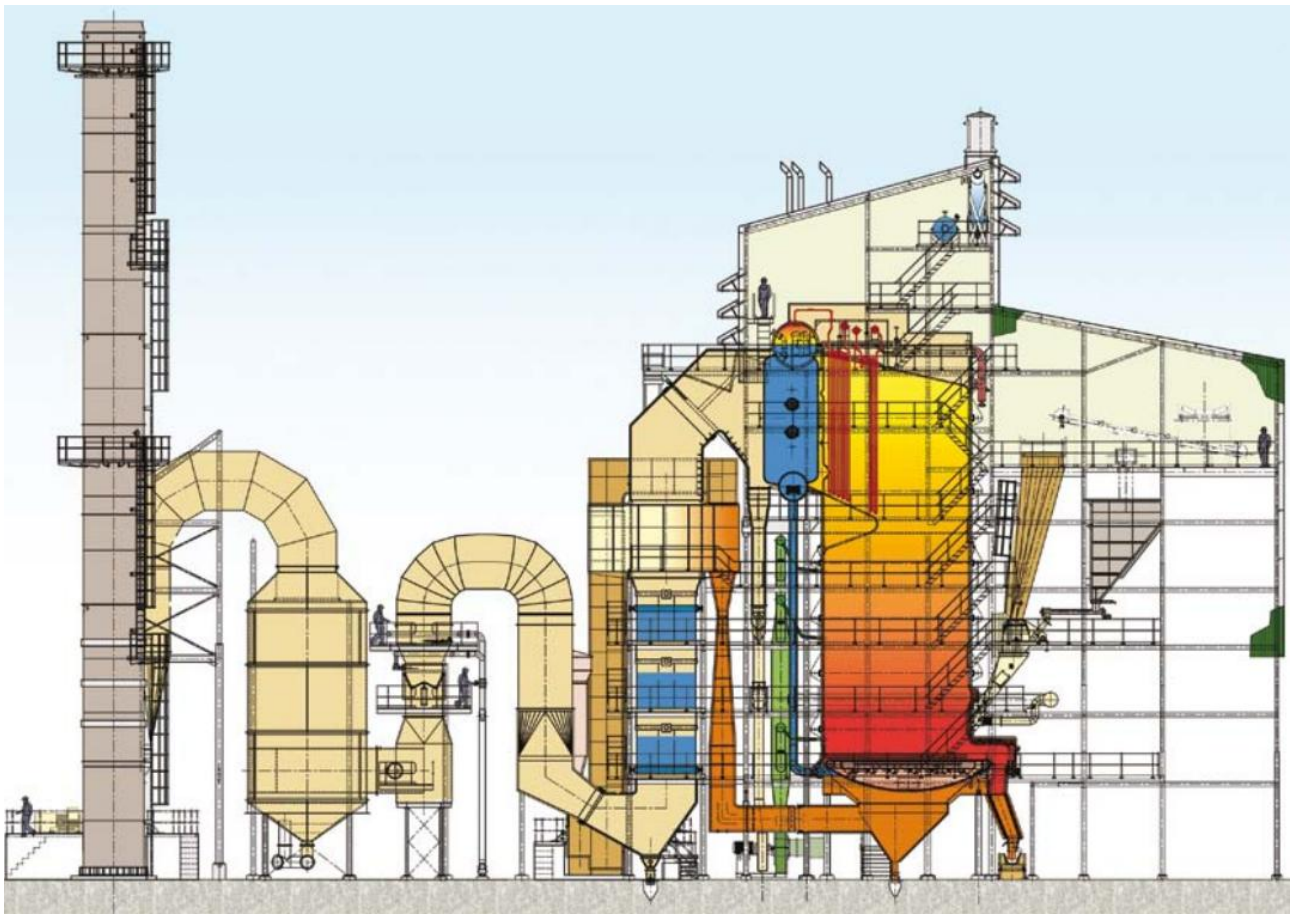

Figure 4.4: *Schematic diagram of the Ubombo boiler [38].*

4.2.1 Boiler Design

The industrial boiler features a membrane-wall furnace, a single pass main bank, two-stage controlled superheaters with venturi-type spray attemperators, an evaporator tube bank, a single-pass tubular air heater, and an extended-surface economizer. The furnace includes a zoned CAD stoker, and bagasse is fed onto the moving grate using three-drum feeders and a pneumatic spreading system that distributes the fuel to the rear of the furnace. The grate motion gradually transports fuel and ash from the rear to the front ash discharge zone.

The layout of the boiler is shown in Figure 4.5. Combustion air is supplied from three sources: distribution air for fuel spreading, heated primary air supplied through the grate, and secondary air injected into the freeboard from the rear wall through 48 nozzles to increase lower furnace turbulence and ensure complete burnout. The air heater is a single-bank crossflow unit, partially bypassed to control under-grate air temperature, preventing grate overheating. The refractory provides the thermal inertia necessary to combust biomass with varying moisture contents. The total planar surface areas of the furnace membrane walls, and refractory-covered walls are approximately 433 m² and 35 m², respectively.

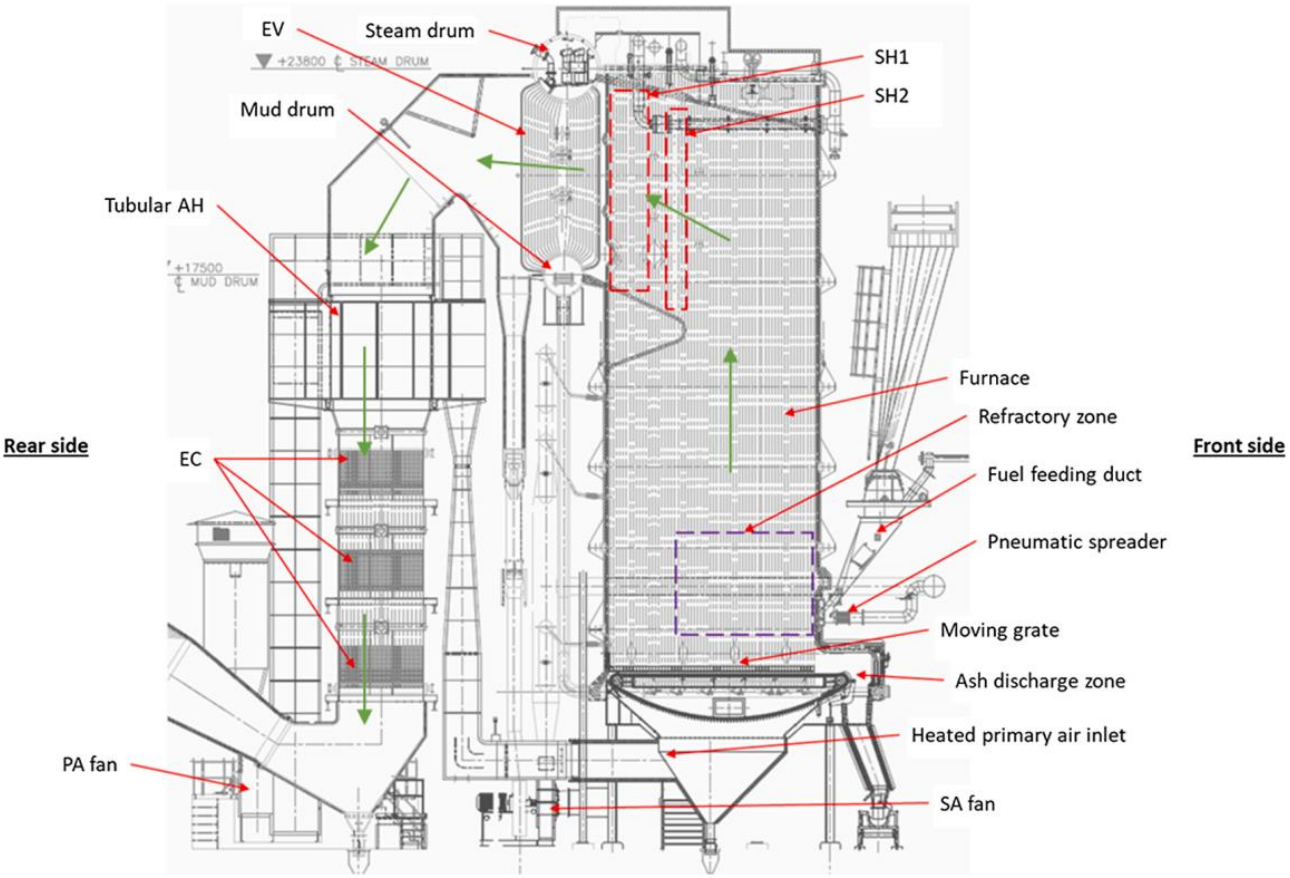

Figure 4.5: *Case study 2 – Boiler layout [14].*

4.2.2 Boiler Operating Conditions

The boiler is designed to generate steam at 450°C and 4.5 MPa, with feedwater supplied at 112°C. Figure 4.6 presents the process flow diagram, which reveals that while Case Study 1 and Case Study 2 share similar overall configurations, there are important distinctions in their design. Case Study 2 includes a condenser, a component not found in Case Study 1. Conversely, Case Study 1 incorporates

two screens, and an additional heat exchanger positioned after the economiser to facilitate heat recovery, a feature absent in Case Study 2.

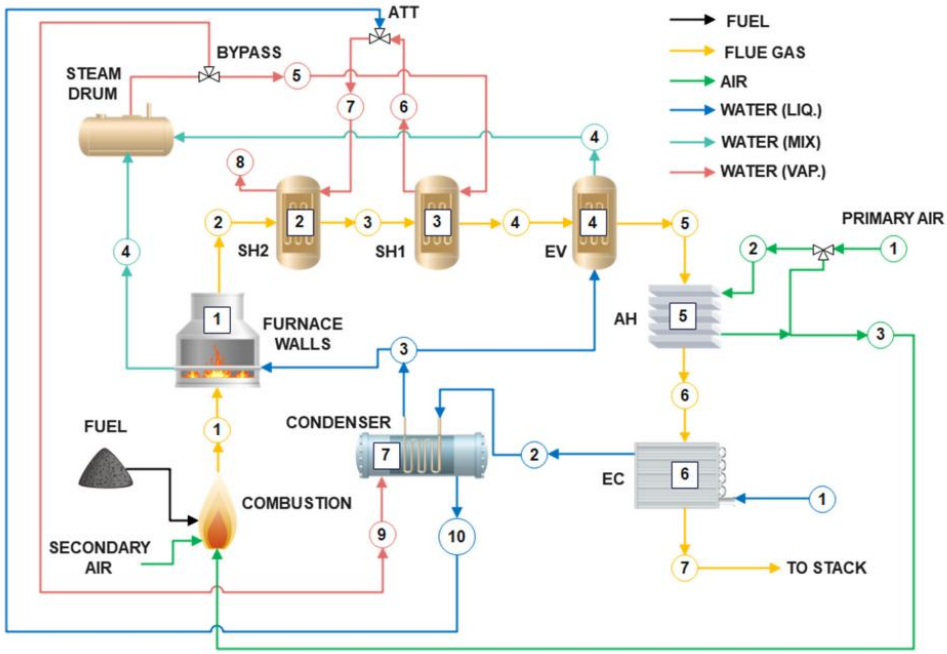

Figure 4.6: *Case study 2 – Process flow diagram [11].*

The fuel properties are summarised in Table 4-2, again highlighting a significant moisture content of 49.6% and an HHV of 8.894 MJ/kg, as well as the low ash content of less than 5%.

Table 4-2: *Case study 2 – Fuel properties [35].*

Proximate analysis			**Ultimate analysis**	
Components	**Wt. (%)**		**Components**	**Wt. (%)**
Volatiles	39.8		C	47.88
Fixed carbon	5.9		H	5.91
Ash	4.7		O	45.82
Moisture	49.6		N	0.35
HHV [MJ/kg]	8.894		S	0.04

On-site measurements for various operating conditions, used for modelling the case study in Python and CFD models, are shown in Table 4-3.

Table 4-3: *Case study 2 – On-site measurements [14].*

			100 t/h load case	**65 t/h load case**
Parameter	**Node**	**Units**	**Mean of measurements**	**Mean of measurements**
Water side				
EC inlet temperature	1	K	370.2	370.2
EC outlet temperature	2	K	460.2	438.0
Steam drum pressure	5	kPa	3115.2	3137.9
SH1 outlet temperature	6	K	661.6	645.1
SH2 outlet temperature	8	K	674.4	675.0
SH2 outlet pressure	8	kPa	2773.0	3095.5
SH2 outlet mass flow rate	8	kg/s	28.8	18.8
Spray water temperature	10	K	487.0	509.9
Flue gas side				
EV outlet temperature	5	K	701.2	643.9
AH outlet temperature	6	K	570.9	522.0
EC outlet temperature	7	K	445.2	410.5
Air side				
AH inlet temperature	1	K	298.5	305.0
AH outlet temperature	3	K	492.2	473.2

4.3 Summary

This chapter introduced the case study boilers utilised in this study. The first case study examines a smaller, compact boiler, while the second investigates a larger industrial-scale boiler. The substantial size disparity between the boilers is detailed in Table 4-4, which clearly demonstrates the larger dimensions and greater capacity of the Ubombo boiler (Case study 2) compared to the MicroGen-X boiler (Case Study 1). This difference in size provides a valuable opportunity to evaluate the performance of furnace models across different scales.

Table 4-4: *Comparison of boiler furnace geometries.*

Description	**Case study 1**	**Case Study 2**	**Ratio**
Furnace height	12.0 m	19.0 m	1.6
Waterwall surface area	152.1 m^2	432.6 m^2	2.8
Refractory surface area	26.7 m^2	34.6 m^2	1.3
Furnace exit plane area	19.8 m^2	44.1 m^2	2.2
Furnace volume	184.1 m^3	636.8 m^3	3.5

The following section will outline the modelling methodology for the CFD models, along with the validation process and post-processing techniques employed to analyse the data.

5. CFD Model of Case Studies

The steady-state CFD boiler models for the case studies were previously developed within the ATProM research unit at UCT using ANSYS® Fluent 2023 R1. These models, verified and validated in prior studies [35], involve the simulation of the biomass-fired boilers by solving fundamental conservation equations for mass, momentum, energy, and species transport. Additionally, various sub-models are integrated to accurately capture the complex physical and chemical processes occurring within the boiler. Given the availability of these CFD models, they were employed in the current study to serve as a baseline for evaluating the accuracy of the 0-D furnace models. The aim and scope of the current study therefore did not include the development of the CFD models. However, for the sake of completeness, Section 5.1 provides a detailed overview of the CFD modelling methodology.

5.1 CFD Modelling Methodology

The CFD boiler furnace model integrates chemical kinetics, flow, turbulence, and radiation, as illustrated in Figure 5.1. This methodology systematically outlines the major components involved in modelling the combustion process in a biomass-fired boiler. For simplicity, the detailed equations are not discussed in this section. The full model descriptions and equations can be found in [35].

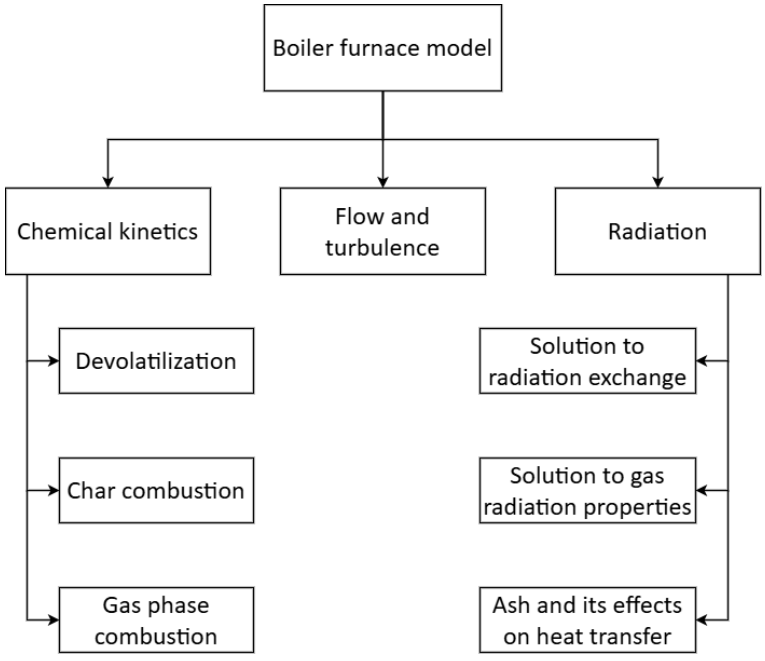

Figure 5.1: *CFD sub-models for the furnace [39].*

The combustion process of biomass particles begins with particle heating, followed by moisture loss during the drying stage, release of volatile materials during devolatilisation, and combustion of char (fixed carbon), as depicted in Figure 5.2. Ash remains as the final solid product, with some unburnt carbon trapped within it. The remaining ash can exit the boiler as fly ash (finer particles) or bottom ash (coarser particles).

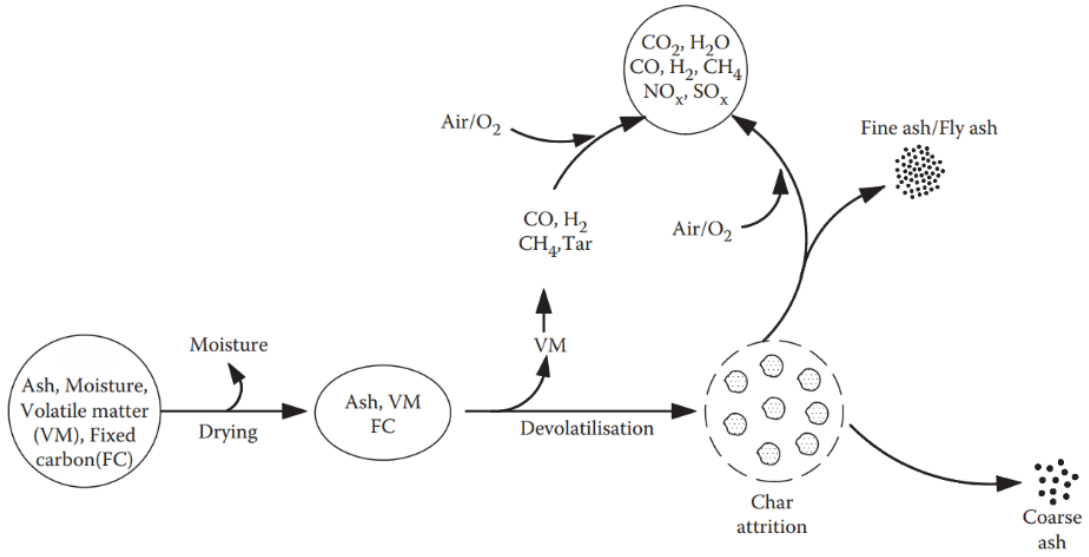

Figure 5.2: *Particle-level processes during the combustion of solid fuel* [40].

The drying phase, involving the evaporation of moisture in the biomass, was modelled using an independent droplet model. The thermal decomposition (devolatilisation) of biomass into volatiles and char was modelled using a single-step Arrhenius-type kinetic rate model, which predicts the volatile yield and reaction rate. The model assumes that the heating rate of particles is much faster than the chemical reactions involving bond breakage.

Char combustion was modelled assuming that it does not commence until devolatilisation is complete. The combustion was considered to be influenced by both physical control (oxygen diffusion to the surface) and chemical control (oxygen combining with carbon). The char oxidation reaction in this study produces CO and was modelled using a kinetic-diffusion limited rate surface reaction model.

The species-transport approach was used to model the multi-species mixture, solving a transport equation for each chemical constituent in the reaction mechanism. Gas-phase reaction rates for volatile and CO oxidation were calculated using the eddy-dissipation/finite rate turbulence-chemistry interaction model, which considers reaction rates dependent on mean species concentration and turbulent mixing.

Given the inherently turbulent nature of boiler flows due to high air and gas velocities, the mass, momentum, and energy conservation equations for the gas phase were solved using Reynolds-averaged forms. These equations were complemented by the realizable k-ε model to capture swirling and recirculating flow behaviours, influencing particle trajectories.

The Eulerian-Lagrangian approach was employed to model gas-solid flow with two-way coupling, accounting for interactions between the continuous (gaseous) and discrete (solid biomass particles) phases. The continuous phase was modelled using a Eulerian reference frame, while the discrete phase utilised a Lagrangian approach. Particle trajectories and interactions were tracked using the discrete random walk model, and particle momentum interaction was ignored.

In the furnace, heat transfer to the walls is predominantly due to radiation from hot gases and ash particles. The discrete ordinates model was used to solve the radiative transfer equation for a finite set of discrete solid angles, providing a detailed depiction of radiative heat transfer within the boiler. The absorption coefficients of the gas mixture were computed using the weighted sum of gray gases model, considering radiation emission from CO_2 and H_2O. The interaction between ash particles and radiation, including scattering effects, was also enabled in the CFD model.

Boundary conditions were defined to accurately reflect the physical environment of the boiler. Key conditions included air and burner inlets, specifying the mass flow rate, composition, and temperature of incoming air. Fuel mass flow rate, particle size, inlet velocity, temperature, and composition were also specified. The furnace walls were modelled as planar surfaces using an effective heat transfer coefficient approach, while no-slip conditions were applied to the walls. A reflect condition for radiation and particles was specified at impermeable walls, and a standard escape boundary condition was used at the outlet.

A significant distinction between the two boilers analysed lies in the operational characteristics of the spreader air velocity. In the second case study, the boiler maintains a constant spreader air velocity across the entire load range, resulting in deeper dispersion of fuel particles into the furnace at lower loads. In contrast, the spreader air velocity for the first case study boiler decreases with load. Since the geometry of the first case study boiler is not symmetrical around the centre line, the full geometry of the boiler was included in the CFD model. In contrast to this, only half of the second case study boiler geometry was modelled to reduce the total mesh count, based on the assumption of symmetrical distribution of transport variables around the centre plane of the boiler.

5.2 CFD Model Validation

The methodology for CFD modelling of the case study boilers was validated using site data from the second case study, focusing on two load scenarios: 100 t/h and 65 t/h. Due to the challenges associated with directly measuring gas temperature at the furnace exit, the heat transfer to the furnace waterwalls cannot be precisely determined through site measurements alone. However, the total heat transfer to the steam generation cycle—which includes heat transfer to the furnace waterwalls, superheater cavity walls, and evaporator tube bank—can be determined from site measurements. This is possible because the pressure in the steam drum is known, allowing for the determination of the saturation temperature of the steam exiting the drum, as well as its enthalpy.

Given the known temperature of the water entering the steam generation cycle, denoted as Point 3 in Figure 4.3, the amount of heat absorbed by the cycle can be calculated. By comparing this absorbed heat to that predicted by the CFD model, the performance and accuracy of the model can be validated against site data.

For the 100 t/h case, heat transfer measurements were taken at ten-minute intervals over a two-hour period. The heat uptake for each interval was calculated, and from these calculations, both the mean heat uptake and the standard deviation were derived. In the 65 t/h case, measurements were taken every second over a twenty-minute period at various locations, and the heat uptake was calculated at four-minute intervals. Similarly, the mean heat uptake and standard deviation were computed for this case.

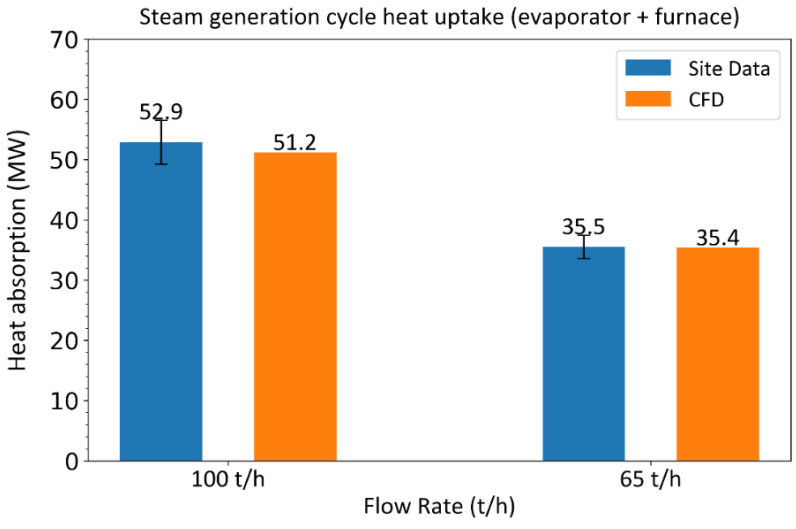

Figure 5.3: *Comparison of steam generation cycle heat uptake.*

Figure 5.3 presents a comparison of the heat uptake values derived from site data and those predicted by the CFD model for both load cases. For the 100 t/h scenario, the site measurements

indicate an average heat uptake of 52.9 MW, with a standard deviation of 3.6 MW, while the CFD model predicts a slightly lower uptake of 51.2 MW. In the 65 t/h case, the site measurements show a heat uptake of 35.5 MW, with a standard deviation of 2.0 MW, while the CFD model prediction closely matches, with a heat uptake of 35.4 MW.

These results demonstrate a good level of agreement between the CFD predictions and the site measurements. This validates the robustness of the CFD model in simulating the heat transfer dynamics of the boiler under different operating loads. Furthermore, the slight discrepancy observed in the 100 t/h case, where the CFD model underpredicts the heat uptake by approximately 1.7 MW, is within acceptable limits of uncertainty, considering the complexities involved in boiler heat transfer processes, such as varying gas temperatures, radiation, and convective heat transfer. The close alignment between the measured and modelled heat uptake values supports the reliability of the CFD methodology in capturing the essential thermodynamic behaviour of the system.

5.3 CFD Post Processing

Detailed post-processing was carried out on the CFD results to determine all the energy flows through the furnace so that it can be compared directly with those of the 0-D process model. This includes the magnitude of direct radiation through the furnace exit, which cannot be extracted directly from the CFD results and must therefore be derived by performing a furnace energy balance.

Figure 5.4 illustrates the control volume for the furnace, capturing all energy flowing into and out of the furnace, including energy absorbed by surrounding surfaces.

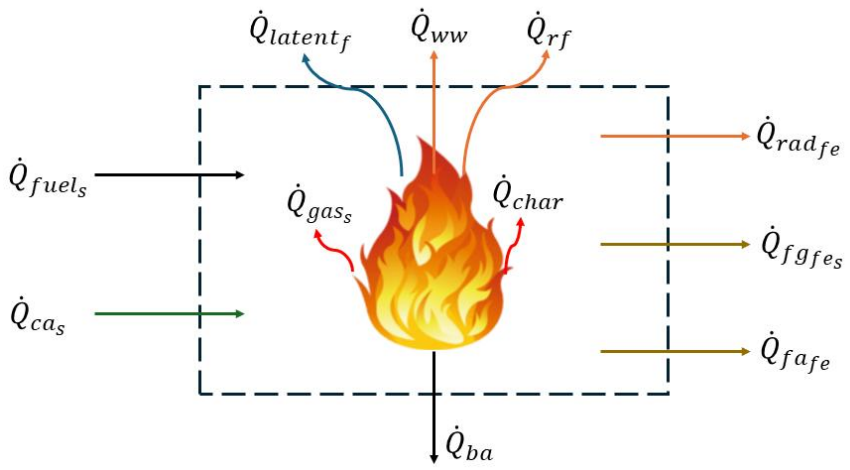

Figure 5.4: *Control volume – Furnace energy balance (sensible heat).*

Equation 5.1 translates the energy flows illustrated in the control volume into a mathematical representation, demonstrating that the energy entering the furnace must be balanced by the energy leaving it. In the equation, the left-hand side represents the energy inputs into the furnace, while the right-hand side represents the energy outputs.

$$\dot{Q}_{fuel_s} + \dot{Q}_{react_s} + \dot{Q}_{ca_s} = \dot{Q}_{fg_{fe_s}} + \dot{Q}_{ww} + \dot{Q}_{rf} + \dot{Q}_{rad_{fe}} + \dot{Q}_{fa_{fe}} + \dot{Q}_{ba} + \dot{Q}_{latent_f} \quad 5.1$$

Here, $\dot{Q}_{fuel_s}$ and $\dot{Q}_{ca_s}$ are the sensible energy inputs from the fuel and combustion air, respectively, calculated using Equation 3.32. The mass flow rate and sensible enthalpy of the combustion air are obtained directly from the CFD model results obtained via Fluent.

The total heat of reaction, $\dot{Q}_{react_s}$, comprises the heat released from volatile combustion and CO oxidation ($\dot{Q}_{gas_s}$), and the heat added from char oxidation ($\dot{Q}_{char}$). $\dot{Q}_{gas_s}$ is directly extracted from the Fluent results, while char combustion is represented by Equation 5.2.

$$C(s) + 0.5\, O_2\,(g) \rightarrow CO\,(g) \quad 5.2$$

The energy released from the combustion of char can be calculated using Equation 5.3, where DPM_{burn} represents the burn rate of discrete phase particles in the furnace, directly obtained from the Fluent results, and LCV_{char} represents the heat of reaction of the char combustion, which was set to a value of 10 100 kJ/kg [33].

$$\dot{Q}_{char} = DPM_{burn} \cdot LCV_{char} \quad 5.3$$

The overall heat of reaction is then expressed as shown in Equation 5.4.

$$\dot{Q}_{react_s} = \dot{Q}_{gas_s} + \dot{Q}_{char} = \dot{Q}_{gas_s} + DPM_{burn} \cdot LCV_{char} \quad 5.4$$

The energy outputs, $\dot{Q}_{ww}$ and $\dot{Q}_{rf}$ are directly extracted from the CFD results, while $\dot{Q}_{fg_{fe_s}}$, $\dot{Q}_{fa_{fe}}$ and $\dot{Q}_{ba}$ are calculated using equations shown in 5.5. Here, $h_{fg_{fe_s}}$, $\dot{m}_{fg_{fe}}$ and $T_{fg_{fe}}$ are properties of flue gas leaving the furnace exit, extracted from CFD simulations, and T_{gr} is the temperature of the top grate, which is assumed to be the temperature the bottom ash leaves the furnace.

$$\dot{Q}_{fg_{fe_s}} = \dot{m}_{fg_{fe}} \cdot h_{fg_{fe_s}}$$

$$\dot{Q}_{fa_{fe_s}} = \dot{m}_{fa_{fe}} \cdot c_{p_{ash}}(T_{fg_{fe}} - T_{ref}) \quad 5.5$$

$$\dot{Q}_{ba_s} = \dot{m}_{ba} \cdot c_{p_{ash}}(T_{gr} - T_{ref})$$

The total mass flow rate of ash ($\dot{m}_{ash}$) can be calculated according to Equation 5.6.

$$\dot{m}_{ash} = \left(\dot{m}_f + \dot{m}_{ca}\right) - \dot{m}_{fg_{fe}} \quad 5.6$$

From this, the mass flow rates of fly ash ($\dot{m}_{fa_{fe}}$) and bottom ash ($\dot{m}_{ba}$) are derived as shown in Equations 5.7 and 5.8. The fraction of fly ash that leaves the boiler outlet (f_{fa}) can be extracted directly from Fluent.

$$\dot{m}_{fa_{fe}} = f_{fa} \cdot \dot{m}_{ash} \quad 5.7$$

$$\dot{m}_{ba} = (1 - f_{fa}) \cdot \dot{m}_{ash} \quad 5.8$$

The endothermic reaction for moisture release from the fuel is described in Equation 5.9. In the equation, h_{latent} is the latent heat of vaporisation (2263 kJ/kg) at the furnace pressure.

$$\dot{Q}_{latent_f} = Y_{M_{AR}} \cdot h_{latent} \quad 5.9$$

To determine the radiation leaving through the furnace exit ($\dot{Q}_{rad_{fe}}$), Equation 5.1 is rearranged as shown below.

$$\dot{Q}_{rad_{fe}} = \dot{Q}_{fuel_s} + \dot{Q}_{react_s} + \dot{Q}_{ca_s} - (\dot{Q}_{fg_{fe_s}} + \dot{Q}_{ww} + \dot{Q}_{rf} + \dot{Q}_{fa_{fe}} + \dot{Q}_{ba} + \dot{Q}_{latent_f}) \quad 5.10$$

Once $\dot{Q}_{rad_{fe}}$ is calculated, the full energy balance, which includes the latent energies, can be determined. Incorporating latent energy allows for a direct comparison with the 0-D furnace models. Figure 5.5 presents the control volume of the furnace, taking these latent energies into account.

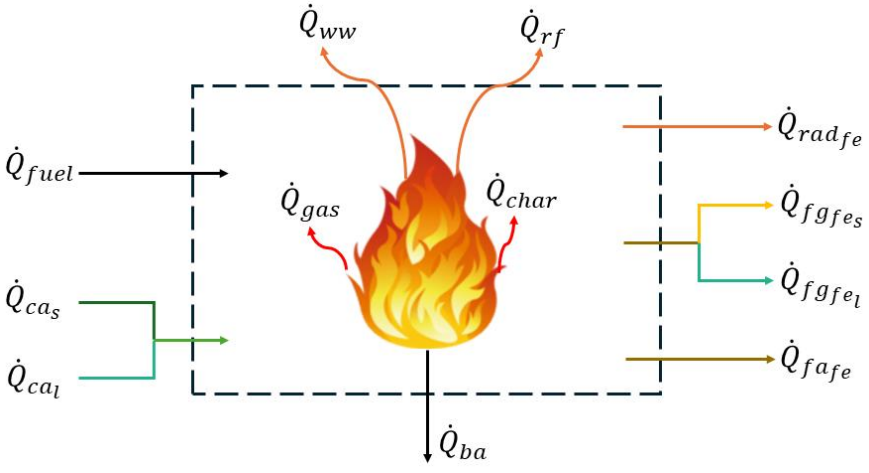

Figure 5.5: *Control volume – Furnace energy balance (sensible and latent heat).*

The total energy from combustion air, including latent energy ($\dot{Q}_{ca_l}$), is expressed as shown in Equation 5.11. Here, $Y_{H_2O_{ca}}$ represents the mass fraction of water vapour in the combustion air, derived directly from Fluent.

$$\dot{Q}_{ca} = \dot{Q}_{ca_s} + \dot{Q}_{ca_l} = \dot{Q}_{ca_s} + \dot{m}_{ca} \cdot Y_{H_2O_{ca}} \cdot h_{latent} \quad 5.11$$

Similarly, the total energy of the flue gas leaving at the furnace exit, including the latent energy ($\dot{Q}_{fg_{fe_l}}$), is calculated as shown in Equation 5.12. In the equation, $Y_{H_2O_{fg_{fe}}}$ denotes the mass fraction of water vapour in the flue gas, extracted directly from Fluent.

$$\dot{Q}_{fg_{fe}} = \dot{Q}_{fg_{fe_s}} + \dot{Q}_{fg_{fe_l}} = \dot{Q}_{fg_{fe_s}} + \dot{m}_{fg_{fe}} \cdot Y_{H_2O_{fg_{fe}}} \cdot h_{latent} \quad 5.12$$

The total heat of reaction of the fuel can be calculated using the HHV of the fuel. The maximum theoretically possible heat released ($\dot{Q}_{react}$) is calculated as shown in Equation 5.13.

$$\dot{Q}_{react} = \dot{m}_f \cdot HHV_f \quad 5.13$$

Not all fixed carbon in the char undergoes complete combustion. The amount of unburnt carbon ($\dot{Q}_{UC}$) is computed by considering the ideal burnout of discrete phase particles ($DPM_{burn_{ideal}}$), as shown in Equation 5.14. Here, $Y_{FC_{PA}}$ represents the mass fraction of fixed carbon from the proximate analysis of the fuel.

$$\dot{Q}_{UC} = \left(DPM_{burn_{ideal}} - DPM_{burn}\right) \cdot HHV_c = \left(\dot{m}_f \cdot Y_{FC_{PA}} - DPM_{burn}\right) \cdot HHV_C \quad 5.14$$

Once the latent heats have been incorporated, the revised energy balance for the CFD furnace is formulated as shown in Equation 5.15.

$$\dot{Q}_{fuel_s} + (\dot{Q}_{react} - \dot{Q}_{UC}) + \dot{Q}_{ca} = \dot{Q}_{fg_{fe}} + \dot{Q}_{ww} + \dot{Q}_{rf} + \dot{Q}_{rad_{fe}} + \dot{Q}_{fa_{fe}} + \dot{Q}_{ba} \quad 5.15$$

Post-processing facilitates a direct comparison between the CFD simulation and the python process model, enabling an in-depth evaluation of the 0-D modelling methodologies employed in the python model. This detailed approach ensures that all energy contributions and losses are meticulously accounted for.

5.4 Summary

This chapter has detailed the CFD modelling methodology and post-processing techniques for biomass-fired boilers, including the validation of the modelling methodology against site measurements. This comprehensive approach, which integrates advanced sub-models such as turbulence, combustion, and heat transfer, along with detailed boundary conditions, ensures accurate simulation and analysis of the biomass combustion processes. The validation process, comparing CFD model predictions with site measurements, further reinforces the reliability of the methodology.

The subsequent section will present the results obtained from both the 0-D and CFD models for the two case studies, offering insights into their comparative performance.

6. Results and Discussion

Comparing the results of the 0-D furnace models with that of the CFD benchmarks provides insightful observations. This section delves deeper into the nuances of these results, integrating relevant theory to contextualise and interpret the findings. The analysis focuses on four distinct model configurations derived from two methods: the projected method and the direct method. Each method is evaluated using the standard model and the high ash model, resulting in four unique sets of 0-D model predictions for each operational condition. These models are identified according to the naming convention shown in Table 6-1.

Table 6-1: *Naming conventions for variations of the 0-D models.*

Name	Description
P1	Projected method – high ash model
P2	Projected method – standard model
D1	Direct method – high ash model
D2	Direct method – standard model

To facilitate a comprehensive comparison, Section 6.1 examines the energy inputs into both the CFD and 0-D models, establishing a common basis for analysis. Subsequently, Sections 6.2 and 6.3 provide a detailed comparative analysis of the case study boilers, highlighting key differences in performance predictions. Lastly, Section 6.4 presents a sensitivity analysis to identify the key parameters influencing the accuracy and behaviour of the 0-D models, thereby providing insights into the underlying factors that affect their predictive capabilities.

6.1 Energy Input to the Furnace

To enable a one-to-one comparison between the 0-D process models and the CFD models, it is essential to ensure that both models account for the same energy entering the furnace control volume. The control volume for the furnace, illustrated in Figure 6.1, establishes the boundaries for this comparison.

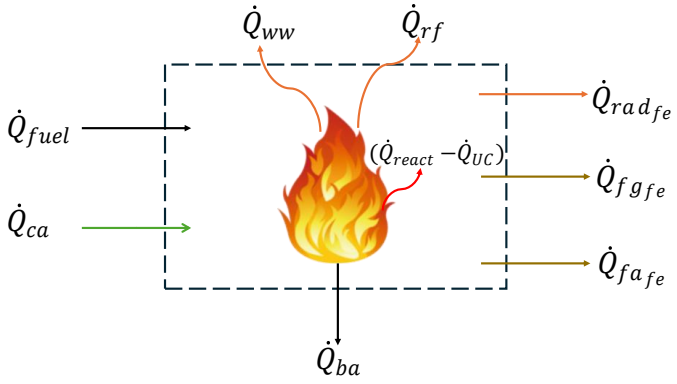

Figure 6.1: *Control volume – Furnace energy balance.*

Case Study 1 – Energy Balance

Table 6-2 presents the energy input data for the full load case (45 t/h) of the boiler in Case Study 1, demonstrating a negligible difference of 39 kW between the CFD and 0-D models. The discrepancy arises from the energy carried by the combustion air, attributable to slight differences in the calculation of fluid properties between the two models. This small difference, however, is insignificant in terms of its impact on overall energy distribution, with a relative error of less than 0.1%.

The results of the lower load cases, the 36 t/h and the 27 t/h, are similar to that of the full load case, with the relative error being less than 0.1% for both cases (Appendix D). These results demonstrate that both models are capturing identical energy inflows, allowing for a direct comparison of their predictive capabilities.

Table 6-2: *CFD vs. 0-D models (Case study 1) – Comparison of furnace energy inflow [kW].*

Description	$\dot{Q}_{ca}$	$\dot{Q}_{fuel_s}$	$\dot{Q}_{react}$	$\dot{Q}_{UC}$	Sum
CFD	4,344	13	49,569	-563	53,363
0-D	4,383	13	49,569	- 563	53,402
Relative error	*0.9%*	*0.0%*	*0.0%*	*0.0%*	*0.1%*

Case Study 2 – Energy Balance

A similar pattern is observed for the larger industrial-scale boiler in Case Study 2, as illustrated in Table 6-3. In this case, the full load operation (100 t/h) also exhibits a negligible energy input difference between the CFD and 0-D models, with a variation of 33 kW. This difference, like in Case Study 1, is primarily due to the energy carried by the combustion air and attributable to slight differences in the calculation of fluid properties between the two models. The relative error remains under 0.1%, reinforcing the consistency of the energy input across both models for various operational conditions. Furthermore, the results for the lower load cases, 80 t/h and 65 t/h, presented in Appendix D, exhibit a similarly low relative error, indicating that both models maintain the same energy input even as the operational load decreases.

Table 6-3: *CFD vs. 0-D models (Case study 2) – Comparison of furnace energy inflow [kW].*

Description	$\dot{Q}_{ca}$	$\dot{Q}_{fuel_s}$	$\dot{Q}_{react}$	$\dot{Q}_{UC}$	Sum
CFD	9,154	32	116,962	-1,462	124,685
0-D	9,187	32	116,962	-1,462	124,718
Relative error	*0.4%*	*0.0%*	*0.0%*	*0.0%*	*0.1%*

The consistency in energy inflow across different load cases, as demonstrated for both Case Study 1 and Case Study 2, indicates that the CFD and 0-D models are capturing the same energy inputs. This establishes a baseline for comparing the energy outflows and evaluating the predictive accuracy of the two models. With the models accounting for nearly identical energy inflows, the subsequent step was to analyse the energy outflows. The energy outflow analysis is presented in Section 6.2 for Case Study 1 and Section 6.3 for Case Study 2, focusing on the distribution of energy across various surfaces and flow of heat out of the furnace control volume.

6.2 Case Study 1 – Energy Distribution Analysis

In Case Study 1, three operational scenarios were analysed to evaluate the performance of the 0-D models in predicting the energy outflow and distribution under different load conditions. The loads analysed were: 45 t/h (full load, 100%), 36 t/h (80% load), and 27 t/h (60% load). For each case, the energy outflows were investigated to assess the accuracy of the 0-D models against the CFD in predicting the energy balance and to identify any discrepancies in the energy distribution to the various surfaces.

6.2.1 Full Load Performance (45 t/h)

The energy outflow results for the compact biomass-fired boiler at full load are presented in Table 6-4. The results reveal that both the CFD and the projected method account for a similar total energy outflow of approximately 54 MW, with a relative error of less than 0.4%. This close agreement underscores the reliability of the model in predicting overall energy outflow under full load conditions and ensuring an overall energy balance between the energy in- and outflows. Although the CFD model omits radiation loss ($\dot{Q}_{rad_{loss}}$), this has minimal impact on the overall result.

Table 6-4: *CFD vs. Projected method (45 t/h) – Comparison of furnace energy outflow [kW].*

Description	$\dot{Q}_{ww}$	$\dot{Q}_{rf}$	$\dot{Q}_{rad_{fe}}$	$\dot{Q}_{fg_{fe}}$	$\dot{Q}_{rad_{loss}}$	$\dot{Q}_{fa_{fe}}$	$\dot{Q}_{ba}$	**Sum**
CFD	13,867	181	1,973	37,281	-	143	108	53,553
P1 model								
P1	11,117	215	1,985	39,651	136	153	108	53,363
Relative error	*-19.8%*	*18.6%*	*0.6%*	*6.4%*	-	*6.4%*	*0.0%*	*-0.4%*
P2 model								
P2	12,312	238	2,198	38,211	150	146	108	53,363
Relative error	*-11.2%*	*31.4%*	*11.4%*	*2.5%*	-	*1.6%*	*0.0%*	*-0.4%*

Analysis of Energy Distribution

Despite the similarity in total energy outflow, notable differences arise in the distribution of energy across different surfaces. The P1 model exhibits an underprediction of waterwall heat uptake ($\dot{Q}_{ww}$) by 2.7 MW, corresponding to a relative error of 19.8%. Consequently, this underprediction leads to elevated flue gas temperatures, resulting in a higher heat flow via the flue gas leaving the furnace exit ($\dot{Q}_{fg_{fe}}$) by 2.4 MW, reflecting a relative error of 6.4%. Despite these differences, the P1 model tracks the direct radiation through the furnace exit ($\dot{Q}_{rad_{fe}}$) with good accuracy, yielding a relative error of less than 1%.

The P2 model also underpredicts $\dot{Q}_{ww}$ though to a lesser extent, with an underprediction of 1.6 MW and a relative error of 11.2%. P2 overestimates $\dot{Q}_{fg_{fe}}$ by 0.9 MW, corresponding to a relative error of 2.5%. While the P2 model demonstrates improved performance over the P1 model in these aspects, it falls short in accurately predicting $\dot{Q}_{rad_{fe}}$, exhibiting a relative error of 11.4%.

The fact that the standard model outperforms the high ash model confirms the expectation that the high ash model will not provide better accuracy, due to the inherently low ash content of the biomass fuel.

Table 6-5: *CFD vs. Direct method (45 t/h) – Comparison of furnace energy outflow [kW].*

Description	$\dot{Q}_{ww}$	$\dot{Q}_{rf}$	$\dot{Q}_{rad_{fe}}$	$\dot{Q}_{fg_{fe}}$	$\dot{Q}_{rad_{loss}}$	$\dot{Q}_{fa_{fe}}$	$\dot{Q}_{ba}$	Sum
CFD	13,867	181	1,973	37,281	-	153	108	53,553
D1 model								
D1	10,170	32	865	41,912	113	163	108	53,363
Relative error	*-26.7%*	*-82.5%*	*-56.2%*	*12.4%*	-	*13.8%*	*0.0%*	*-0.4%*
D2 model								
D2	11,522	36	957	40,456	128	156	108	53,363
Relative error	*-16.9%*	*-80.1%*	*-51.5%*	*8.5%*	-	*9.0%*	*0.0%*	*-0.4%*

The D1 and D2 models, presented in Table 6-5, reveal even larger discrepancies in their predictions. Consistent with the findings observed for the projected method, the standard model (D2) continues to demonstrate superior performance compared to the high ash model (D1). Both direct method

models significantly underestimate $\dot{Q}_{ww}$, with the D1 model showing a relative error of 26.7%, indicating a substantial disparity. This underestimation leads to corresponding overestimations of $\dot{Q}_{fg_{fe}}$, although the error for this metric is less pronounced, reaching 12.4% for the D1 model.

Moreover, the direct method models reveal notable limitations in accurately predicting $\dot{Q}_{rad_{fe}}$, with errors reaching up to 56%. In contrast, the projected method models demonstrated better accuracy in predicting $\dot{Q}_{rad_{fe}}$ due to their more sophisticated treatment of radiative heat transfer, which takes into account the actual position of the flame core.

The direct method models also considerably underestimate the heat absorbed by the refractory ($\dot{Q}_{rf}$), with a relative error of up to 83%. These shortcomings further illustrate the challenges associated with the direct method models.

In comparison, the projected method models consistently outperform the direct method models, with the P2 model standing out as the most reliable option in terms of overall predictive capability.

Analysis of Predicted Flue Gas and Wall Temperatures

Figure 6.2 shows the volume-averaged temperature profile of the flue gas along the furnace height. In the CFD model, the volume-averaged flue gas temperature is 1257 K, while the mass-averaged FEGT is lower, at 1188 K.

The figure reveals that the high-temperature zone is concentrated in the lower portion of the furnace, with the peak temperature occurring at 1.5 m along the furnace height, corresponding to the location of the refractory lining (positioned between 1.1 m and 3.5 m). The relative height of the highest temperature zone within the furnace is 0.13 m.

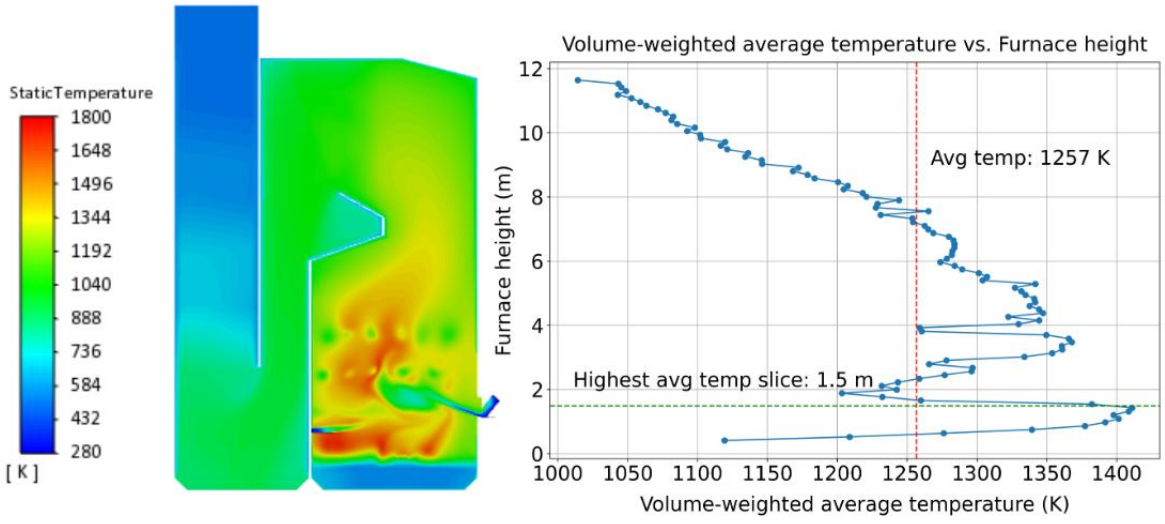

Figure 6.2: *Case study 1 (45 t/h) – CFD furnace temperature profile.*

Table 6-6 provides a comparative analysis of temperatures obtained using the 0-D methods against the CFD model. Although the 0-D methods underpredict $\dot{Q}_{ww}$, which would typically suggest lower average gas temperatures (T_{fg}) than the CFD, the results in Table 6-6 indicate otherwise. Specifically, the 0-D models predict higher T_{fg} values than those observed in the CFD model.

Table 6-6: *CFD vs. 0-D models (45 t/h) – Comparison of furnace temperatures [K].*

Description	$T_{fg_{fe}}$	Error	T_{fg}	Error	T_{ww}	Error	T_{rf}	Error	T_w	Error
CFD	1,188	-	1,257	-	735	-	1,287	-	817	-
P1	1,245	*4.8%*	1,411	*12.2%*	-	-	-	-	-	-
P2	1,202	*1.2%*	1,366	*8.7%*	-	-	-	-	-	-
D1	1,311	*10.4%*	1,311	*4.3%*	688	*-6.4%*	688	*-46.6%*	688	*-15.8%*
D2	1,269	*6.8%*	1,269	*0.9%*	705	*-4.1%*	705	*-45.2%*	705	*-13.7%*

The 0-D methods tend to overpredict the FEGT ($T_{fg_{fe}}$). This outcome is consistent with the expected trend: a reduced waterwall heat uptake leads to higher flue gas temperatures at the furnace exit and consequently increases the heat flow carried by the flue gas through the furnace exit. This pattern is evident in the D1 and D2 models, where the reduced heat transfer for $\dot{Q}_{ww}$ leads to high $T_{fg_{fe}}$ values. In contrast, the P1 and P2 models show better performance in predicting $T_{fg_{fe}}$, which aligns with their more accurate predictions of the flue gas heat flow $\dot{Q}_{fg_{fe}}$. Notably, the P2 model shows close agreement with the CFD predictions, with a relative error of only 1.2%, a reflection of its more accurate $\dot{Q}_{fg_{fe}}$ prediction. Additionally, the projected method models predict a higher $\dot{Q}_{rad_{fe}}$ compared to the CFD model, which aligns with the observed higher $T_{fg_{fe}}$.

In contrast, although the direct method models also predicts a $T_{fg_{fe}}$ higher than the CFD, which would intuitively suggest an increase in $\dot{Q}_{rad_{fe}}$, it predicts less than half of the radiation predicted by the CFD model. This highlights a significant limitation in the ability of the direct method to accurately model the direct radiation through the furnace exit.

Furthermore, as shown in Table 6-6, the direct method models predict a higher $T_{fg_{fe}}$ and a lower wall temperature (T_w) compared to the CFD model. This observation could intuitively suggest that the models would predict a correspondingly higher $\dot{Q}_{ww}$. However, as shown in Table 6-5, this is not

the case. This finding suggests that there may be limitations in the modelling of gas-particle and wall interactions within the context of this boiler system. Moreover, the direct method assumes a constant T_w, while in reality there is a variation in wall temperature, as indicated in Figure 6.3. models, further emphasising the limitations of its modelling approach.

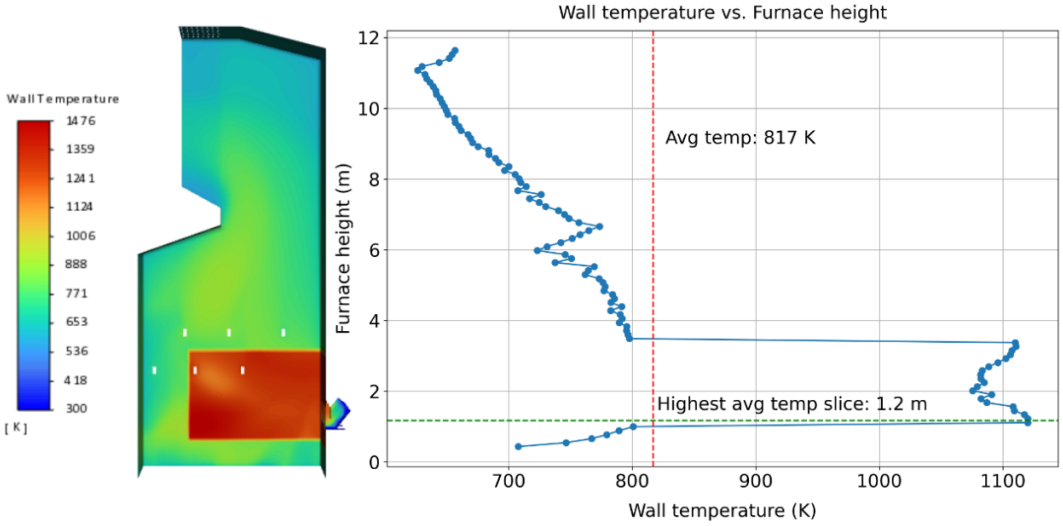

Figure 6.3: *Case study 1 (45 t/h) – CFD wall temperature profile along furnace height.*

This oversimplification likely contributes to inaccuracies in the predictions by the direct method models. Additionally, the direct method further simplifies the thermal analysis by assuming that the temperatures of the waterwall (T_{ww}) and the refractory (T_{rf}) are equal to T_w. This assumption is made due to the complexity in explicitly determining the individual temperatures of these surfaces. While this approximation may be reasonable for T_{ww}, it significantly misrepresents T_{rf}, which is significantly higher as shown in Table 6-6. This inaccuracy could contribute to the low $\dot{Q}_{rf}$ observed in the direct method.

6.2.2 Reduced Load Performance (36 t/h and 27 t/h)

The reduced load cases offer additional insights into the performance of the 0-D models under varying operational conditions. As the load decreases, the total fuel input and heat generation decrease, altering the heat transfer dynamics within the furnace. In the reduced load cases, the primary air, secondary air, and spreader air velocities were reduced proportionally, maintaining the same velocity profile while adjusting the total air mass flow rate to match the reduced fuel input. The primary air, being fed from the bottom of the furnace, drives the updraft, and thus, a reduction in primary air velocity leads to a lower updraft, affecting the overall combustion dynamics within the furnace.

Impact of Load Reduction on Combustion Dynamics

As shown in Figure 6.4, the velocity profile remains roughly the same between the load cases, even as the total mass flow rate of air decreases. The similar velocity profiles suggest that the basic flow patterns, including the turbulent mixing of air and fuel, are preserved across the load variations.

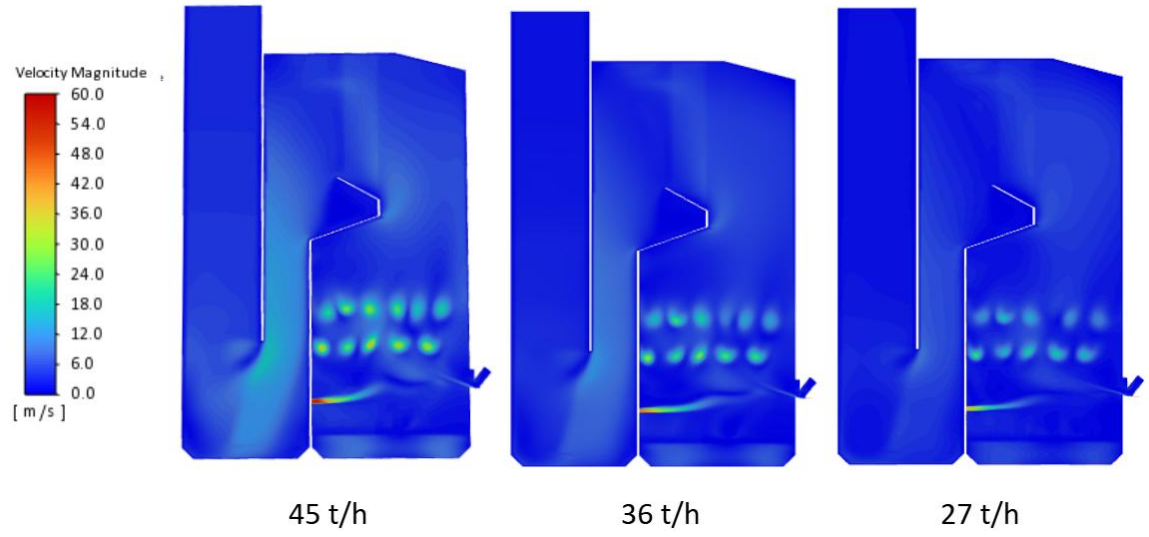

Figure 6.4: *Case study 1 – CFD velocity profiles for full and reduced loads.*

The temperature profile within the furnace is another critical indicator of how load reductions affect boiler performance. The temperature profile remains largely the same across the different load cases, with the primary combustion zone and the hottest region remaining in the horizontal centre of the furnace, as shown in Figure 6.5. Further, the temperatures at the furnace exit decrease as the load is reduced. This trend can be attributed to the combined effect of the reduced fuel input and lower air velocities, which lower the overall combustion intensity and heat release.

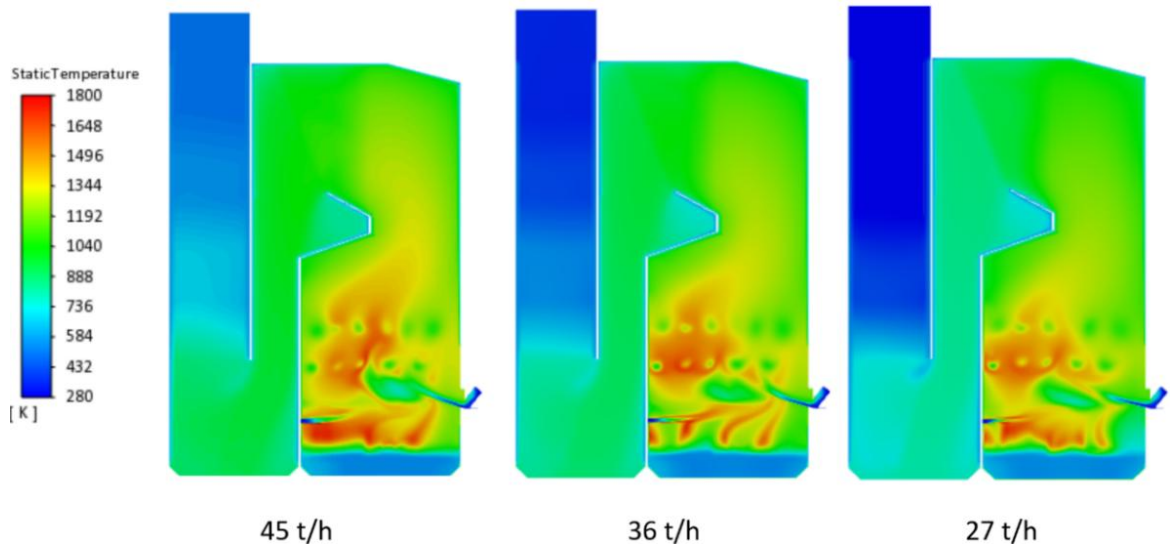

Figure 6.5: *Case study 1 – CFD temperature profiles for full and reduced loads.*

The heat flux profile, like the temperature profile, exhibits similar patterns across the different load conditions, as shown in Figure 6.6. The highest heat absorption is observed near the horizontal centre of the furnace, where the flame is most intense. As the load decreases, however, there is a clear reduction in the total heat absorbed as the combustion gases move toward the furnace exit.

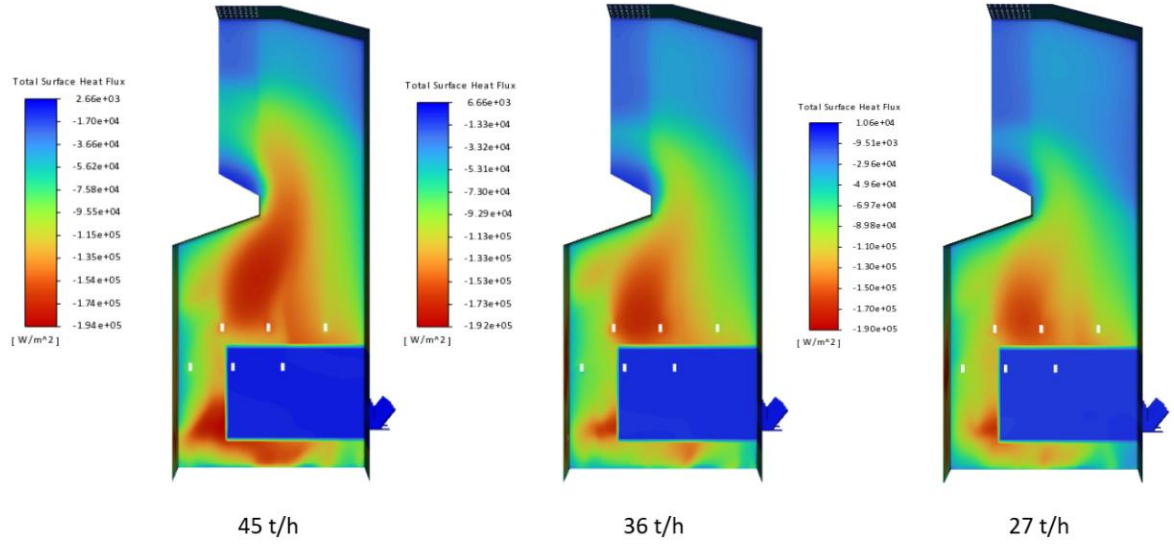

Figure 6.6: *Case study 1 – CFD total surface heat flux profile for full and reduced loads.*

This reduction in heat absorption at higher regions of the furnace can be attributed to the lower gas temperatures and reduced radiative heat transfer at partial loads. Since radiation plays a dominant role in transferring heat from the flame to the furnace walls, the lower radiative intensity at reduced loads results in lower overall heat flux to the waterwalls. Additionally, at lower loads, the combustion process is spread over a relatively larger surface area, which means relatively more heat is absorbed in the lower part of the furnace, despite the lower heat flux. This is also reflected in the decreased heat flux observed at the furnace exit.

Analysis of Energy Distribution at 36 t/h

With the trends for the reduced load cases established, the performance of the 0-D models was compared against the CFD results for the reduced load cases. The results for the 36 t/h load case, presented in Table 6-7, indicate that although the models account for a similar total energy output of approximately 42.7 MW, there are significant deviations from the CFD benchmarks, mirroring the discrepancies noted in the full load cases.

The results reveal that the accuracy of the 0-D models deteriorates with decreasing load conditions. For example, the prediction of $\dot{Q}_{ww}$ demonstrates substantial discrepancies across all models, with the D1 model reflecting a relative error of 27.3%. This result underscores the limitations of the D1 model under reduced load conditions, as it fails to capture the nuances of thermal dynamics at

reduced loads adequately. In contrast, the P1 and P2 models exhibit better performance, particularly in predicting $\dot{Q}_{fg_{fe}}$, where relative errors remain below 10%. Notably, the P2 model consistently outperforms the P1 model, affirming its superior predictive capabilities even in lower load scenarios.

Table 6-7: *CFD vs. 0-D models (36 t/h) – Comparison of furnace energy outflow [kW].*

Description	$\dot{Q}_{ww}$	$\dot{Q}_{rf}$	$\dot{Q}_{rad_{fe}}$	$\dot{Q}_{fg_{fe}}$	$\dot{Q}_{rad_{loss}}$	$\dot{Q}_{fa_{fe}}$	$\dot{Q}_{ba}$	Sum
CFD	12,519	177	1,585	28,221	0	99	95	42,706
P1 model								
P1	9,841	190	1,757	30,594	120	108	95	42,696
Relative error	*-21.4%*	*7.4%*	*10.9%*	*8.4%*	-	*9.0%*	*0.0%*	*0.0%*
P2 model								
P2	10,847	209	1,937	29,382	133	102	95	42,696
Relative error	*-13.4%*	*18.4%*	*22.2%*	*4.1%*	-	*3.5%*	*0.0%*	*0.0%*
D1 model								
D1	9,098	28	742	32,525	101	116	95	42,696
Relative error	*-27.3%*	*-84.0%*	*-53.2%*	*15.3%*	-	*17.6%*	*0.0%*	*0.0%*
D2 model								
D2	10,213	32	804	31,338	113	111	95	42,696
Relative error	*-18.4%*	*-82.0%*	*-49.3%*	*11.0%*	-	*12.3%*	*0.0%*	*0.0%*

A critical observation involves the prediction of $\dot{Q}_{rad_{fe}}$ by the P1 model, which, although initially showing good agreement with the CFD data at full load, reveals a significant relative error of 10.9% at reduced load. This sharp increase highlights the inadequacies of 0-D models in representing complex thermal dynamics within the furnace. As illustrated in Figure 6.6, the CFD results indicate a pronounced decrease in total surface heat flux near the furnace exit, which suggests a pronounced decrease in direct radiation, a phenomenon that the 0-D models fail to accurately represent. This misrepresentation further emphasises the inherent limitations of direct method models in predicting both $\dot{Q}_{rf}$ and $\dot{Q}_{rad_{fe}}$.

Analysis of Energy Distribution at 27 t/h

The performance trends observed in the 36 t/h case are reiterated in the analysis of the 27 t/h load case, as presented in Table 6-8. The prediction errors for this lower load case signify a growing trend of inaccuracy in the 0-D models, indicating an increasing challenge in tracking thermal dynamics as load decreases. This decline in model accuracy may be attributed to reduced flue gas velocity, which transitions heat transfer mechanisms toward a more radiant-dominant regime. The inability of the 0-D models to effectively model this transition likely contributes to their underperformance in lower load scenarios.

Table 6-8: *CFD vs. 0-D models (27 t/h) – Comparison of furnace energy outflow [kW].*

Description	$\dot{Q}_{ww}$	$\dot{Q}_{rf}$	$\dot{Q}_{rad_{fe}}$	$\dot{Q}_{fg_{fe}}$	$\dot{Q}_{rad_{loss}}$	$\dot{Q}_{fa_{fe}}$	$\dot{Q}_{ba}$	Sum
CFD	10,952	168	911	20,180	0	50	68	32,329
P1 model								
P1	8,333	161	1,488	21,913	102	55	68	32,119
Relative error	*-23.9%*	*-4.3%*	*63.3%*	*8.6%*	-	*9.5%*	*0.0%*	*-0.6%*
P2 model								
P2	9,118	176	1,628	20,967	111	52	68	32,119
Relative error	*-16.8%*	*4.7%*	*78.7%*	*3.9%*	-	*3.4%*	*0.0%*	*-0.6%*
D1 model								
D1	7,756	24	591	23,534	85	60	68	32,119
Relative error	*-29.2%*	*-85.6%*	*-35.1%*	*16.6%*	-	*19.9%*	*0.0%*	*-0.6%*
D2 model								
D2	8,604	27	620	22,649	94	57	68	32,119
Relative error	*-21.4%*	*-84.0%*	*-31.9%*	*12.2%*	-	*14.3%*	*0.0%*	*-0.6%*

Analysis of Predicted Flue Gas and Wall Temperatures

To enhance the understanding of thermal dynamics, a finer analysis of the temperature details was conducted. As illustrated in Figure 6.7, the volume-averaged temperature decreases with load reduction. The discretised volume-averaged temperature profile for the furnace remains relatively the same, with the highest temperature zone consistently located in the region of the refractory. The relative heights of the highest temperature zone are 0.28 m for the 36 t/h case and 0.26 m for the 27 t/h case, indicating an upward shift of the flame compared to the full load case, which has a relative height of 0.13 m. This shift may explain why the P1 model exhibits limitations in predicting $\dot{Q}_{rad_{fe}}$ at lower loads, as the altered flame position affects radiation dynamics within the furnace.

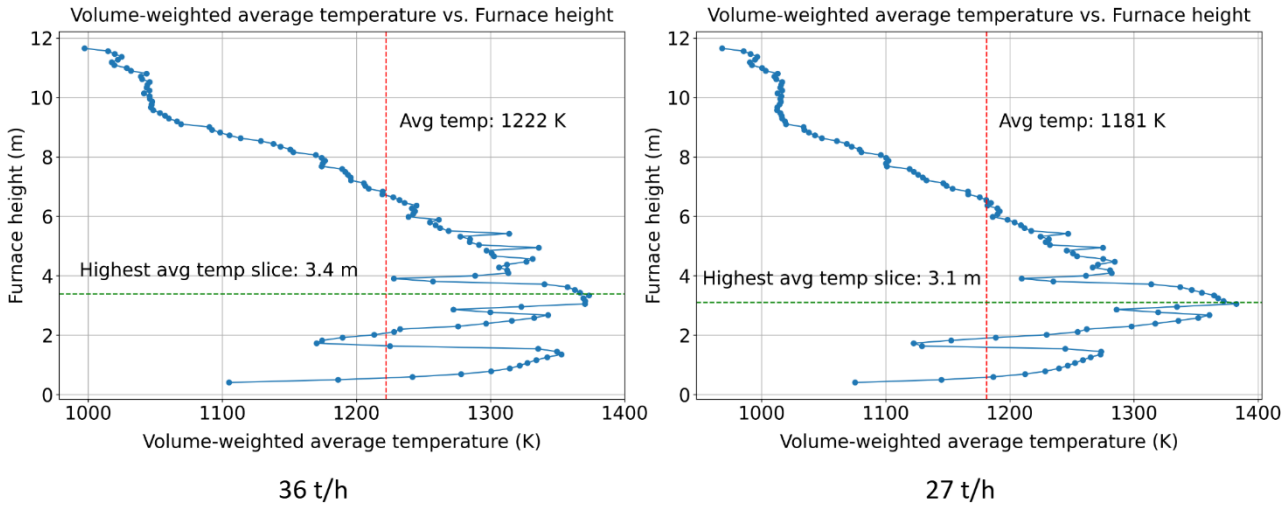

Figure 6.7: *Discretised furnace temperature profile – 36 t/h load (left) and 27 t/h load (right).*

This temperature profile is consistent with earlier findings that 0-D models tend to predict higher FEGT compared to the CFD model, as summarised in Table 6-9. The P2 model, in particular, tracks $T_{fg_{fe}}$ with a maximum relative error below 2.6% across various load conditions. Conversely, the direct method models consistently overestimate T_{fg} and underestimate T_w, without a corresponding increase in $\dot{Q}_{ww}$. This discrepancy reveals fundamental limitations within the 0-D models, particularly concerning their thermal radiation models for gas-solid suspension.

The widening performance gap between the 0-D models and the CFD results becomes increasingly pronounced as the load decreases. The D1 model consistently exhibits significant deviations from the CFD benchmarks, reinforcing the notion that 0-D models are inherently limited in their capacity to accurately capture load-dependent thermal dynamics.

Table 6-9: *CFD vs. 0-D models (36 t/h & 27 t/h) – Comparison of furnace temperatures [K].*

Description		$T_{fg_{fe}}$	***Error***	T_{fg}	***Error***	T_{ww}	***Error***	T_{rf}	***Error***	T_w	***Error***
36 t/h	CFD	1,126	-	1,222	-	717	-	1,270	-	800	-
	P1	1,201	*6.6%*	1,365	*11.7%*	-	-	-	-	-	-
	P2	1,156	*2.6%*	1,321	*8.1%*	-	-	-	-	-	-
	D1	1,272	*12.9%*	1,272	*4.1%*	674	*-6.1%*	674	*-46.9%*	674	*-15.7%*
	D2	1,229	*9.1%*	1,229	*0.5%*	688	*-4.1%*	688	*-45.8%*	688	*-14.0%*
27 t/h load											
27 t/h	CFD	1,068	-	1,181	-	698	-	1,235	-	778	-
	P1	1,142	*6.9%*	1,306	*10.6%*	-	-	-	-	-	-
	P2	1,094	*2.5%*	1,263	*6.9%*	-	-	-	-	-	-
	D1	1,222	*14.4%*	1,222	*3.5%*	657	*-5.8%*	657	*-46.8%*	657	*-15.5%*
	D2	1,178	*10.3%*	1,178	*-0.2%*	668	*-4.3%*	668	*-46.0%*	668	*-14.1%*

The performance gap between the 0-D models and CFD widens as the load decreases, with the D1 model consistently showing greater deviations from the CFD benchmark, showing that the 0-D models exhibit limitations in tracking load-dependent changes.

Summary

In conclusion, while the projected method models demonstrate better performance in predicting heat distribution and furnace exit temperatures compared to the direct method models, both show increasing discrepancies from the CFD results at lower loads, as shown in Figure 6.8, Figure 6.9 and Figure 6.10. This highlights the inherent challenges of modelling complex heat transfer processes under reduced load conditions. Additionally, the standard method outperforms the high ash method for this specific application, suggesting that although the high-ash approach is more fundamental, it does not lead to better accuracy in the case of very low ash fuels like biomass.

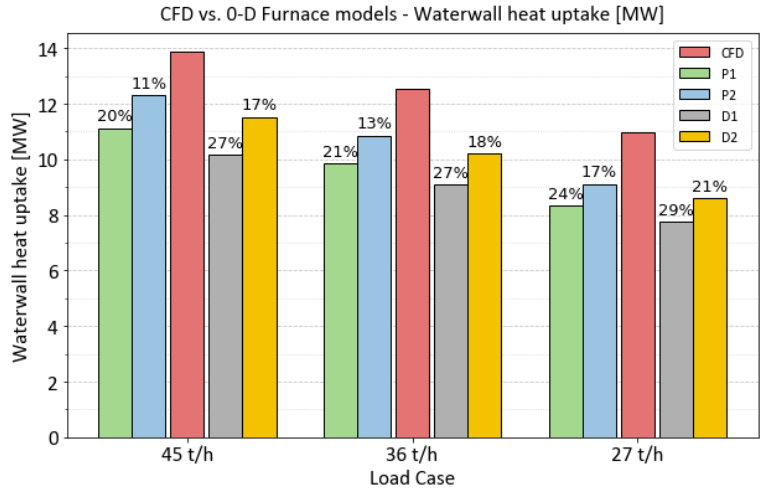

Figure 6.8: *Case study 1 - Waterwall heat uptake across all load conditions.*

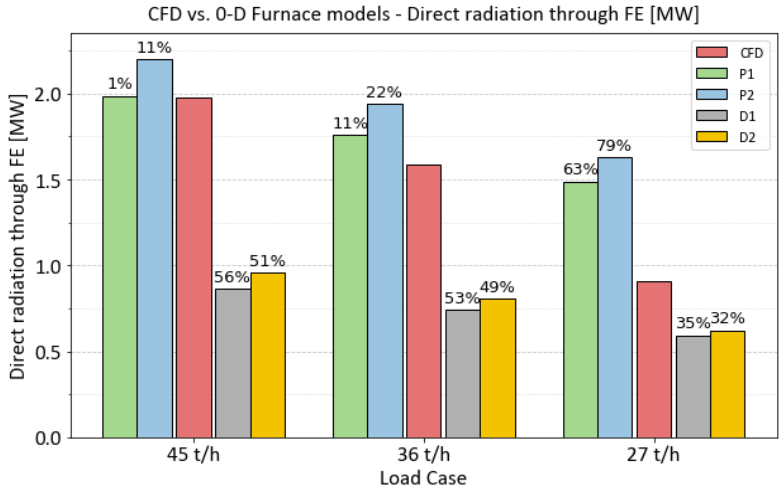

Figure 6.9: *Case study 1 - Direct radiation through the furnace exit across all load conditions.*

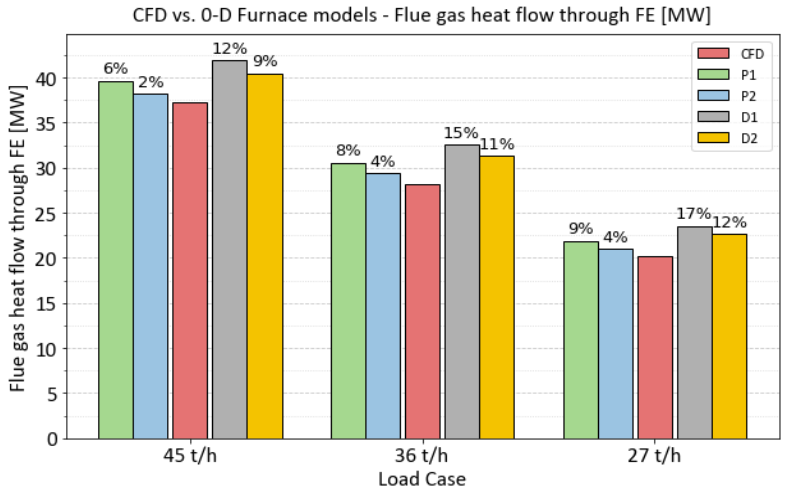

Figure 6.10: *Case study 1 - Flow of heat through the furnace exit across all load conditions.*

6.3 Case Study 2 – Energy Distribution Analysis

Building upon the findings from the compact biomass-fired boiler in the previous section, this case study investigates the performance of the models for the larger industrial biomass-fired boiler under three distinct operational conditions: full load at 100 t/h, 80 t/h, and 65 t/h. By examining how energy outflow, heat distribution, and temperature profiles evolve under these varied loads, we can draw direct comparisons to the smaller boiler to assess scalability and identify consistent trends or deviations. This comparative approach enables a deeper understanding of how boiler size, combustion dynamics, and load changes influence overall system behaviour, thus providing a more comprehensive perspective on the accuracy and applicability of 0-D models across different boiler configurations.

6.3.1 Full Load Performance (100 t/h)

Analysis of Energy Distribution

The results of the industrial biomass-fired boiler, presented in Table 6-10, offer significant insights into the performance of 0-D models for larger-scale boiler. The energy distribution analysis shows that the projected method models and the CFD simulation align closely, with both accounting for an energy outflow of approximately 125 MW and a relative error of less than 0.1%. This demonstrates a strong overall energy balance agreement between the models, which is consistent with findings from the smaller boiler in Case Study 1. However, the detailed distribution of this energy between various surfaces shows notable differences.

The projected method models reveal variations in heat absorbed by the waterwalls ($\dot{Q}_{ww}$), refractory ($\dot{Q}_{rf}$), and furnace exit heat flow ($\dot{Q}_{fg_{fe}}$). The P1 model overpredicts the $\dot{Q}_{ww}$, where the error reaches 1.7 MW, equivalent to a relative error of 6.1%, compared to the CFD model. This overprediction of $\dot{Q}_{ww}$ results in a lower predicted flue gas temperature, leading to an underestimation of $\dot{Q}_{fg_{fe}}$ by 0.6 MW, which translates to a smaller relative error of 0.6%. However, in contrast to Case Study 1, where the P1 model accurately captured direct radiation ($\dot{Q}_{rad_{fe}}$) in full-load operation, Case Study 2 reveals a significant deviation, with a relative error of 22.5%.

In contrast, the P2 model exhibits larger deviations compared to the P1 model. It overestimates $\dot{Q}_{ww}$ by 13.0%, which also impacts the prediction of $\dot{Q}_{fg_{fe}}$, leading to an underestimation of 2.7 MW, corresponding to a relative error of 3%. Additionally, comparing the high ash and standard models demonstrates different performance outcomes depending on boiler size. The high ash

model performs better in larger boilers, while the standard model yields more accurate results for smaller boilers. These results highlight the difficulties of applying thermal radiation models to boilers of varying sizes, as the complexities introduced by scaling differ significantly from those encountered in smaller boilers.

Table 6-10: *CFD vs. Projected method (100 t/h) – Comparison of furnace energy outflow [kW].*

Description	$\dot{Q}_{ww}$	$\dot{Q}_{rf}$	$\dot{Q}_{rad_{fe}}$	$\dot{Q}_{fg_{fe}}$	$\dot{Q}_{rad_{loss}}$	$\dot{Q}_{fa_{fe}}$	$\dot{Q}_{ba}$	Sum
CFD	27,819	204	5,423	90,463	-	590	84	124,583
P1 model								
P1	29,521	264	4,203	89,905	176	566	84	124,718
Relative error	*6.1%*	*29.2%*	*-22.5%*	*-0.6%*	-	*-4.2%*	*0.0%*	*0.1%*
P2 model								
P2	31,423	281	4,473	87,722	187	548	84	124,718
Relative error	*13.0%*	*37.5%*	*-17.5%*	*-3.0%*	-	*-7.2%*	*0.0%*	*0.1%*

The direct method models (Table 6-11), much like the projected methods, display varying levels of accuracy in predicting heat absorption parameters. The D1 and D2 methods predict $\dot{Q}_{ww}$ with relative errors of 5.1% and 3.0%, respectively, showing relatively good agreement with the CFD model. Similarly, the direct method models align well with the CFD in predicting $\dot{Q}_{fg_{fe}}$, with relative errors of 5.5% for D1 and 2.9% for D2. Interestingly, in the case of the direct method models, the standard model performs better than the high ash model. However, both methods exhibit significant underprediction for $\dot{Q}_{rf}$, with errors exceeding 80%, and for $\dot{Q}_{rad_{fe}}$, with errors greater than 60%. This indicates that while direct method models can reasonably predict certain heat transfer parameters, they still fall short in capturing some of the radiative processes accurately, a trend also observed with the smaller boiler. These discrepancies may arise from the simplifications employed in the application of the direct method.

Table 6-11: *CFD vs. Direct method (100 t/h) – Comparison of furnace energy outflow [kW].*

Description	$\dot{Q}_{ww}$	$\dot{Q}_{rf}$	$\dot{Q}_{rad_{fe}}$	$\dot{Q}_{fg_{fe}}$	$\dot{Q}_{rad_{loss}}$	$\dot{Q}_{fa_{fe}}$	$\dot{Q}_{ba}$	Sum
CFD	27,819	204	5,423	90,463		590	84	124,583
D1 model								
D1	26,403	38	1,967	95,470	147	610	84	124,718
Relative error	*-5.1%*	*-81.6%*	*-63.7%*	*5.5%*	-	*3.3%*	*0.0%*	*0.1%*
D2 model								
D2	28,654	41	2,102	93,087	159	591	84	124,718
Relative error	*3.0%*	*-80.1%*	*-61.2%*	*2.9%*	-	*0.1%*	*0.0%*	*0.1%*

Comparison with Case Study 1

The performance of the 0-D models in the larger boiler provides useful insights when compared to the compact boiler in Case Study 1. Although both case studies use similar modelling approaches, the results differ significantly due to the scale of the boilers. In the compact boiler, the projected method models notably underpredicted $\dot{Q}_{ww}$, with the P2 model performing better than the P1 model (Figure 6.11). This underprediction was even more pronounced in the direct method models, highlighting their limitations in smaller-scale applications.

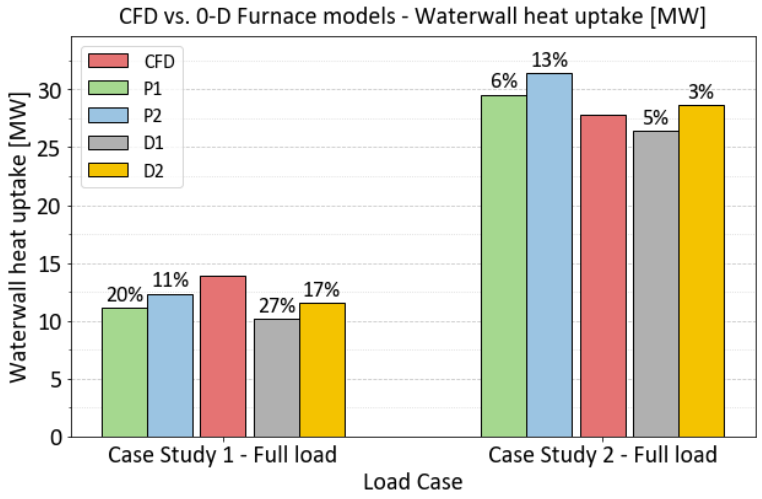

Figure 6.11: *Case study 1 vs. Case study 2 - Waterwall heat uptake (full load).*

In contrast, for the larger industrial boiler, the projected method models overestimated $\dot{Q}_{ww}$, with the P1 model showing better agreement with the CFD than the P2 model (Figure 6.11). Similarly, the direct method models demonstrated better accuracy in the larger boiler, with the D2 model outperforming the D1 model. This suggests that scaling introduces complexities in radiative heat transfer that the 0-D models do not fully capture, particularly in smaller boilers where the simplified treatment of radiation leads to reduced predictive accuracy.

For Case Study 1, the P2 model showed the best agreement with the CFD for $\dot{Q}_{fg_{fe}}$, whereas in the larger boiler, the P1 model aligned more closely with the CFD, while the P2 and D2 models also showed good agreement (Figure 6.12). This improvement in performance for the larger boiler further emphasising that 0-D models are more effective in predicting performance for larger boilers.

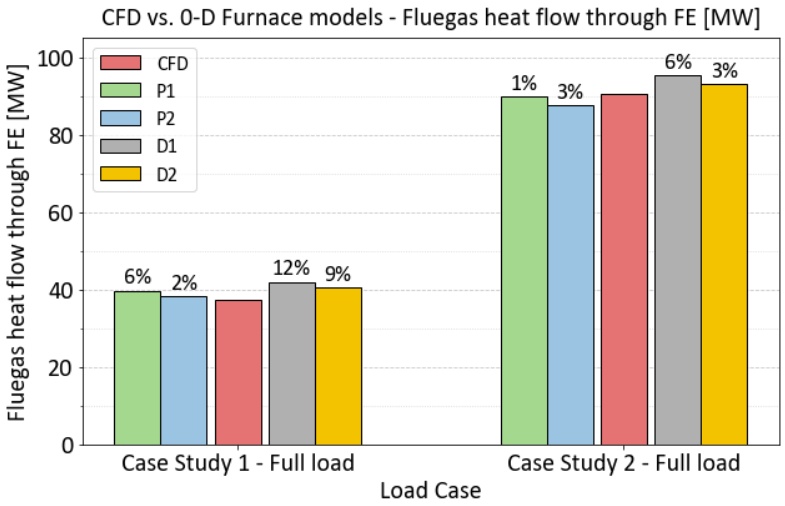

Figure 6.12: *Case study 1 vs. Case study 2 - Flow of heat through FE (full load).*

The overall improvement in model accuracy for the larger boiler indicates that, while the 0-D methods are promising for predicting certain aspects of heat transfer, their reliability depends on the operating conditions and scale of the boiler. The improved radiation predictions in the larger boiler may be attributed to the fact that the high-temperature zones and radiative heat transfer processes in larger-scale boilers more closely resemble the conditions for which these models were originally developed. Consequently, the 0-D models demonstrate better performance in larger boilers, whereas their predictive capabilities are more limited in smaller systems.

Analysis of Predicted Flue Gas and Wall Temperatures

In addition to the energy distribution, the analysis of the flue gas temperature profiles provides further insights (Figure 6.13).

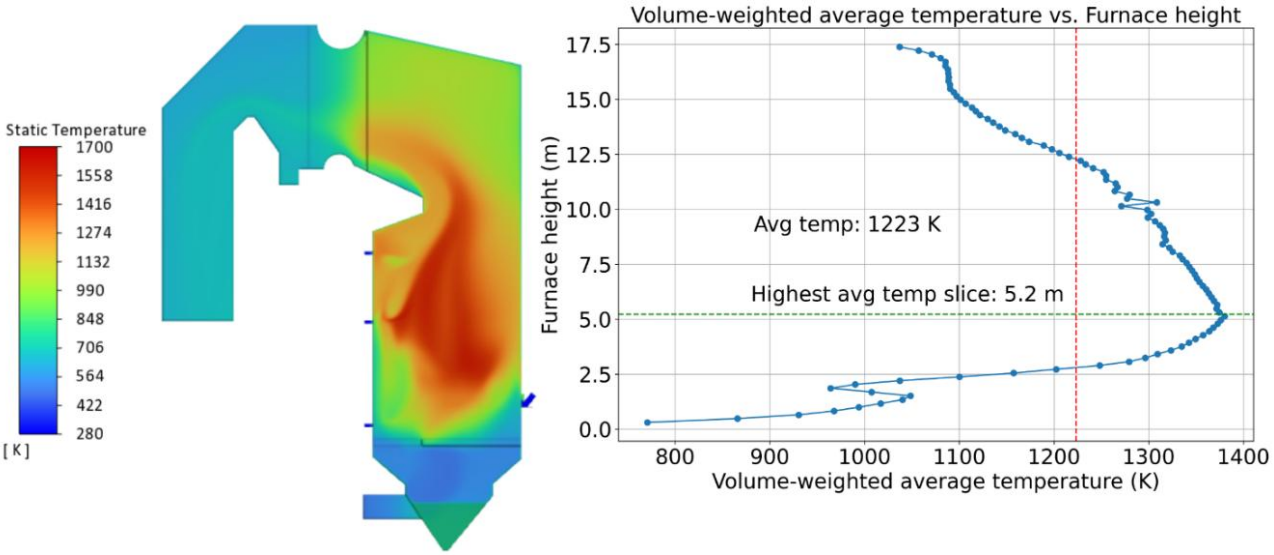

Figure 6.13: *Case study 2 (100 t/h) – CFD furnace temperature profile.*

The relative height of the highest temperature zone within the furnace is 0.30 m. The volume-averaged flue gas temperature in the CFD model is 1223 K while the mass-averaged gas temperature at the exit is higher at 1228 K. This is counter-intuitive since one would expect the outlet temperature to be lower than the average temperature. However, the reason for this is that the volume-averaged temperature also includes the large 'passive' zones of colder gas that are indicated by the green areas in Figure 6.13.

The temperature data for the 0-D models is compared to the CFD results in Table 6-12, where notable differences are observed. For the P1 model the average gas temperature is 1351 K while the FEGT is lower at 1189 K. Although this intuitively seems to be more correct, it highlights a limitation of the 0-D models where the 3-D details are omitted, since the 0-D models cannot account for the large 'passive' volumes of colder gas. This suggests that the 0-D projected method effectively captures the temperature trends in boilers with relatively uniform profiles, such as the compact boiler, but encounters difficulties when applied to boilers with more variable temperature profiles, as seen in the industrial boiler.

Interestingly, the D1 and D2 models predict FEGT values closer to that of the CFD model, with relative errors of less than 2.5%. Additionally, the direct method models demonstrate good agreement with the CFD for waterwall heat uptake, exhibiting the improved performance of the direct method in the larger boiler.

Table 6-12: *CFD vs. 0-D models (100 t/h) – Comparison of furnace temperatures [K].*

Description	$T_{fg_{fe}}$	Error	T_{fg}	Error	T_{ww}	Error	T_{rf}	Error	T_{w}	Error
CFD	1,228	-	1,223	-	641	-	1,065	-	673	-
P1	1,189	*-3.2%*	1,351	*10.5%*	-	-	-	-	-	-
P2	1,162	*-5.4%*	1,323	*8.2%*	-	-	-	-	-	-
D1	1,259	*2.5%*	1,259	*2.9%*	627	*-2.2%*	627	*-41.1%*	627	*-6.8%*
D2	1,229	*0.1%*	1,229	*0.5%*	637	*-0.6%*	637	*-40.2%*	637	*-5.3%*

Summary

The results show that the direct method models demonstrate good agreement with the CFD for predicting waterwall heat absorption ($\dot{Q}_{ww}$) and flue gas furnace exit heat flow ($\dot{Q}_{fg_{fe}}$), with relative errors under 6%. However, both models significantly underpredict refractory heat absorption ($\dot{Q}_{rf}$) and direct radiation through the furnace exit ($\dot{Q}_{rad_{fe}}$), with errors exceeding 60%. Comparisons between the two case studies reveal that the 0-D models perform better for larger boilers, with the P1 and D2 models showing the closest agreement with the CFD. These findings highlight that boiler size influences the predictive accuracy of thermal radiation models, with better results achieved in larger boilers.

The next section will examine the performance of the 0-D models in predicting performance at reduced load for the larger case study boiler.

6.3.2 Reduced Load Performance (80 t/h and 65 t/h)

Impact of Load Reduction on Combustion Dynamics

The analysis of the reduced load scenarios, shown in Figure 6.14 and Figure 6.15, highlights key changes in the velocity and temperature profiles within the furnace.

As the load decreases from 100 t/h, both the mass flow rate of primary air and secondary air decrease proportionally, which in turn reduces the upward velocity within the furnace. However, the velocity of the spreader air remains constant, significantly altering the combustion dynamics. This leads to a change in the turbulent mixing patterns and results in the combustion occurring closer to the rear wall of the furnace for the lower load cases.

The shift in combustion location has a direct impact on the heat absorption and surface heat flux distribution across the furnace walls. As shown in Figure 6.16, the highest heat absorption regions move towards the rear of the furnace under reduced loads, reflecting the changed combustion dynamics. This highlights how load reduction redistributes the thermal energy within the furnace and alters the overall heat transfer profile.

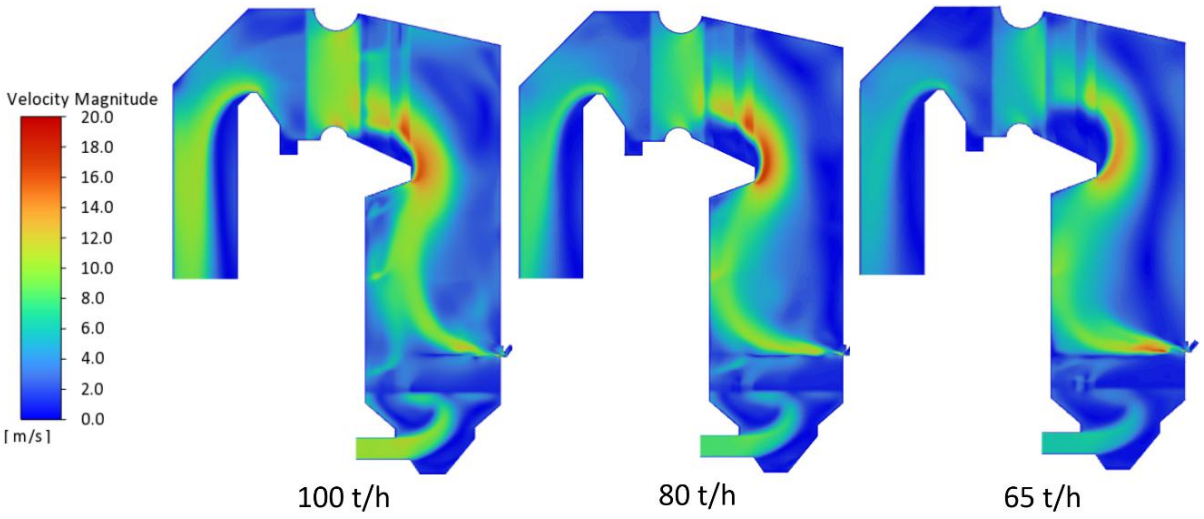

Figure 6.14: *Case study 2 – CFD velocity profiles for full and reduced loads.*

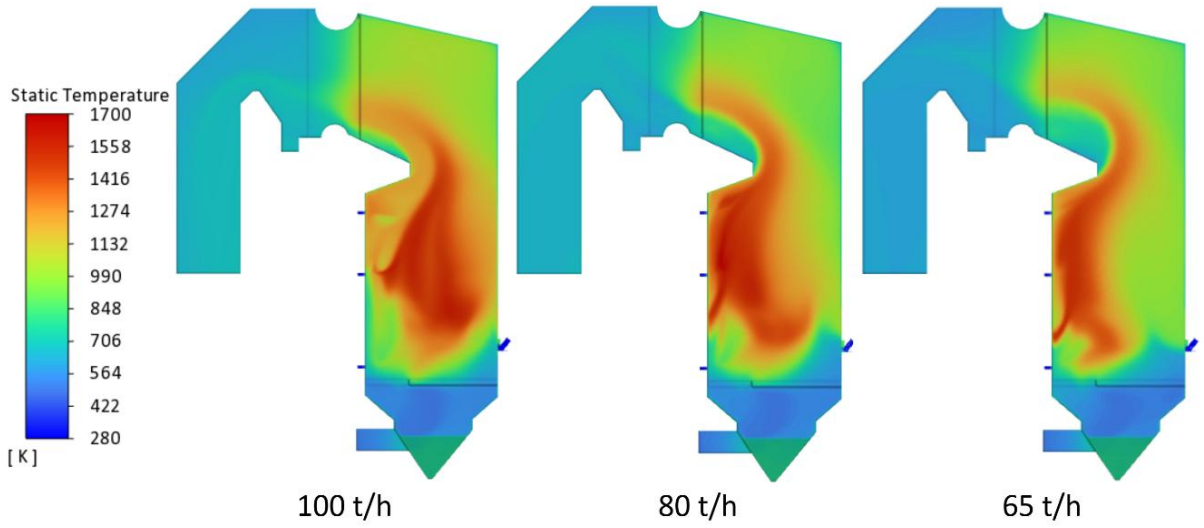

Figure 6.15: *Case study 2 – CFD temperature profiles for full and reduced loads.*

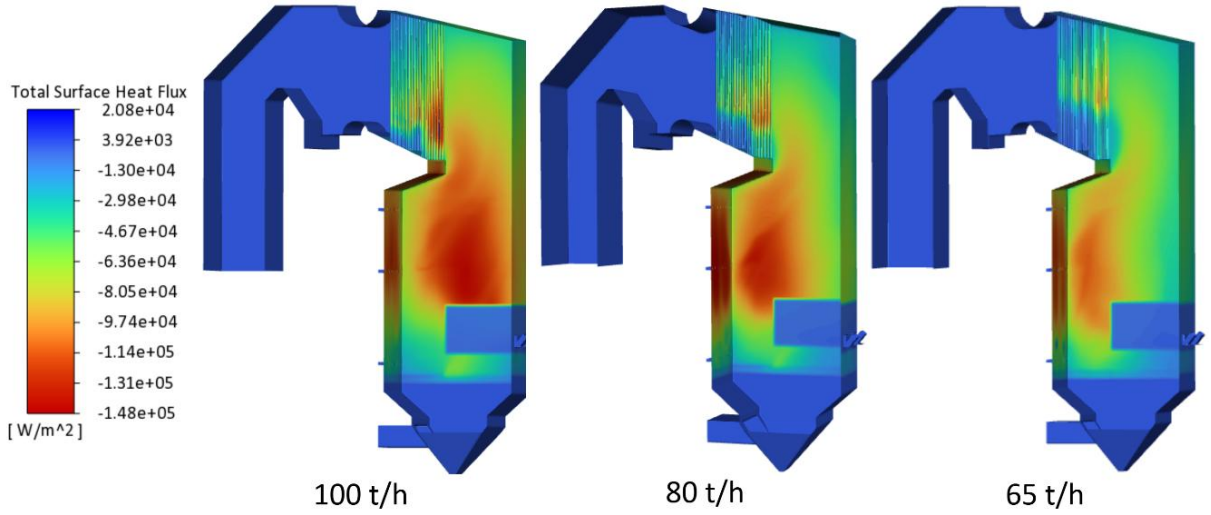

Figure 6.16: *Case study 2 – CFD total surface heat flux profile for full and reduced loads.*

Analysis of Energy Distribution at 80 t/h

The comparison of energy outflow between the CFD and 0-D models for the 80 t/h load case is shown in Table 6-13. Although the overall energy output error remains less than 1% for the 0-D models compared to the CFD, discrepancies emerge when analysing specific heat distributions, as was observed for the full load case and Case Study 1.

The P1 and P2 models both overpredict $\dot{Q}_{ww}$ by 6.3% and 12.8%, respectively, while the D1 and D2 models show better agreement with the CFD, with relative errors of -5.0% and 2.4%. However, the performance of the models in predicting $\dot{Q}_{rf}$ reveals significant discrepancies. The 0-D models exhibit large underpredictions, with the direct method models showing the highest relative errors, exceeding 80% in both D1 and D2. The P1 and P2 models, while better, still significantly underpredict $\dot{Q}_{rf}$, with errors of 28.2% and 36.0%, respectively.

The predicted $\dot{Q}_{rad_{fe}}$ follows a similarly inconsistent trend, which mirrors the trend observed in the smaller case study. The P1 and P2 models underpredict $\dot{Q}_{rad_{fe}}$ by 29.1% and 24.8%, respectively, indicating divergent behaviour in the projected method models. The direct method models also exhibit poor performance, underpredicting $\dot{Q}_{rad_{fe}}$ by -60.9% for D1 and -57.9% for D2. These errors indicate that the 0-D models show limitations in accurately accounting for the direct radiation through the furnace exit, an aspect of radiative heat transfer that seemingly becomes more challenging to model at lower loads for both case studies.

In contrast, $\dot{Q}_{fg_{fe}}$ predictions show a much closer alignment with the CFD. The P1 model demonstrates good agreement, with a relative error of just 0.2%, while the P2 model underpredicts

$\dot{Q}_{fg_{fe}}$ by 2.4%. The direct methods also show reasonable accuracy, with relative errors of 6.7% for D1 and 4.0% for D2.

Table 6-13: *CFD vs. 0-D models (80 t/h) – Comparison of furnace energy outflow [kW].*

Description	$\dot{Q}_{ww}$	$\dot{Q}_{rf}$	$\dot{Q}_{rad_{fe}}$	$\dot{Q}_{fg_{fe}}$	$\dot{Q}_{rad_{loss}}$	$\dot{Q}_{fa_{fe}}$	$\dot{Q}_{ba}$	Sum
CFD	24,059	178	5,136	69,438		423	101	99,334
P1 model								
P1	25,574	229	3,641	69,577	152	409	101	99,683
Relative error	*6.3%*	*28.2%*	*-29.1%*	*0.2%*	-	*-3.1%*	*0.0%*	*0.4%*
P2 model								
P2	27,139	243	3,863	67,781	161	396	101	99,683
Relative error	*12.8%*	*36.0%*	*-24.8%*	*-2.4%*	-	*-6.4%*	*0.0%*	*0.4%*
D1 model								
D1	22,847	32	2,009	74,122	129	444	101	99,683
Relative error	*-5.0%*	*-81.8%*	*-60.9%*	*6.7%*	-	*5.0%*	*0.0%*	*0.4%*
D2 model								
D2	24,631	35	2,165	72,184	139	429	101	99,683
Relative error	*2.4%*	*-80.4%*	*-57.9%*	*4.0%*	-	*1.6%*	*0.0%*	*0.4%*

Analysis of Energy Distribution at 65 t/h

The 65 t/h load case exhibits a continuation of the trends seen at 80 t/h, but with some notable differences (Table 6-14). The P1 model continues to overpredict $\dot{Q}_{ww}$, but with a reduced relative error of 5.5%, while the P2 model exhibits a larger error of 11.6%. The direct methods, D1 and D2, once again demonstrate better accuracy, with errors of -4.5% and 2.4%, respectively. These results further reinforce the observation that the direct method is more reliable for predicting waterwall heat uptake at reduced loads for this particular boiler.

Table 6-14: *CFD vs. 0-D models (65 t/h) – Comparison of furnace energy outflow [kW].*

Description	$\dot{Q}_{ww}$	$\dot{Q}_{rf}$	$\dot{Q}_{rad_{fe}}$	$\dot{Q}_{fg_{fe}}$	$\dot{Q}_{rad_{loss}}$	$\dot{Q}_{fa_{fe}}$	$\dot{Q}_{ba}$	Sum
CFD	21,100	152	5,394	51,569	-	259	112	78,586
P1 model								
P1	22,269	199	3,170	52,546	132	259	112	78,688
Relative error	*5.5%*	*30.8%*	*-41.2%*	*1.9%*	-	*0.1%*	*0.0%*	*0.1%*
P2 model								
P2	23,538	210	3,351	51,088	140	249	112	78,688
Relative error	*11.6%*	*38.2%*	*-37.9%*	*-0.9%*	-	*-3.7%*	*0.0%*	*0.1%*
D1 model								
D1	20,146	29	1,347	56,658	111	286	112	78,688
Relative error	*-4.5%*	*-81.2%*	*-75.0%*	*9.9%*	-	*10.5%*	*0.0%*	*0.1%*
D2 model								
D2	21,610	31	1,396	55,145	119	276	112	78,688
Relative error	*2.4%*	*-79.8%*	*-74.1%*	*6.9%*	-	*6.7%*	*0.0%*	*0.1%*

The 0-D models show considerable limitations in predicting $\dot{Q}_{rf}$ and $\dot{Q}_{rad_{fe}}$, as observed in both the full-load case and the reduced load case at 80 t/h. Interestingly, $\dot{Q}_{rad_{fe}}$ increases from the 80 t/h case to the 65 t/h case, likely due to the constant flow of spreader air, which alters the combustion dynamics within the furnace. This constant flow of spreader air affects the vertical distribution of combustion gases, shifting the combustion zone higher in the furnace. As a result, the hot combustion gases are more exposed to the furnace exit, leading to an increase in the direct radiation that escapes through the furnace exit.

However, the 0-D models do not adequately capture these complex interactions. Their simplified nature fails to account for aspects of the thermal dynamics, such as spatial temperature variations and the impact of different airflow patterns on heat transfer. Consequently, the models show

limitations in accurately representing the intricate heat transfer processes occurring within the furnace, resulting in significant discrepancies in the predictions of $\dot{Q}_{rad_{fe}}$.

Nonetheless, the projected method models perform relatively well in predicting $\dot{Q}_{fg_{fe}}$, with P1 showing a reduced error of 1.9% and P2 underpredicting by 0.9%. The direct method models show higher errors of 9.9% for D1 and 6.9% for D2.

Analysis of Predicted Flue Gas and Wall Temperatures

The analysis of flue gas and wall temperatures provides additional insights into the performance of the 0-D models under reduced load conditions. Figure 6.17 illustrates the discretised temperature profile for the reduced load cases, demonstrating that the profile of the volume-averaged temperature changes with a reduction in load. For the 65 t/h case, the maximum temperature zone shifts from just above the refractory (located between 1.4 m and 3.75 m) to a higher position within the furnace. This shift is mainly due to the cooling effect of the spreader air, which also correlates with the observed increase in $\dot{Q}_{rad_{fe}}$ when reducing the load from 80 t/h to 65 t/h. Notably, the highest temperature zone is 9.7 m along the furnace height in the 65 t/h case, corresponding to a relative height of 0.55 m. In contrast, the maximum temperature zone is at 4.7 m in the 80 t/h case, which translates to a relative height of 0.27 m.

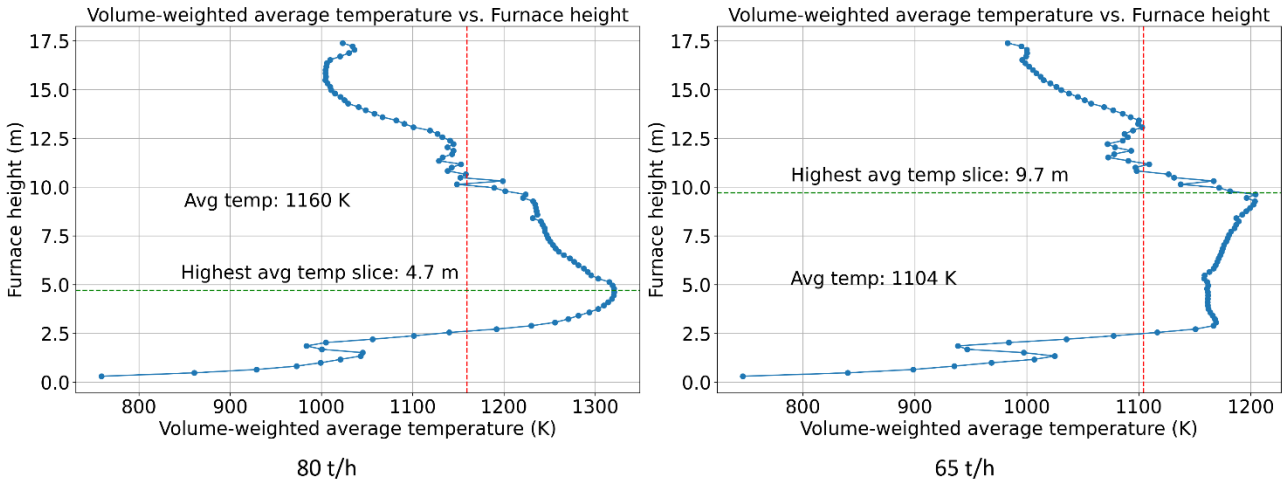

Figure 6.17: *Discretised furnace temperature profile – 80 t/h load (left) and 65 t/h load (right).*

Table 6-15 compares the temperatures predicted by the CFD model and the 0-D models, including the relative errors between them. For the 80 t/h case, the 0-D models track $T_{fg_{fe}}$, with relative errors of less than 5%, but are seen to show limitations in the prediction of T_{fg}. As previously discussed, the direct method presents limitations in its approach to wall temperature predictions. Interestingly, T_{ww} aligns well with the CFD results, which is particularly evident in the predictions

for the waterwall heat uptake $\dot{Q}_{ww}$, where it shows good agreement for the direct method models. Conversely, T_{rf} reveals significant relative errors, which correspondingly affect the predictions of $\dot{Q}_{rf}$.

Table 6-15: *CFD vs. 0-D models (80 t/h & 65 t/h) – Comparison of furnace temperatures [K].*

Description		$T_{fg_{fe}}$	***Error***	T_{fg}	***Error***	T_{ww}	***Error***	T_{rf}	***Error***	T_w	***Error***
80 t/h	CFD	1,166	-	1,160	-	623	-	993	-	651	-
	P1	1,138	*-2.3%*	1,297	*11.8%*	-	-	-	-	-	-
	P2	1,109	*-4.8%*	1,271	*9.6%*	-	-	-	-	-	-
	D1	1,208	*3.7%*	1,208	*4.1%*	612	*-1.8%*	612	*-38.4%*	612	*-6.0%*
	D2	1,178	*1.1%*	1,178	*1.6%*	620	*-0.5%*	620	*-37.6%*	620	*-4.8%*
65 t/h load											
65 t/h	CFD	1,085	-	1,104	-	608	-	917	-	631	-
	P1	1,086	*0.1%*	1,248	*13.0%*	-	-	-	-	-	-
	P2	1,056	*-2.7%*	1,222	*10.7%*	-	-	-	-	-	-
	D1	1,167	*7.6%*	1,167	*5.7%*	600	*-1.3%*	600	*-34.6%*	600	*-4.9%*
	D2	1,137	*4.8%*	1,137	*3.0%*	606	*-0.3%*	606	*-33.9%*	606	*-3.9%*

For the 65 t/h case, the project method models maintain a relative error of less than 5% for $T_{fg_{fe}}$. However, the direct method exhibits greater deviations in this regard. The 0-D models continue to show limitations in predicting T_{fg}, similar to observations from the 80 t/h case. Notably, T_{ww} predictions remain in good agreement with the CFD, which is also reflected in the $\dot{Q}_{ww}$ predictions.

Summary

In conclusion, the projected method models maintain consistent predictions under reduced load conditions for the waterwall heat uptake and flow of heat via the flue gas through the furnace exit, as shown in Figure 6.18 and Figure 6.19. Notably, the relative error remains stable, in contrast to the trends observed for the smaller boiler. However, discrepancies arise in their predictions of direct radiation through the furnace exit, as illustrated in Figure 6.20, where prediction errors increase with decreasing load.

In contrast, the direct method models demonstrate good agreement with the CFD for the waterwall heat uptake for both full-load and reduced-load cases, however, they exhibit limitations in accurately predicting the flow of heat through the furnace exit when operating under reduced load conditions. The direct method models continue to exhibit limitations in predicting direct radiation through the furnace exit, consistent with observations from the smaller case study.

Additionally, the 0-D models reveal a significant improvement in their predictive capabilities for the larger boiler, further highlighting the limitations inherent in their application to smaller boiler systems.

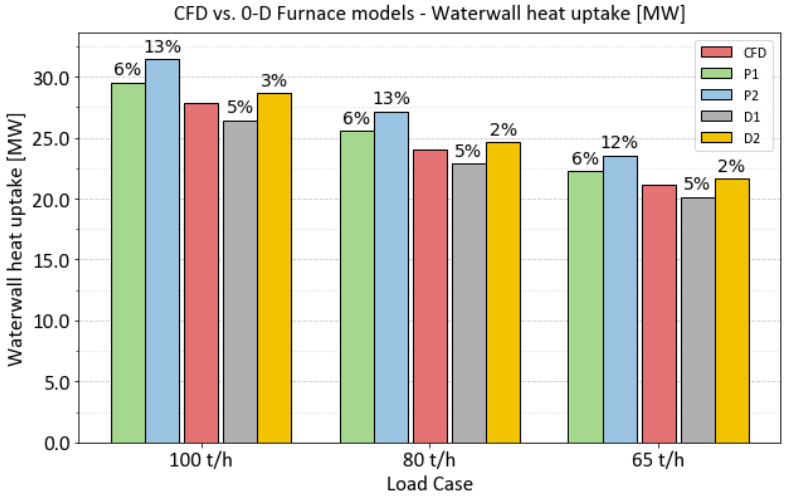

Figure 6.18: *Case study 2 - Waterwall heat uptake across all load conditions.*

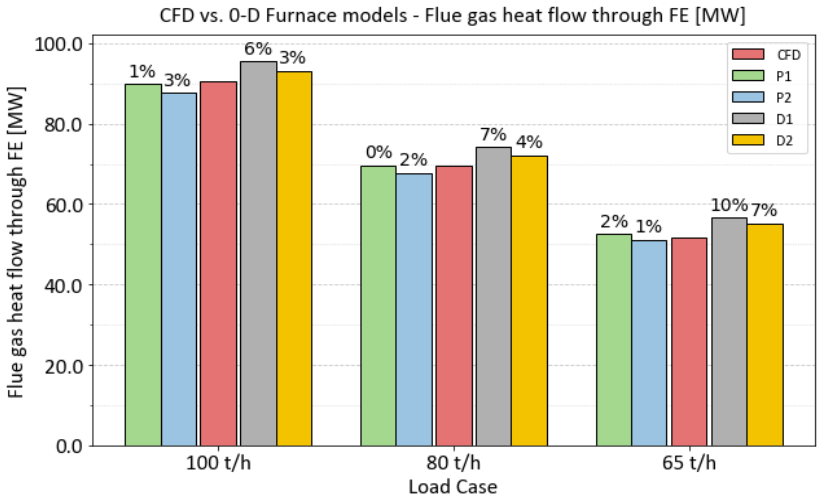

Figure 6.19: *Case study 2 - Flow of heat through the furnace exit across all load conditions.*

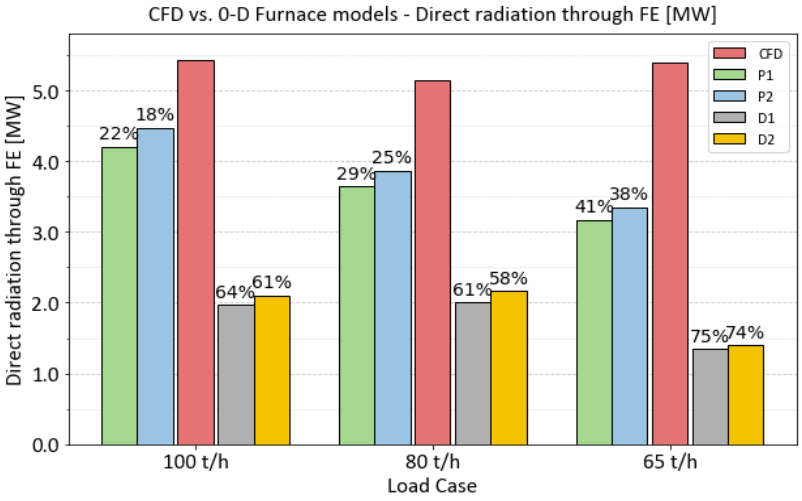

Figure 6.20: *Case study 2 - Direct radiation through the furnace exit across all load conditions.*

6.4 Sensitivity Analysis

This section presents a comprehensive sensitivity analysis aimed at identifying the parameters that significantly influence the performance of the 0-D direct and projected methods. By identifying these key parameters, it becomes possible to better understand the limitations of each model and sets a platform for enhancing their predictive accuracy under varying operational conditions. Section 6.4.1 focuses on the sensitivity analysis for the more empirical projected method, while Section 6.4.2 examines the sensitivity analysis for the more fundamental direct method.

6.4.1 Projected Method

Key Parameters

The sensitivity analysis for the projected method was performed across both full-load and reduced-load conditions for both case study boilers. Several key input parameters were chosen for this analysis, as outlined in Table 6-16, based on their empirical nature or the uncertainty associated with their values.

The emissivity of the gas-particle mixture (ε_{gp}) is determined either using the standard or the high ash method. Since both methods are semi-empirical, they introduce a level of uncertainty into the 0-D model. This uncertainty is evident in the differing results observed in Case Studies 1 and 2, which highlight the influence of the chosen method on the performance of the 0-D models, underscoring the need to quantify the sensitivity of the model to ε_{gp}.

Table 6-16: *Selected parameters – Projected method sensitivity analysis.*

Input	Description		Input	Description
η_{fe}	Non-uniformity factor (furnace exit)		x_{ww}	Angular coefficient (waterwall)
β_{fe}	Reradiation coefficient (furnace exit)		x_{rf}	Angular coefficient (refractory)
ε_{gp}	Emissivity of g-p mixture (furnace)		x_{fe}	Angular coefficient (furnace exit)
η_{rf}	Non-uniformity factor (refractory)		d_p	Particle diameter (fly ash)
ξ_{ww}	Fouling factor (waterwall)		M_{fl}	Flame modification factor
ξ_{rf}	Fouling factor (refractory)		$c_{p_{ash}}$	Specific heat capacity of ash
ξ_{fe}	Fouling factor (furnace exit)			

Sensitivity Methodology

The sensitivity of key output variables such as the waterwall heat uptake and FEGT was analysed using a one at a time perturbation approach. The sensitivity coefficient, denoted as $C_{S_{x,y}}$, describes how an output variable (y) changes in response to a change in input (x), as shown in Equation 6.1.

$$C_{S_{x_i,y_j}} = \frac{\partial y_j}{\partial x_i} \tag{6.1}$$

The sensitivity index of each parameter was quantified using the root-sum-square method as shown in Equation 6.2. This equation calculates the contribution of the sensitivity of each parameter to the overall system by squaring the sensitivity coefficient, normalising it by the total sum of squared sensitivity coefficients, and expressing it as a percentage.

$$S_{x_i,y_j} = \frac{C^2_{S_{x_i,y_j}}}{\sum C_{S^2_{x_i,y_j}}} \cdot 100\% \tag{6.2}$$

Additionally, the directionality of the perturbations (whether they increased or decreased the output) was taken into account in Equation 6.3. This modification ensures that the sensitivity index reflects not only the magnitude but also the direction of the effect of each parameter on the output.

$$S_{x_i,y_j} = S_{x_i,y_j} \cdot \frac{C_{S_{x_i,y_j}}}{\left|C_{S_{x_i,y_j}}\right|} \tag{6.3}$$

Case Study 1 – Projected Method Sensitivity Analysis

Using the equations above, the sensitivity analysis was performed for a 1% perturbation to the selected input parameters. Table 6-17 provides the sensitivity results for Case Study 1 under full load operating conditions. In this table, the shaded cells in each column indicate the parameters with the most significant influence on each output variable, with the darkest shade representing the parameter that has the highest impact. This layout provides a clear visual representation of how various inputs affect the behaviour of the system, emphasising the parameters that require careful consideration in the development of the 0-D furnace models.

It is important to note that for this analysis, $\dot{Q}_{fg_{fe}}$ is directly proportional to T_{fe}. As a result, the sensitivity of $\dot{Q}_{fg_{fe}}$ is equal to the sensitivity of T_{fe}. Therefore, any changes in T_{fe} will have a corresponding effect on $\dot{Q}_{fg_{fe}}$, reflecting their interdependence in the system.

Table 6-17: *Case study 1 (45 t/h) – Projected method sensitivity at 1% perturbation.*

Parameter	Value	Unit	$T_{fg_{fe}}$	T_{fg}	$\dot{Q}_{fur}$	$\dot{Q}_{ww}$	$\dot{Q}_{rf}$	$\dot{Q}_{rad_{fe}}$	$\dot{Q}_{fg_{fe}}$
η_{fe}	0.80	-	0.0%	0.0%	0.0%	-1.3%	0.0%	18.9%	0.0%
β_{fe}	1.00	-	0.0%	0.0%	0.0%	-0.8%	0.0%	12.1%	0.0%
ε_{gp}	0.43	-	-21.0%	-31.8%	21.0%	18.3%	0.7%	8.4%	-21.0%
η_{rf}	0.64	-	0.0%	0.0%	0.0%	0.0%	2.3%	0.0%	0.0%
ξ_{ww}	0.60	m²K/W	-3.8%	-5.7%	3.8%	9.8%	-0.9%	-11.0%	-3.8%
ξ_{rf}	0.10	m²K/W	-0.1%	-0.2%	0.1%	-0.1%	92.7%	-0.4%	-0.1%
ξ_{fe}	1.00	m²K/W	-0.1%	-0.1%	0.1%	-0.2%	0.0%	9.0%	-0.1%
x_{ww}	0.92	-	-4.8%	-7.3%	4.8%	8.5%	-0.2%	-2.5%	-4.8%
x_{rf}	1.00	-	0.0%	-0.1%	0.0%	0.0%	1.0%	0.0%	0.0%
x_{fe}	1.00	-	-0.2%	-0.2%	0.2%	-0.1%	0.0%	9.5%	-0.2%
d_p	20.00	µm	0.0%	0.0%	0.0%	0.0%	0.0%	0.0%	0.0%
M_{fl}	0.52	-	-70.0%	54.5%	70.0%	60.7%	2.2%	28.1%	-70.0%
$c_{p_{ash}}$	1200.00	J/kg·K	0.0%	0.0%	0.0%	0.0%	0.0%	0.0%	0.0%

Similarly, the total radiation in the furnace, $\dot{Q}_{fur}$ is composed of three components: $\dot{Q}_{ww}$, $\dot{Q}_{rf}$ and $\dot{Q}_{rad_{fe}}$. The table shows that the sensitivity of $\dot{Q}_{fur}$ is equal and opposite to that of $\dot{Q}_{fg_{fe}}$, indicating a direct relationship between radiation heat transfer and the FEGT. This finding indicates a compensatory relationship between the radiation heat transfer in the furnace and the heat transfer from the flue gas. Specifically, as radiation heat transfer within the furnace increases, the heat flow of the flue gas through the furnace exit decreases, and vice versa.

The results show that M_{fl} is the most influential parameter across several outputs. For instance, an increase in M_{fl} leads to a decrease in $T_{fg_{fe}}$ but an increase in $\dot{Q}_{ww}$ and $\dot{Q}_{rad_{fe}}$. This relationship is intuitive: a higher M_{fl} indicates a lower flame position in the furnace, which leads to more heat being absorbed by the waterwalls, thereby reducing the FEGT. This observation aligns with Equation *3.53* from Section 3.5.1, which shows that $T_{fg_{fe}}$ is inversely proportional to M_{fl}.

Interestingly, while $T_{fg_{fe}}$ decreases with an increase in M_{fl}, the mean gas temperature (T_{fg}) rises. This reflects the complex heat redistribution within the furnace, where a lower flame position increases the heat absorbed by the waterwalls and alters the balance between convective and radiative heat transfer.

The emissivity of the gas-particle mixture (ε_{gp}) is the second most influential parameter affecting the thermal performance of the furnace. An increase in ε_{gp} results in a more emissive gas mixture, which enhances the heat absorption by the waterwall ($\dot{Q}_{ww}$) and consequently lowers the furnace exit gas temperature ($T_{fg_{fe}}$). This change also leads to an increase in the direct radiation through the furnace exit ($\dot{Q}_{rad_{fe}}$).

These findings highlight the crucial role that the radiative properties of the gas-particle mixture play in the overall heat distribution within the furnace, highlighting the importance of accurate thermal radiation models. In this study, both the high ash and standard models exhibited variability in their predictions, which in turn affected the overall furnace predictions. The sensitivity analysis confirmed the significance of ε_{gp}, reinforcing its status as an important parameter in modelling furnace behaviour.

The analysis also shows that x_{ww} has a significant influence on $\dot{Q}_{ww}$ and $T_{fg_{fe}}$. An increase in x_{ww} results in more heat being absorbed by the waterwalls ($\dot{Q}_{ww}$), which subsequently lowers the FEGT ($T_{fg_{fe}}$) and reduces heat radiated from flame through the furnace exit ($\dot{Q}_{rad_{fe}}$). This is because a higher x_{ww} increases the effective surface area available for radiation, enhancing the waterwall absorption and reducing the flow of heat through the furnace exit.

Moreover, the sensitivity analysis was conducted across different perturbation levels and lower load cases. The results, presented in 0, demonstrate that the sensitivity profiles of the parameters exhibit negligible changes across varying perturbations and load conditions.

Case Study 2 – Projected Method Sensitivity Analysis

The sensitivity analysis for the larger boiler in Case Study 2, shown in Table 6-18, reveals a similar profile to that of the smaller boiler, with a few important distinctions.

Notably, the larger boiler is less sensitive to ε_{gp}, while its sensitivity to the M_{fl} is greater. This difference can be attributed to the larger furnace volume-to-surface-area ratio in the larger boiler, which results in a longer mean beam length (4.484 m compared to 3.021 m for the smaller boiler). A longer mean beam length implies that the gas has a larger radiation thickness and is more emissive, making radiative heat transfer more dominant in the larger boiler. Consequently, changes

in the flame position (controlled by M_{fl}) have a more pronounced impact on heat transfer in the larger boiler compared to the smaller one.

Table 6-18: *Case study 2 (100 t/h) – Projected method sensitivity at 1% perturbation.*

Parameter	Value	Unit	$T_{fg_{fe}}$	T_{fg}	$\dot{Q}_{fur}$	$\dot{Q}_{ww}$	$\dot{Q}_{rf}$	$\dot{Q}_{rad_{fe}}$	$\dot{Q}_{fg_{fe}}$
η_{fe}	0.80	-	0.0%	0.0%	0.0%	-0.9%	0.0%	19.5%	0.0%
β_{fe}	1.00	-	0.0%	0.0%	0.0%	-0.6%	0.0%	12.5%	0.0%
ε_{gp}	0.51	-	-15.5%	-26.4%	15.5%	13.6%	0.4%	5.8%	-15.5%
η_{rf}	0.64	-	0.0%	0.0%	0.0%	0.0%	2.3%	0.0%	0.0%
ξ_{ww}	0.60	m²K/W	-5.4%	-9.3%	5.4%	11.0%	-0.9%	-11.9%	-5.4%
ξ_{rf}	0.10	m²K/W	0.0%	-0.1%	0.0%	0.0%	93.1%	-0.1%	0.0%
ξ_{fe}	1.00	m²K/W	-0.1%	-0.1%	0.1%	-0.2%	0.0%	9.9%	-0.1%
x_{ww}	0.92	-	-5.9%	-10.0%	5.9%	9.1%	-0.2%	-2.9%	-5.9%
x_{rf}	1.00	-	0.0%	0.0%	0.0%	0.0%	1.0%	0.0%	0.0%
x_{fe}	1.00	-	-0.1%	-0.2%	0.1%	-0.1%	0.0%	10.2%	-0.1%
d_p	800.80	µm	0.0%	0.0%	0.0%	0.0%	0.0%	0.0%	0.0%
M_{fl}	0.52	-	-73.0%	54.0%	73.0%	64.4%	2.1%	27.3%	-73.0%
$c_{p_{ash}}$	1200.00	J/kg·K	0.0%	0.0%	0.0%	0.0%	0.0%	0.0%	0.0%

As was observed with the smaller boiler, the sensitivity profile remains consistent across different perturbation levels and load conditions, as shown in 0. This consistency suggests that the relative influence of the key parameters, such as M_{fl} and ε_{gp}, is robust across a range of operating conditions.

Overall, the sensitivity analysis highlights the importance of key parameters such as the flame modification factor (M_{fl}), emissivity of the gas-particle suspension (ε_{gp}), and the angular coefficient of the waterwalls (x_{ww}) in governing the heat transfer dynamics within the furnace. The direct relationships between these parameters and critical outputs such as $T_{fg_{fe}}$, $\dot{Q}_{ww}$, and $\dot{Q}_{rad_{fe}}$ provide valuable insights for improving the performance of the projected method.

The slight variations in the sensitivity profiles between the smaller and larger boilers further highlight how furnace size and geometry influence heat transfer behaviour. This demonstrates that great care has to be taken when selecting the flame modification factor for a specific boiler application and that the recommended values i.e., 0.52 for furnaces utilising travelling grate or stoker systems [7] may not always provide sufficient accuracy as shown for the smaller case study boiler.

6.4.2 Direct Method

The sensitivity analysis for the direct method employed a methodology similar to that used for the projected method, with notable distinctions in focus and parameters. The parameters examined in this analysis are outlined in Table 6-19.

Key Parameters

The direct method differs from the projected method primarily in its direct approach to calculating radiative heat transfer, placing significant emphasis on the properties of the furnace walls and their interactions with the surrounding medium. In contrast, the projected method focuses on the mean gas temperature (T_{fg}) as a key variable. In the direct method, the assumption that T_{fg} equals $T_{fg_{fe}}$ shifts the focus from gas temperature to wall temperature, necessitating an evaluation of how variations in different parameters affect thermal dynamics at the wall level.

Key parameters selected for the analysis (Table 6-19) include the emissivity (ε_{gp}) and absorptivity ($\propto_{gp}$) of the gas-particle mixture, as variations in these properties directly impact the radiative heat transfer and the overall thermal dynamics within the furnace. Furthermore, the thermal characteristics of the furnace walls, particularly their emissivity (ε_w) and thermal conductivity (k), play a critical role in the performance of the model. These wall properties influence the absorption and emission of thermal radiation, thereby affecting temperature profiles and heat distribution throughout the system.

The thermal properties of fouling layers (k_{fo}) are also considered in this analysis. Fouling can alter the effective emissivity and absorptivity of the furnace walls, thus impacting overall heat transfer distribution. By systematically assessing the sensitivity of these parameters, the D1 model provides valuable insights into how variations in wall properties and gas-particle interactions affect furnace thermal performance. This comprehensive evaluation is expected to enhance the understanding of the key factors driving heat transfer distribution within the furnace.

Table 6-19: *Selected parameters – Direct method sensitivity analysis.*

Input	Description		Input	Description
ε_{gp}	Emissivity of g-p mixture (furnace)		x_{rf}	Angular coefficient (refractory)
$\varepsilon_{gp_{hx}}$	Emissivity of g-p mixture (HX)		x_{fe}	Angular coefficient (furnace exit)
$\propto_{gp}$	Absorptivity of g-p mixture (furnace)		d_p	Particle diameter (fly ash)
$\propto_{gp_{hx}}$	Absorptivity of g-p mixture (HX)		T_{sat}	Saturation temperature (water)
k_{fo}	Thermal conductivity of fouling		$c_{p_{ash}}$	Specific heat capacity of ash
k_{ww}	Thermal conductivity of waterwall		$T_{w_{hx}}$	Temperature of HX wall
k_{rf}	Thermal conductivity of refractory		ε_w	Emissivity of furnace walls
h_i	Heat transfer coefficient		$\varepsilon_{w_{hx}}$	Emissivity of HX walls
x_{ww}	Angular coefficient (waterwall)			

Case Study 1 – Direct Method Sensitivity Analysis

In the case of the smaller boiler (Case Study 1) at full load, the emissivity of the gas-particle mixture (ε_{gp}) emerged as the most influential parameter, significantly affecting $T_{fg_{fe}}$, the mean wall temperature (T_w), and $\dot{Q}_{fg_{fe}}$. Table 6-20 shows that an increase in ε_{gp} leads to a reduction in $T_{fg_{fe}}$ and an increase in $\dot{Q}_{ww}$, mirroring the trends observed in the projected method.

For the direct method, it can be seen that ε_{gp} has a significant effect on the overall performance of the model. Therefore, the underprediction of $\dot{Q}_{ww}$ by the direct method for the smaller case could imply that the thermal radiation models for gas-particle suspension need further refinement in order to suit application for the smaller case study boiler. Although the models are based on fundamentals, they have a few empirical correlations which could not necessarily provide acceptable results for models that deviate from the range for which these equations were originally derived.

The angular coefficient of the waterwalls (x_{ww}) also has significant influence in the sensitivity of the direct method. An increase in x_{ww} leads to more heat being absorbed by the waterwalls ($\dot{Q}_{ww}$), resulting in a lower FEGT ($T_{fg_{fe}}$). Similarly, the emissivity of the furnace walls (ε_w) exerts a significant influence on the heat distribution within the furnace, highlighting the importance of accurately specifying wall emissivity for realistic simulations.

Table 6-20: *Case study 1 (45 t/h) – Direct method sensitivity at 1% perturbation.*

Parameter	Value	Unit	$T_{fg_{fe}}$	T_w	$\dot{Q}_{fur}$	$\dot{Q}_{ww}$	$\dot{Q}_{rf}$	$\dot{Q}_{rad_{fe}}$	$\dot{Q}_{fg_{fe}}$
ε_{gp}	0.42	-	-82.0%	62.4%	82.0%	82.8%	54.5%	-13.9%	-82.0%
$\varepsilon_{gp_{hx}}$	0.42	-	-1.1%	-0.5%	1.1%	-0.6%	-0.4%	68.5%	-1.1%
$\propto_{gp}$	0.52	-	2.1%	-1.6%	-2.1%	-2.1%	-1.4%	0.4%	2.1%
$\propto_{gp_{hx}}$	0.48	-	0.1%	0.0%	-0.1%	0.1%	0.0%	-6.8%	0.1%
k_{fo}	1.00	W/m·K	-0.1%	-24.7%	0.1%	0.1%	-20.7%	0.0%	-0.1%
k_{ww}	47.0	W/m·K	0.0%	0.0%	0.0%	0.0%	0.0%	0.0%	0.0%
k_{rf}	1.40	W/m·K	0.0%	0.0%	0.0%	0.0%	13.5%	0.0%	0.0%
h_i	20,000	W/m^{2}K	0.0%	0.0%	0.0%	0.0%	0.0%	0.0%	0.0%
x_{ww}	0.92	-	-7.8%	6.0%	7.8%	7.9%	5.2%	-1.3%	-7.8%
x_{rf}	1.00	-	-0.2%	0.2%	0.2%	0.2%	0.2%	0.0%	-0.2%
x_{fe}	1.00	-	-0.5%	0.0%	0.5%	0.0%	0.0%	5.3%	-0.5%
d_p	20.00	µm	0.0%	0.0%	0.0%	0.0%	0.0%	0.0%	0.0%
T_{sat}	558.2	K	0.0%	0.0%	0.0%	0.0%	0.0%	0.0%	0.0%
$c_{p_{ash}}$	1,200	J/kg·K	0.0%	0.0%	0.0%	0.0%	0.0%	0.0%	0.0%
$T_{w_{hx}}$	924.2	K	0.0%	0.0%	0.0%	0.0%	0.0%	0.0%	0.0%
ε_w	0.80	-	-6.0%	4.6%	6.0%	6.1%	4.0%	-1.0%	-6.0%
$\varepsilon_{w_{hx}}$	0.80	-	0.0%	0.0%	0.0%	0.0%	0.0%	2.7%	0.0%

T_w and $\dot{Q}_{rf}$ exhibit notable sensitivity to k_{fo}. Conversely, the outputs display low sensitivity to several other parameters, including k_{ww}, k_{rf}, h_i, T_{sat}, $c_{p_{ash}}$, $T_{w_{hx}}$ and $\varepsilon_{w_{hx}}$. Among the input parameters, the emissivity of the gas particle mixture at the heat exchanger ($\varepsilon_{gp_{hx}}$) situated directly after the furnace exit plane, has the most pronounced impact on $\dot{Q}_{rad_{fe}}$. Similar to the P1 sensitivity analysis, the sensitivity profile remained consistent across varying perturbation values and under reduced load conditions (Appendix F).

Case Study 2 – Direct Method Sensitivity Analysis

The full-load results for the larger boiler in Case Study 2, presented in Table 6-21, align with the trends observed in Case Study 1, although there are notable variations. In the larger boiler, while the sensitivity to ε_{gp} remains significant, it is lower compared to that of the smaller boiler. It is important to note that the direct method predicts a higher FEGT for the smaller boiler relative to the larger one. This discrepancy contributes to the more pronounced effects of the sensitivity of ε_{gp} observed in the smaller boiler.

Table 6-21: *Case study 2 (100 t/h) – Direct method sensitivity at 1% perturbation.*

Parameter	Value	Unit	$T_{fg_{fe}}$	T_w	$\dot{Q}_{fur}$	$\dot{Q}_{ww}$	$\dot{Q}_{rf}$	$\dot{Q}_{rad_{fe}}$	$\dot{Q}_{fg_{fe}}$
ε_{gp}	0.49	-	-73.5%	50.4%	73.5%	74.0%	42.5%	-14.5%	-73.5%
$\varepsilon_{gp_{hx}}$	0.49	-	-0.7%	-0.4%	0.7%	-0.5%	-0.3%	62.5%	-0.7%
$\propto_{gp}$	0.63	-	1.9%	-1.3%	-1.9%	-1.9%	-1.1%	0.4%	1.9%
$\propto_{gp_{hx}}$	0.58	-	0.1%	0.0%	-0.1%	0.1%	0.0%	-5.8%	0.1%
k_{fo}	1.00	W/m·K	0.0%	-31.9%	0.0%	0.0%	-26.0%	0.0%	0.0%
k_{ww}	47.0	W/m·K	0.0%	0.0%	0.0%	0.0%	0.0%	0.0%	0.0%
k_{rf}	1.40	W/m·K	0.0%	0.0%	0.0%	0.0%	16.6%	0.0%	0.0%
h_i	20,000	W/m^{2}K	0.0%	0.0%	0.0%	0.0%	0.0%	0.0%	0.0%
x_{ww}	0.92	-	-12.4%	8.5%	12.4%	12.5%	7.2%	-2.5%	-12.4%
x_{rf}	1.00	-	-0.1%	0.1%	0.1%	0.1%	0.0%	0.0%	-0.1%
x_{fe}	1.00	-	-0.4%	0.0%	0.4%	0.0%	0.0%	7.2%	-0.4%
d_p	800.8	µm	0.0%	0.0%	0.0%	0.0%	0.0%	0.0%	0.0%
T_{sat}	509.1	K	0.0%	0.0%	0.0%	0.0%	0.0%	0.0%	0.0%
cp_{ash}	1200	J/kg K	0.0%	0.0%	0.0%	0.0%	0.0%	0.0%	0.0%
$T_{w_{hx}}$	872.8	K	0.0%	0.0%	0.0%	0.0%	0.0%	0.0%	0.0%
ε_w	0.80	-	-10.8%	7.4%	10.8%	10.9%	6.3%	-2.1%	-10.8%
$\varepsilon_{w_{hx}}$	0.80	-	-0.1%	0.0%	0.1%	0.0%	0.0%	5.0%	-0.1%

Table 6-21 also illustrates an increased sensitivity to x_{ww} in the larger boiler, which can be attributed to the greater waterwall surface area. This increase amplifies the influence of changes in x_{ww} on the total radiation absorbed by the waterwalls. The findings highlight the need for careful consideration of furnace geometry in 0-D thermal models, as parameters such as x_{ww} exhibit a more pronounced impact on the overall heat transfer distribution in larger systems. Furthermore, k_{fo} is observed to have a more significant effect in the larger boiler, due to both the increased surface area and the greater potential for fouling.

Consistent with Case Study 1, the percentage perturbation did not significantly impact the sensitivity profile for Case Study 2, maintaining a consistent sensitivity profile even under reduced load conditions (Appendix F).

The sensitivity analysis for both Case Study 1 and Case Study 2 reveal that the emissivity of the gas-particle mixture is the most influential parameter affecting thermal dynamics within the furnace for the direct method. This finding highlights the need for the evaluation of the thermal radiation models for gas-solid mixture to ensure accuracy. The contrasting sensitivity profiles between the smaller and larger boilers further highlight how furnace size and geometry influence heat transfer behaviour, emphasising the need for tailored calibration strategies based on specific boiler configurations.

6.5 Results Summary

This section compared the 0-D models to validated CFD models, revealing performance differences based on boiler size and load conditions. For the smaller 45 t/h boiler, both the projected and direct method models deviated significantly from the CFD results, especially under reduced loads. The projected–standard (P2) model performed better than the other models but still showed limitations in predicting waterwall heat uptake. Overall, the 0-D models demonstrated constraints in accurately capturing the heat transfer dynamics of the smaller boiler.

For the larger boiler, 0-D model predictions improved notably. The direct method models performed better than the projected method models in predicting the waterwall heat uptake, with the direct – high ash (D2) model performing better in comparison to the direct – standard model (D1). While the direct method models aligned well with CFD results for furnace exit gas temperature at full load, greater variances were observed at reduced loads. The projected method models exhibited limitations in predicting waterwall heat uptake but demonstrated good agreement in predicting the furnace exit gas temperature across all loads, particularly with the high ash (P1) model.

A sensitivity analysis identified key influencing parameters for each model. The flame modification factor had the greatest influence on the projected method, while gas-particle emissivity was key for the direct method. Boiler geometry also impacted performance, with larger boilers being more sensitive to wall emissivity and angular coefficients, while smaller boilers were more affected by gas-particle emissivity.

These results highlight the difficulties of applying thermal radiation models to boilers of varying sizes, as the complexities introduced by scaling differ significantly from those encountered in smaller boilers. Therefore, boiler size is a crucial factor in determining the accuracy of heat transfer predictions, and model selection must take this into account.

7. Conclusion and Recommendations

The comparative analysis of the 0-D models with CFD simulations highlighted the strengths and limitations of these simplified models in predicting heat transfer within biomass-fired boilers. While the 0-D models demonstrated satisfactory performance in the larger boiler, their predictive capability diminished significantly in the smaller, more compact boiler. In particular, both the projected and the direct method models exhibited inaccuracies in the smaller boiler; however, the projected method yielded better results than the direct method. For the larger boiler, the direct-standard model performed better in predicting waterwall heat uptake, yet it shows limitations in accurately estimating the furnace exit gas temperature at reduced loads. In contrast, the projected-high ash model performed better in this area, with predictions closer to the CFD results.

The sensitivity analysis identified key parameters affecting the accuracy of the 0-D models. In the direct method, emissivity of the gas-particle mixture was the most influential parameter, while the flame modification factor dominated in the projected method, which also showed significant sensitivity to gas-particle mixture emissivity. These findings were consistent with the boiler performance results, which showed that the choice between the high ash model and the standard model significantly influenced predictions for both boilers, although the high ash model did not necessarily perform better in all cases.

Based on these findings, several recommendations can be made. First, model refinement is necessary for smaller boilers, particularly in predicting the waterwall heat uptake, where both the projected method and direct method require calibration and adaptation to adequately address the complexities associated with compact biomass-fired systems. Second, calibration strategies should focus on the most sensitive parameters identified in this study, such as flame modification factor for the projected method and the emissivity of the gas-particle mixture for the direct method, to enhance model accuracy across various boiler configurations. Lastly, future research should extend the analysis to encompass a broader range of biomass-fired boilers with diverse operational characteristics. Emphasis should be placed on improving the performance of the models, particularly under low-load conditions and for smaller boilers, where existing models exhibit significant limitations.

In conclusion, although the 0-D models serve as practical tools for modelling biomass-fired boilers, their application must be approached with caution, particularly in smaller systems and under reduced load conditions. Further refinement and calibration are required to extend their applicability beyond large coal-fired systems and ensure accurate performance predictions across a broader spectrum of biomass boiler configurations.

8. References

[1] M. F. Demirbas, M. Balat, and H. Balat, "Potential contribution of biomass to the sustainable energy development," *Energy Conversion and Management,* vol. 50, no. 7, pp. 1746-1760, 2009/07/01/ 2009, doi: https://doi.org/10.1016/j.enconman.2009.03.013.

[2] *Energy Statistics Pocketbook*: United Nations, New York - Department of Economic and Social Affairs, 2024. [Online]. Available: https://unstats.un.org/unsd/energystats/pubs/documents/2022pb-web.pdf.

[3] L. I. Díez, C. Cortés, and A. Campo, "Modelling of pulverized coal boilers: review and validation of on-line simulation techniques," *Applied Thermal Engineering,* vol. 25, no. 10, pp. 1516-1533, 2005/07/01/ 2005, doi: https://doi.org/10.1016/j.applthermaleng.2004.10.003.

[4] H. Kumar, S. K. Mohapatra, and R. I. Singh, "Review on CFD Modelling of Fluidized Bed Combustion Systems based on Biomass and Co-firing," *Journal of The Institution of Engineers (India): Series C,* vol. 99, no. 4, pp. 449-474, 2018/08/01 2018, doi: 10.1007/s40032-017-0361-2.

[5] Babcock and W. Company, *Steam: its generation and use*. Kessinger Publishing, 2005.

[6] M. Kind, H. Martin, P. Stephan, W. Roetzel, B. Spang, and H. Müller-Steinhagen, "VDI heat atlas,"*)^(Eds.):'Book VDI Heat Atlas'(Springer Berlin/Heidelberg, Germany, 2010, edn.),* 2010.

[7] P. Basu, C. Kefa, and L. Jestin, *Boilers and burners: design and theory*. Springer Science & Business Media, 2012.

[8] Y. Zhang, Q. Li, and H. Zhou, *Theory and calculation of heat transfer in furnaces*. Elsevier, 2016.

[9] G. Tzolakis, P. Papanikolaou, D. Kolokotronis, N. Samaras, A. Tourlidakis, and A. Tomboulides, "Emissions' reduction of a coal-fired power plant via reduction of consumption through simulation and optimization of its mathematical model," *Operational Research,* vol. 10, pp. 71-89, 2010.

[10] S. Chantasiriwan, "Optimum installation of flue gas dryer and additional air heater to increase the efficiency of coal-fired utility boiler," *Energy,* vol. 221, p. 119769, 2021.

[11] P. Rousseau, R. Laubscher, and B. T. Rawlins, "Heat Transfer Analysis Using Thermofluid Network Models for Industrial Biomass and Utility Scale Coal-Fired Boilers," *Energies,* vol. 16, no. 4, p. 1741, 2023.

[12] H. Hajebzadeh, A. N. Ansari, and S. Niazi, "Mathematical modeling and validation of a 320 MW tangentially fired boiler: A case study," *Applied Thermal Engineering,* vol. 146, pp. 232-242, 2019.

[13] M. Trojan, "Modeling of a steam boiler operation using the boiler nonlinear mathematical model," *Energy,* vol. 175, pp. 1194-1208, 2019.

[14] R. Laubscher and E. De Villiers, "Integrated mathematical modelling of a 105 t/h biomass fired industrial watertube boiler system with varying fuel moisture content," *Energy,* vol. 228, p. 120537, 2021.

[15] R. Starkloff, F. Alobaid, K. Karner, B. Epple, M. Schmitz, and F. Boehm, "Development and validation of a dynamic simulation model for a large coal-fired power plant," *Applied Thermal Engineering,* vol. 91, pp. 496-506, 2015.

[16] W. Zima *et al.*, "Thermal calculations of a natural circulation power boiler operating under a wide range of loads," *Energy,* vol. 261, p. 125357, 2022/12/15/ 2022, doi: https://doi.org/10.1016/j.energy.2022.125357.

[17] B. Leckner, "Spectral and total emissivity of water vapor and carbon dioxide," *Combustion and Flame,* vol. 19, no. 1, pp. 33-48, 1972/08/01/ 1972, doi: https://doi.org/10.1016/S0010-2180(72)80084-1.

[18] S. Kakaç, *Boilers, evaporators, and condensers*. John Wiley & Sons, 1991.

[19] V. Ganapathy, *Industrial boilers and heat recovery steam generators: design, applications, and calculations*. CRC Press, 2002.

[20] P. Stephan, S. Kabelac, M. Kind, D. Mewes, K. Schaber, and T. Wetzel, *VDI-Wärmeatlas: Fachlicher Träger VDI-Gesellschaft Verfahrenstechnik und Chemieingenieurwesen*. Springer-Verlag, 2019.

[21] F. Alobaid, N. Mertens, R. Starkloff, T. Lanz, C. Heinze, and B. Epple, "Progress in dynamic simulation of thermal power plants," *Progress in energy and combustion science,* vol. 59, pp. 79-162, 2017.

[22] G. M. Castilla, R. M. Montanes, D. Pallares, and F. Johnsson, "Dynamic modeling of the reactive side in large-scale fluidized bed boilers," *Industrial & Engineering Chemistry Research,* vol. 60, no. 10, pp. 3936-3956, 2021.

[23] P. Orłowski, W. Dobrzański, and E. Szwarc, "Steam boilers," *WNT, Warszawa,* 1979.

[24] J. Taler, P. Dzierwa, D. Taler, and P. Harchut, "Optimization of the boiler start-up taking into account thermal stresses," *Energy,* vol. 92, pp. 160-170, 2015.

[25] E. Oko and M. Wang, "Dynamic modelling, validation and analysis of coal-fired subcritical power plant," *Fuel,* vol. 135, pp. 292-300, 2014.

[26] S. Chandrasekharan, R. C. Panda, and B. Natrajan Swaminathan, "Dynamic analysis of the boiler drum of a coal-fired thermal power plant," *Simulation,* vol. 93, no. 11, pp. 995-1010, 2017.

[27] T. Marx-Schubach and G. Schmitz, "Modeling and simulation of the start-up process of coal fired power plants with post-combustion CO2 capture," *International Journal of Greenhouse Gas Control,* vol. 87, pp. 44-57, 2019/08/01/ 2019, doi: https://doi.org/10.1016/j.ijggc.2019.05.003.

[28] G. Zhang, W. Xu, X. Wang, and Y. Yang, "Analysis and optimization of a coal-fired power plant under a proposed flue gas recirculation mode," *Energy Conversion and Management,* vol. 102, pp. 161-168, 2015/09/15/ 2015, doi: https://doi.org/10.1016/j.enconman.2015.01.073.

[29] P. Rousseau and R. Laubscher, "A thermofluid network-based model for heat transfer in membrane walls of pulverized coal boiler furnaces," *Thermal Science and Engineering Progress,* vol. 18, p. 100547, 2020.

[30] P. Madejski, D. Taler, and J. Taler, "Thermal and flow calculations of platen superheater in large scale CFB boiler," *Energy,* vol. 258, p. 124841, 2022.

[31] H.-G. Brummel, "K4 Thermal Radiation of Gas–Solids–Dispersions," in *VDI Heat Atlas*, 1993.

[32] R. Laubscher and P. Rousseau, "Power Plant Boilers: Thermofluid Processes and Controls," University of Cape Town, Course Notes, 2023.

[33] Y. A. Cengel, M. A. Boles, and M. Kanoğlu, *Thermodynamics: an engineering approach*. McGraw-hill New York, 2011.

[34] I. H. Bell, J. Wronski, S. Quoilin, and V. Lemort, "Pure and pseudo-pure fluid thermophysical property evaluation and the open-source thermophysical property library CoolProp," *Industrial & engineering chemistry research,* vol. 53, no. 6, pp. 2498-2508, 2014.

[35] R. Laubscher and S. van der Merwe, "Heat transfer modelling of semi-suspension biomass fired industrial watertube boiler at full-and part-load using CFD," *Thermal Science and Engineering Progress,* vol. 25, p. 100969, 2021.

[36] R. Laubscher and P. Rousseau, "An enhanced model of particle radiation properties in high ash gas-particle dispersion flow through industrial gas-to-steam heat exchangers," *Fuel,* vol. 285, p. 119153, 2021/02/01/ 2021, doi: https://doi.org/10.1016/j.fuel.2020.119153.

[37] *MicroGen Biomass-/Fossil Fuel-fired Boiler*, John Thompson, ACTOM, 2019. [Online]. Available: https://www.johnthompson.co.za/wp-content/uploads/2019/09/microGen-biomass-fossil-fuel-fired-boiler.pdfhttps://www.johnthompson.co.za/wp-content/uploads/2019/09/microGen-biomass-fossil-fuel-fired-boiler.pdf.

[38] *105t/h Bagasse-/Coal-fired Boiler for Cogeneration*, John Thomson, ACTOM, 2019. [Online]. Available: https://www.johnthompson.co.za/wp-content/uploads/2020/09/case-study-42-105-th-bagasse-coal-fired-boiler-for-cogeneration-jul19.pdf.

[39] G. Sankar, D. S. Kumar, and K. Balasubramanian, "Computational modeling of pulverized coal fired boilers–A review on the current position," *Fuel,* vol. 236, pp. 643-665, 2019.

[40] V. V. Ranade and D. F. Gupta, *Computational modeling of pulverized coal fired boilers*. CRC press, 2014.

Appendix A. Fuel Chemical Equation Derivation

Complete combustion occurs if all carbon in the fuel converts to CO_2, all hydrogen to H_2O, and all sulphur to SO_2, ensuring that all combustible components are fully oxidized. The complete combustion of one mole of each reactant is represented by the following equations:

$$C + O_2 \rightarrow CO_2$$

$$H + \frac{1}{4}O_2 \rightarrow \frac{1}{2}H_2O$$

$$S + O_2 \rightarrow SO_2$$

Some of the nitrogen in the reactants typically forms various NOx compounds in the products. However, for complete combustion, nitrogen is converted to stable diatomic nitrogen in the products (flue gas) as follows:

$$N \rightarrow \frac{1}{2}N_2$$

During complete combustion, any oxygen in the fuel is consumed in the oxidation process and does not appear in the products:

$$O - \frac{1}{2}O_2 \rightarrow 0$$

Let $n_{fC}, n_{fH}, n_{fO}, n_{fN}$ and n_{fS} represent the moles of carbon, hydrogen, oxygen, nitrogen, and sulphur, respectively, in one kilomole (kmol) of fuel. The chemical reactions for complete combustion are as follows:

$$n_{fC} \cdot C + n_{fC} \cdot O_2 \rightarrow n_{fC} \cdot CO_2$$

$$n_{fH} \cdot H + \frac{1}{4}n_{fH} \cdot O_2 \rightarrow \frac{1}{2}n_{fH} \cdot H_2O$$

$$n_{fO} \cdot O - \frac{1}{2}n_{fO} \cdot O_2 \rightarrow n_{fO} \cdot 0$$

$$n_{fN} \cdot N \rightarrow \frac{1}{2}n_{fN} \cdot N_2$$

$$n_{fS} \cdot S + n_{fS} \cdot O_2 \rightarrow n_{fS} \cdot SO_2$$

The mass balance per kmol of fuel is expressed as:

$$C_{n_{fC}}H_{n_{fH}}O_{n_{fO}}N_{n_{fN}}S_{n_{fS}} + \left(n_{fC} + \frac{1}{4}n_{fH} - \frac{1}{2}n_{fO} + n_{fS}\right) \cdot O_2$$

$$\rightarrow n_{fC} \cdot CO_2 + \frac{1}{2} n_{fN} \cdot N_2 + n_{fS} \cdot SO_2 + \frac{1}{2} n_{fH} \cdot H_2O$$

From this equation, the minimum oxygen required for complete combustion, known as stoichiometric or theoretical oxygen, can be derived. This value accounts for the O_2 required for the combustion of carbon, hydrogen, and sulphur, minus the oxygen already present in the fuel:

$$n_{st_{O_2}} = n_{fC} + \frac{1}{4} n_{fH} - \frac{1}{2} n_{fO} + n_{fS}$$

Biomass fuel contains moisture, denoted as M, which remains unreacted and appears as additional H_2O in the products. The moisture balance is shown below:

$$n_{fM} \cdot M \rightarrow n_{fM} \cdot H_2O$$

Dry air used in combustion is approximated as a gas mixture containing 21% oxygen and 79% nitrogen by volume. Therefore, for every mole of oxygen provided by the air, 3.7619 moles of nitrogen are introduced. The moles of nitrogen introduced per kmol of fuel via the stoichiometric oxygen are:

$$n_{st_{N_2}} = 3.7619 \cdot n_{st_{O_2}}$$

The required mass of dry stoichiometric air per kmol of fuel is:

$$m_{st_{dryair}} = \left(n_{st_{O_2}} M_{O_2} + n_{st_{N_2}} M_{N_2} \right) = \left(M_{O_2} + 3.7619 M_{N_2} \right) n_{st_{O_2}}$$

Incomplete combustion occurs if the combustion products contain any unburnt fuel or components such as C, H_2, CO, or OH. Insufficient oxygen can cause incomplete combustion, but it can also occur with more than the theoretical oxygen due to inadequate mixing in the combustion chamber or dissociation at high temperatures. To enhance the likelihood of complete combustion and to control the combustion chamber temperature, more air than the stoichiometric amount is often used. This extra air is called excess air and is usually expressed as a percentage of the stoichiometric air. It is convenient to express excess air as a factor, α, of the stoichiometric air, where α = 1.0 indicates zero excess air (theoretical air), and α = 1.2 indicates 20% excess air. The total moles of O_2 per kmol of fuel in the combustion air are:

$$n_{a_{O_2}} = \alpha \cdot n_{st_{O_2}}$$

The total moles of N_2 per kmol of fuel in the combustion air are:

$$n_{a_{N_2}} = \alpha \cdot n_{st_{N_2}} = 3.7619 \cdot \alpha \cdot n_{st_{O_2}}$$

The total required mass of dry air per kmol of fuel is therefore:

$$m_{dryair} = \left(n_{air_{O_2}} M_{O_2} + n_{air_{N_2}} M_{N_2}\right)$$

$$m_{dryair} = \left(n_{air_{O_2}} + n_{air_{N_2}}\right) M_{air} = (1 + 3.7619)\alpha \cdot n_{st_{O_2}} M_{air} = 4.7619 \cdot \alpha \cdot n_{st_{O_2}} M_{air}$$

The excess air adds additional oxygen and nitrogen to the process, which do not react and leave in the flue gas:

$$(\alpha - 1)(\, n_{st_{O_2}})O_2 \rightarrow (\alpha - 1)(\, n_{st_{O_2}})O_2$$

$$(3.7619\alpha \cdot n_{st_{O_2}})N_2 \rightarrow (3.7619\alpha \cdot n_{st_{O_2}})N_2$$

The overall mass balance, including the excess air, is:

$$\begin{aligned} C_{n_{fC}} H_{n_{fH}} O_{n_{fO}} N_{n_{fN}} S_{n_{fS}} + \left(\alpha \cdot n_{st_{O_2}}\right) \cdot O_2 + \left(3.7619\ \alpha \cdot n_{st_{O_2}}\right) \cdot N_2 \\ \rightarrow n_{fC} \cdot CO_2 + \left(\frac{1}{2} n_{fN} + 3.7619\ \alpha \cdot n_{st_{O_2}}\right) \cdot N_2 + n_{fS} \cdot SO_2 + \left(n_M + \frac{1}{2} n_{fH}\right) \cdot H_2O \\ + (\ \alpha - 1) n_{st_{O_2}} \cdot O_2 \end{aligned}$$

The combustion air typically contains moisture, expressed as specific humidity (w) in kg of moisture per kg of dry air:

$$w = \frac{m_{H_2O}}{m_{dryair}}$$

The mass of water in the combustion air is:

$$m_{H_2O} = w \cdot m_{dryair} = \ w \cdot \left(4.7619 \cdot \alpha \cdot n_{st_{O_2}} M_{air}\right)$$

The moles of water introduced via the combustion air are:

$$n_{air_{H_2O}} = \frac{m_{H_2O}}{M_{H_2O}} = \frac{w \cdot 4.7619 \cdot \alpha \cdot n_{st_{O_2}} M_{air}}{M_{H_2O}}$$

The required total mass of humid combustion air per kmol of fuel is:

$$m_{air} = n_{air_{O_2}} M_{O_2} + n_{air_{N_2}} M_{N_2} + n_{air_{H_2O}} M_{H_2O}$$

$$m_{air} = (M_{O_2} + 3.7619 M_{N_2} + 4.7619 w M_{air}) \frac{\alpha \cdot n_{st_{O_2}}}{M_{H_2O}}$$

The additional water that enters the process via the combustion air also leaves in the flue gas:

$$(4.7619 \alpha w \frac{M_{air}}{M_{H_2O}} n_{st_{O_2}}) H_2O \rightarrow (4.7619 \alpha w \frac{M_{air}}{M_{H_2O}} n_{st_{O_2}}) H_2O$$

The overall mass balance, including theoretical and excess air, as well as moisture from combustion air, is:

$$C_{n_{fC}} H_{n_{fH}} O_{n_{fO}} N_{n_{fN}} S_{n_{fS}} + \left(4.7619\ \alpha w \frac{M_{air}}{M_{H_2O}} n_{st_{O_2}}\right) \cdot H_2O + \left(\alpha \cdot n_{st_{O_2}}\right) \cdot O_2 + \left(3.7619\ \alpha \cdot n_{st_{O_2}}\right) \cdot N_2$$
$$\rightarrow n_{fC} \cdot CO_2 + \left(\frac{1}{2} n_{fN} + 3.7619\ \alpha \cdot n_{st_{O_2}}\right) \cdot N_2 + n_{fS} \cdot SO_2$$
$$+ \left(n_M + \frac{1}{2} n_{fH} + 4.7619\ \alpha w \frac{M_{air}}{M_{H_2O}} n_{st_{O_2}}\right) \cdot H_2O + (\alpha - 1) n_{st_{O_2}} \cdot O_2$$

The reactants now include the additional moisture introduced via the combustion air (theoretical and excess air). The products include the moisture in the fuel, the water formed during the oxidation of hydrogen, and the additional moisture from the combustion air (theoretical and excess air). The generic chemical equation for the combustion of fuel with excess humid air can be simplified as shown below:

$$C_{n_{fC}} H_{n_{fH}} O_{n_{fO}} N_{n_{fN}} S_{n_{fS}} M_{n_{fM}} + n_{r_{H_2O}} \cdot H_2O + n_{r_{O_2}} \cdot O_2 + n_{r_{N_2}} \cdot N_2$$
$$\rightarrow n_{p_{CO_2}} \cdot CO_2 + n_{p_{N_2}} \cdot N_2 + n_{p_{SO_2}} \cdot SO_2 + n_{p_{H_2O}} \cdot H_2O + n_{p_{O_2}} \cdot O_2$$

Appendix B. Projected Method Derivation

The total net radiative heat flux, which denotes the heat absorbed by the furnace and at the furnace exit plane, is represented by the following equation:

$$Q_{rad} = \psi \varepsilon_{fur} A_{rad} ({T_{fg}}^4 - T_w^4)$$

The net radiative heat exchange with the wall must equal the loss of enthalpy of the flue gas. This enthalpy loss can be expressed as:

$$\dot{Q}_{fg_{fur}} = \varphi \dot{m}_f \overline{VC} (T_{fg_{aft}} - T_{fg_{fe}})$$

By equating the two equations, we get:

$$\varphi \dot{m}_f \overline{VC} \left(T_{fg_{aft}} - T_{fg_{fe}}\right) = \psi \varepsilon_{fur} A_{rad} ({T_{fg}}^4 - T_w^4)$$

The average temperature will lie somewhere between $T_{fg_{aft}}$ and $T_{fg_{fe}}$; however, its precise value is difficult to determine. To simplify this equation, we introduce non-dimensional temperatures:

$$\theta_{fg_{fe}} = \frac{T_{fg_{fe}}}{T_{fg_{aft}}}, \ \theta_{fg} = \frac{T_{fg}}{T_{fg_{aft}}}, \theta_w = \frac{T_w}{T_{fg_{aft}}}.$$

By dividing the equation by $T_{fg_{aft}}$ and introducing the non-dimensional terms, we get:

$$1 - \theta_{fg_{fe}} = \frac{\varepsilon_{furn} C ({\theta_{fg}}^4 - {\theta_w}^4)}{B_o}$$

where C is an empirical constant and B_o is the Boltzmann number, defined as:

$$B_o = \frac{\varphi \dot{m}_f \overline{VC}}{\sigma_o \psi A_{rad} {T_{fg_{aft}}}^3}.$$

Experimental observations and theoretical reasoning suggest that the furnace exit temperature increases with an increase in the furnace temperature. Based on empirical data, an empirical coefficient is used to relate $T_{fg_{aft}}, T_{fg}$ and $T_{fg_{fe}}$:

$$\theta_{fg} \alpha \ {\theta_{fg_{fe}}}^n$$

where n is an empirical correlation. Given that T_w is much smaller compared to T_{fg}, we can approximate:

$$\theta_{fg,mean} \gg \theta_w$$

$${\theta_{fg}}^4 - {\theta_w}^4 \approx {\theta_{fg}}^4$$

Thus, the equation simplifies to:

$$1 - \theta_{fg_{fe}} = \frac{\varepsilon_{fur} C ({\theta_{fg_{fe}}}^{4n})}{B_o}$$

The empirical coefficients C and n depend on the properties of the fuel fired, the combustion conditions, the furnace design, and the heat-absorbing surfaces. These coefficients can be obtained from experimental data from studies by Gurvich and Blokh. Simplifying the equation further, we get:

$$\theta_{fg_{fe}} = \frac{T_{fg_{fe}}}{T_{fg_{aft}}} = \frac{{B_o}^{0.6}}{M \cdot {\varepsilon_{fur}}^{0.6} + {B_o}^{0.6}}$$

Therefore:

$$\frac{T_{fg_{fe}}}{T_{fg_{aft}}} = \frac{1}{M \left(\frac{\sigma_o \psi_{eff} A_{rad} \varepsilon_{fur} {T_{fg_{aft}}}^3}{\varphi \dot{m}_f \overline{VC}} \right) + 1}$$

where M is the flame modification factor.

Appendix C. Direct Method Derivation

The emissive power of a blackbody (E_b) is described by the Stefan-Boltzmann law:

$$E_b = \sigma_o T^4 \left[\frac{W}{m^2}\right]$$

where σ_o is the Stefan-Boltzmann constant (approximated 5.67 x 10^{-8} W/m^{2}K^4) and T is the absolute temperature in Kelvin. For any real surface, the emissive power is less than that of a blackbody due to its emissivity (ε). Emissivity is defined as the ratio of the actual radiation emitted by a surface to the radiation emitted by a blackbody at the same temperature. Emissivity values range between 0 and 1. The emissive power of a real surface, E_ε, can be determined by multiplying the blackbody emissive power by the emissivity of the surface:

$$E_\varepsilon = \varepsilon E_b = \varepsilon \sigma_o T^4$$

Since a real surface both absorbs and reflects radiation, the relationship among emissivity, absorptivity ($\propto$), and reflectivity (ρ) is given by:

$$\varepsilon + \propto + \rho = 1$$

The radiation absorbed by a body, characterised by absorptivity, can be calculated as:

$$E_\propto = \alpha E_b = \alpha \sigma_o T^4$$

In the context of a furnace with a medium (gas) and waterwall, the radiation emitted by the medium ($\dot{Q}_g$) and the waterwall ($\dot{Q}_w$) can be expressed as:

$$\dot{Q}_g = \varepsilon_g \sigma_o T_g^4 A_{rad}$$

$$\dot{Q}_w = \varepsilon_w \sigma_o T_w^4 A_{rad}$$

where T_g and T_w are the temperatures of the medium and the waterwall, respectively, and A_{rad} is the radiating area. The radiation projected onto the waterwall from the medium ($\dot{Q}_{em_g}$) includes the radiation from the medium ($\dot{Q}_g$) and the reflected radiation from the waterwall ($\dot{Q}_{em_w}(1 - \alpha_g)$):

$$\dot{Q}_{\varepsilon_g} = \dot{Q}_g + \dot{Q}_{\varepsilon_w}(1 - \alpha_g) = \varepsilon_g \sigma_o T_g^4 A_{rad} + \dot{Q}_{\varepsilon_w}(1 - \alpha_g)$$

The reflected radiation of the waterwall back to the medium $\left(\dot{Q}_{\rho_w}\right)$ is therefore:

$$\dot{Q}_{\rho_w} = (1 - \alpha_w)\dot{Q}_{em_g}$$

Substituting $\dot{Q}_{em_g}$ into the equation for $\dot{Q}_{ref_w}$, we get:

$$\dot{Q}_{\rho_w} = (1 - \alpha_w)\left[\varepsilon_g \sigma_o T_g^4 A_{rad} - \dot{Q}_{em_w}(1 - \alpha_g)\right]$$

Thus, the radiosity equation for the waterwall becomes:

$$\dot{Q}_{em_w} = \dot{Q}_w + \dot{Q}_{ref_w} = \varepsilon_w \sigma_o T_w^4 A_{rad} + (1-\alpha_w)\left[\varepsilon_g \sigma_o T_g^4 A_{rad} - \dot{Q}_{em_w}(1-\alpha_g)\right]$$

Solving for $\dot{Q}_{em_w}$ yields:

$$\dot{Q}_{em_w} = \frac{\varepsilon_w T_w^4 + \varepsilon_g(1-\alpha_w)T_g^4}{1-(1-\alpha_w)(1-\alpha_g)}\sigma_o A_{rad}$$

Considering the heat transfer, the radiative heat loss from the medium ($\dot{Q}_{rad}$) is:

$$\dot{Q}_{rad} = \dot{Q}_g - \alpha_g \dot{Q}_{em_w} = \varepsilon_g \sigma_o T_g^4 A_{rad} - \alpha_g \frac{\varepsilon_w T_w^4 + \varepsilon_g(1-\alpha_w)T_g^4}{1-(1-\alpha_w)(1-\alpha_g)}\sigma_o A_{rad}$$

Substituting $\dot{Q}_g$ and $\dot{Q}_{em_w}$:

$$\dot{Q}_{rad} = \varepsilon_g \sigma_o T_g^4 A_{rad} - \alpha_g \frac{\varepsilon_w T_w^4 + \varepsilon_g(1-\alpha_w)T_g^4}{1-(1-\alpha_w)(1-\alpha_g)}\sigma_o A_{rad}$$

Simplified, this equation becomes:

$$\dot{Q}_{rad} = \frac{\frac{\varepsilon_g}{\alpha_g}T_g^4 + \frac{\varepsilon_w}{\alpha_w}T_w^4}{\frac{1}{\alpha_w}+\frac{1}{\alpha_g}-1}\sigma_o A_{rad}$$

Assuming the heating surface is a graybody ($\alpha_w = \varepsilon_w$), the equation further simplifies to:

$$\dot{Q}_{rad} = \frac{\varepsilon_w}{\propto_g + \varepsilon_w - \propto_g \varepsilon_w}\sigma_o A_{rad}\left(\varepsilon_g T_{fg}^4 - \propto_g T_w^4\right)$$

The projected method is derived assuming both the heating surface and the medium are graybodies ($\alpha_w = \varepsilon_w$ and $\alpha_g = \varepsilon_g$). The equation for radiative heat transfer for the projected method simplifies to:

$$\dot{Q}_{rad} = \frac{1}{\frac{1}{\varepsilon_g}+\frac{1}{\varepsilon_w}-1}\sigma_o A_{rad}\left(T_{fg}^4 - T_w^4\right)$$

Here, $\frac{1}{\frac{1}{\varepsilon_g}+\frac{1}{\varepsilon_w}-1}$ represents the furnace emissivity $\left(\varepsilon_{furn}\right)$. The actual furnace emissivity ε_{furn} is different from the one above due to fouling and furnace view factors. From above, we know the net radiation leaving the furnace wall ($\dot{Q}_{em_w}$) is given by:

$$\dot{Q}_{em_w} = \dot{Q}_w + (1-\alpha_w)\dot{Q}_{em_g}$$

Considering both the medium and water wall as graybodies, the emissivity equations for the medium and waterwall simplify to:

$$\dot{Q}_{em_g} = \varepsilon_g \sigma_o T_g^4 A_{rad} + (1 - \varepsilon_g)\dot{Q}_{em_w}$$

$$\dot{Q}_{em_w} = \varepsilon_w \sigma_o T_w^4 A_{rad} + (1 - \varepsilon_w)\dot{Q}_{em_g}$$

Utilising the furnace emissivity, the net radiation from the flame can be expressed as:

$$\dot{Q}_{em_g} = \varepsilon_{furn} \sigma_o {T_g}^4 A_{rad}$$

Therefore, we can therefore simplify $\dot{Q}_{em_w}$ to:

$$\dot{Q}_{em_w} = \varepsilon_w \sigma_o T_w^4 A_{rad} + (1 - \varepsilon_w)\varepsilon_{furn} \sigma_o {T_g}^4 A_{rad}$$

The furnace efficiency factor (ψ) is defined as:

$$\psi = \frac{\dot{Q}_{em_g} - \dot{Q}_{em_w}}{\dot{Q}_{em_g}}$$

$$\psi = \frac{\varepsilon_{furn} \sigma_o {T_g}^4 - \varepsilon_w \sigma_o {T_w}^4 + (1 - \varepsilon_w)\varepsilon_{furn} \sigma_o {T_g}^4}{\varepsilon_{furn} \sigma_o {T_g}^4}$$

Dividing throughout by ${T_g}^4$ and cancelling out σ_o, we get:

$$\psi = \frac{\varepsilon_{furn} - \frac{{T_w}^4}{{T_g}^4}\varepsilon_w + (1 - \varepsilon_w)\varepsilon_{furn}}{\varepsilon_{furn}}$$

Solving for $\frac{{T_w}^4}{{T_g}^4}$:

$$\frac{{T_w}^4}{{T_g}^4} = \varepsilon_{furn}\left(1 - \frac{\psi}{\varepsilon_w}\right)$$

Finally, solving the two equations above for ε_{furn}, we get:

$$\varepsilon_{furn} = \frac{\varepsilon_g}{\varepsilon_g + (1 - \varepsilon_g)\psi}$$

Therefore, for the projected method, which assumes that T_w is much smaller compared to T_g, the radiation heat transfer in the furnace becomes:

$$\dot{Q}_{rad} = \varepsilon_{furn} \sigma_o A_{rad} T_g^4$$

These equations provide a comprehensive framework for deriving radiation heat transfer equations for both the direct and the projected method, accounting for the complexities of real surfaces and the interactions within a furnace system.

Appendix D. Energy Input to the Furnace

D.1 Case Study 1

Table D-1.1: *CFD vs. 0-D models (Case Study 1 – 36 t/h) – Comparison of furnace energy inflow [kW].*

Description	$\dot{Q}_{ca}$	$\dot{Q}_{fuel_s}$	$\dot{Q}_{react}$	$\dot{Q}_{UC}$	Sum
CFD	3,506	11	39,828	-609	42,736
0-D	3,477	11	39,828	-609	42,706
Relative error	*-0.8%*	*0%*	*0%*	*0%*	*-0.1%*

Table D-1.2: *CFD vs. 0-D models (Case Study 1 – 27 t/h) – Comparison of furnace energy inflow [kW].*

Description	$\dot{Q}_{ca}$	$\dot{Q}_{fuel_s}$	$\dot{Q}_{react}$	$\dot{Q}_{UC}$	Sum
CFD	2,634	8	30,167	-665	32,144
0-D	2,609	8	30,167	-665	32,119
Relative error	*-0.9%*	*0.0%*	*0.0%*	*0.0%*	*-0.1%*

D.2 Case Study 2

Table D-2.1: *CFD vs. 0-D models (Case Study 2 – 80 t/h) – Comparison of furnace energy inflow [kW].*

Description	$\dot{Q}_{ca}$	$\dot{Q}_{fuel_s}$	$\dot{Q}_{react}$	$\dot{Q}_{UC}$	Sum
CFD	7,270	25	93,936	-1,597	99,634
0-D	7,318	25	93,936	-1,597	99,683
Relative error	*0.7%*	*0.0%*	*0.0%*	*0.0%*	*0.0%*

Table D-2.2: *CFD vs. 0-D models (Case Study 2 – 65 t/h) – Comparison of furnace energy inflow [kW].*

Description	$\dot{Q}_{ca}$	$\dot{Q}_{fuel_s}$	$\dot{Q}_{react}$	$\dot{Q}_{UC}$	Sum
CFD	5,720	20	74,406	-1,530	78,712
0-D	5,792	20	74,406	-1,530	78,787
Relative error	*1.3%*	*0.0%*	*0.0%*	*0.0%*	*0.1%*

Appendix E. Energy Distribution Analysis

E.1 Case Study 1

Table E-1: *Percentage contribution of* $\dot{Q}_{ww}$ and $\dot{Q}_{fg_{fe}}$ to the total heat.

Description		$\dot{Q}_{ww}$	**%**	$\dot{Q}_{fg_{fe}}$	**%**
45 t/h	**CFD**	13.9	*25.9%*	37.3	*69.6%*
	P1	11.1	*20.8%*	39.7	*74.3%*
	D1	10.2	*19.1%*	41.9	*78.5%*
36 t/h	**CFD**	12.5	*29.3%*	28.2	*66.1%*
	P1	9.8	*23.0%*	30.6	*71.6%*
	D1	9.1	*21.3%*	32.5	*76.2%*
27 t/h	**CFD**	10.9	*33.9%*	20.2	*62.4%*
	P1	8.3	*25.9%*	21.9	*68.2%*
	D1	7.8	*24.1%*	23.5	*73.3%*

Full load (45 t/h)

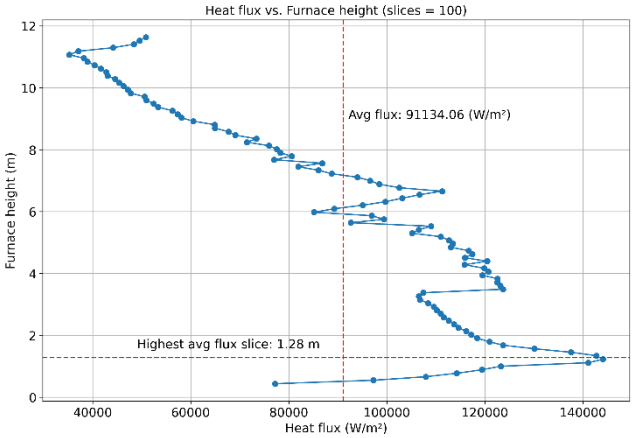

***Figure E1.1**: Waterwall furnace heat flux along the furnace height.*

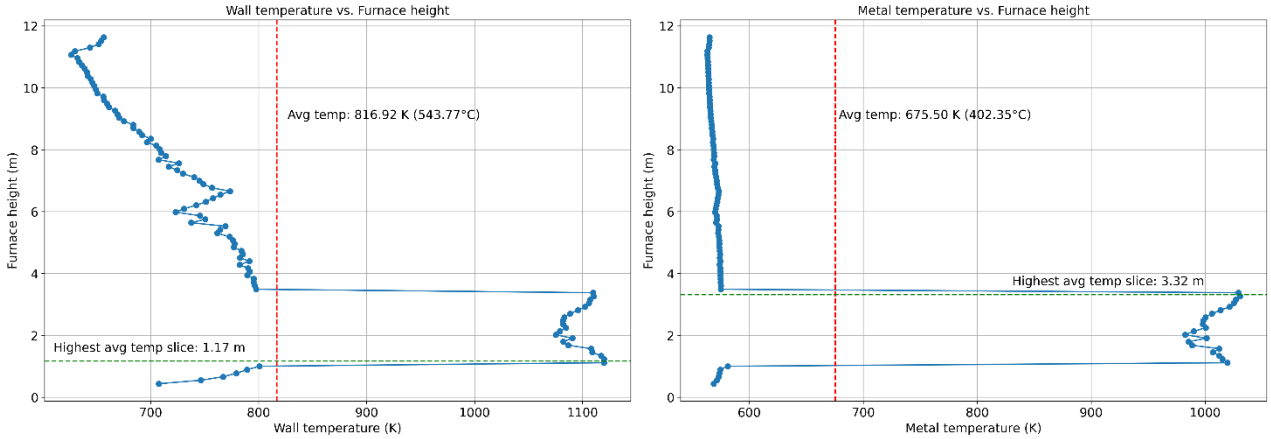

***Figure E1.2:** Wall temperature (left) and metal temperature (right) along the furnace height.*

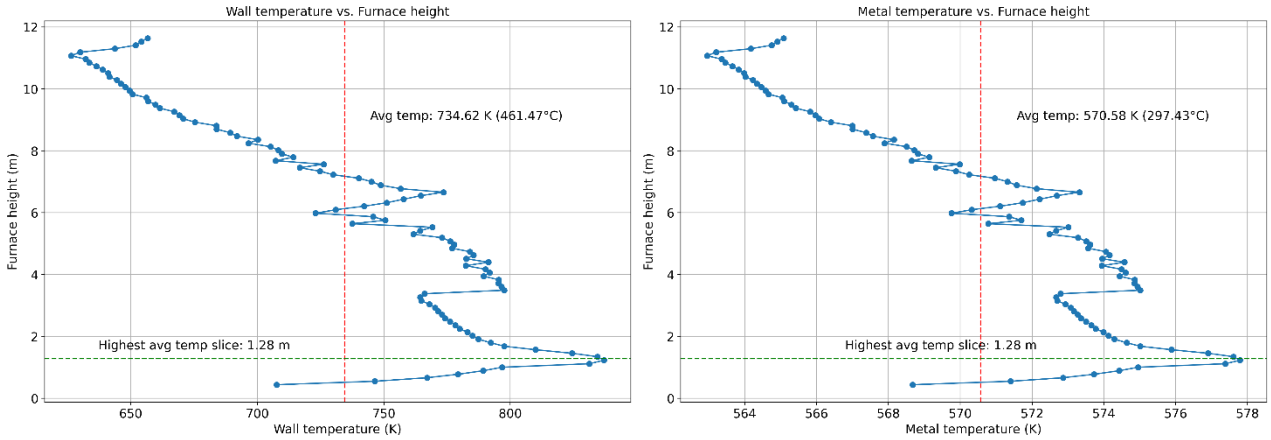

***Figure E1.3:** Waterwall wall temperature (left) and metal temperature (right) along the furnace height.*

Reduced load – 36 t/h

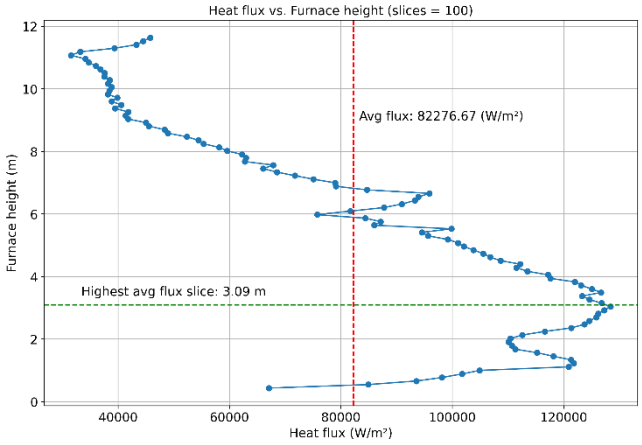

Figure E1.4: *Waterwall furnace heat flux along the furnace height.*

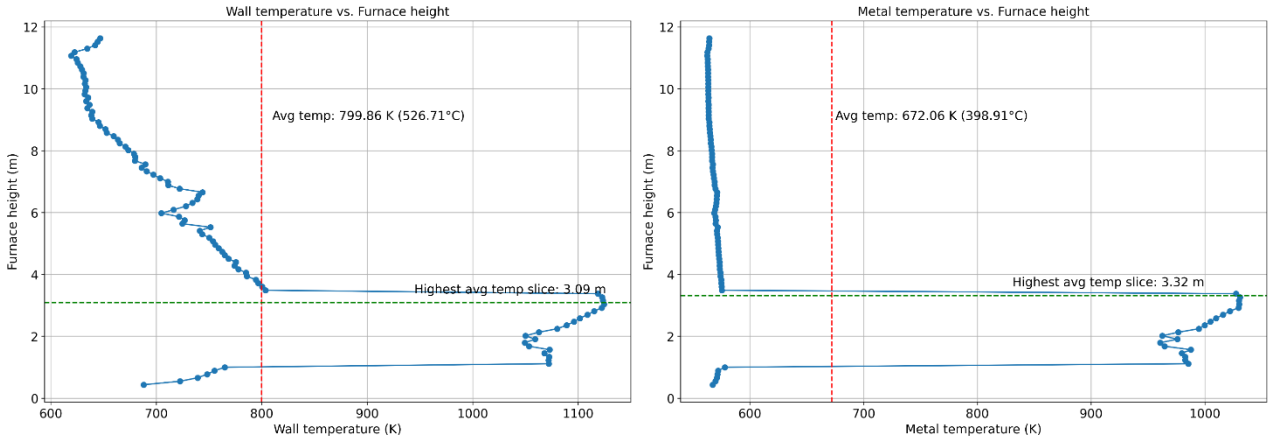

Figure E1.5: *Wall temperature (left) and metal temperature (right) along the furnace height.*

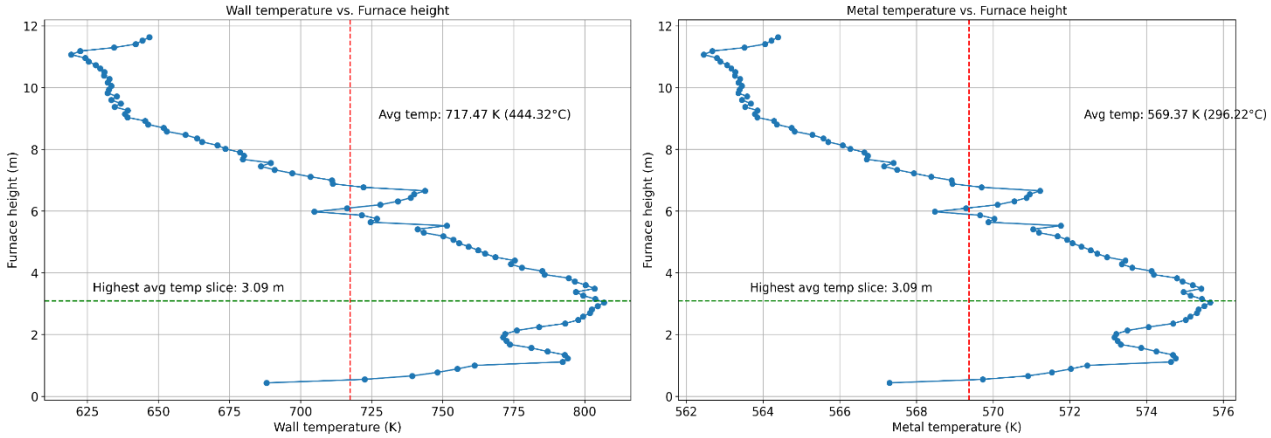

Figure E1.6: *Waterwall wall temperature (left) and metal temperature (right) along the furnace height.*

Reduced load – 27 t/h

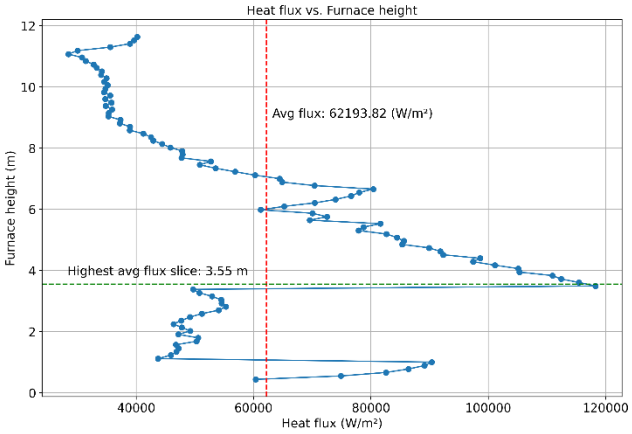

Figure E1.9: *Wall furnace heat flux along the furnace height.*

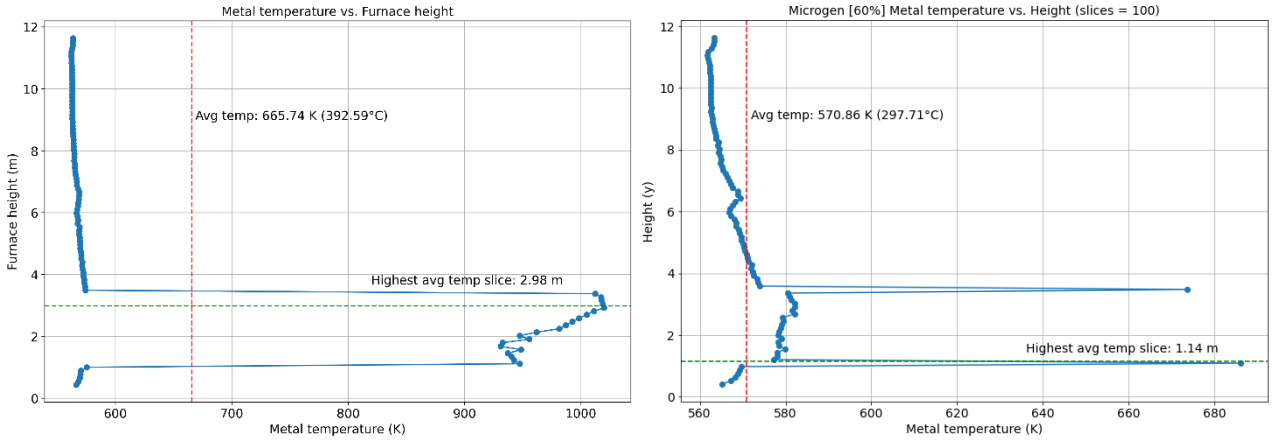

Figure E1.10: *Wall metal temperature (left) and waterwall metal temperature (right) along the furnace height.*

E.2 Case Study 2

Table E.2: *Percentage contribution of* $\dot{Q}_{ww}$ and $\dot{Q}_{fg_{fe}}$ to the total heat.

Description		$\dot{Q}_{ww}$	**%**	$\dot{Q}_{fg_{fe}}$	**%**
100 t/h	**CFD**	27.8	*22.3%*	90.4	*72.1%*
	P1	29.5	*23.7%*	89.9	*72.1%*
	P2	31.3	*25.2%*	87.7	*70.3%*
	D1	26.4	*21.2%*	95.7	*76.5%*
	D2	28.7	*23.0%*	93.1	*74.6%*
80 t/h	**CFD**	24.1	*24.2%*	69.4	*69.9%*
	P1	25.5	*25.7%*	69.6	*69.8%*
	P2	27.1	*27.2%*	67.8	*68.0%*
	D1	22.8	*22.9%*	74.1	*74.4%*
	D2	24.6	*24.7%*	72.1	*72.4%*
65 t/h	**CFD**	21.1	*26.8%*	51.6	*65.6%*
	P1	22.2	*28.3%*	52.5	*66.8%*
	P2	23.5	*29.9%*	51.1	*64.9%*
	D1	20.1	*25.6%*	56.7	*72.0%*
	D2	21.6	*27.5%*	55.1	*70.1*

Full load – 100 t/h

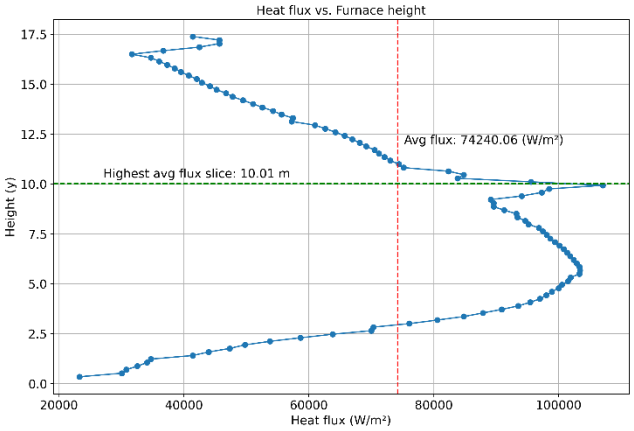

Figure E2.1: *Waterwall furnace heat flux along the furnace height.*

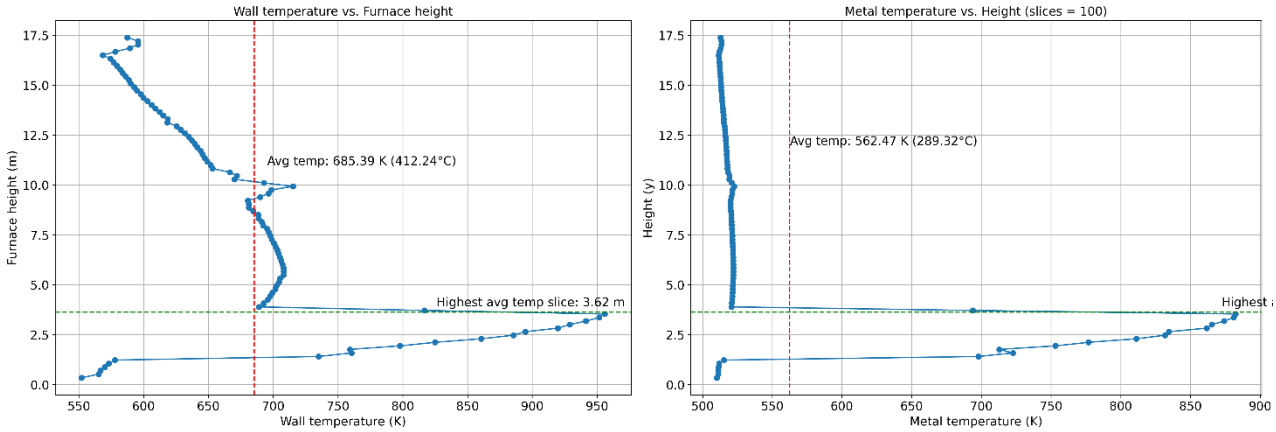

Figure E2.2: *Wall temperature (left) and metal temperature (right) along the furnace height.*

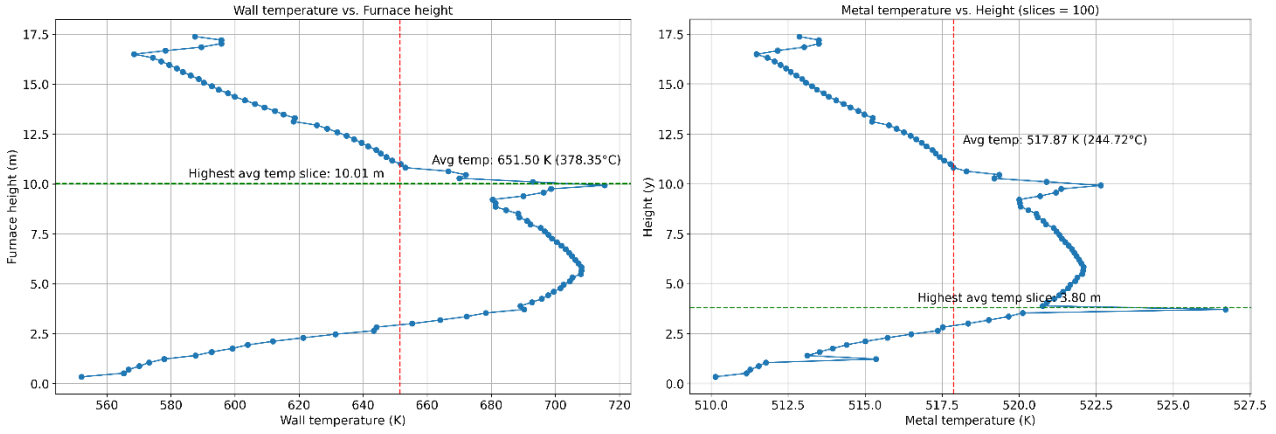

Figure E2.3: *Waterwall temperature (left) and metal temperature (right) along the furnace height.*

Reduced load – 80 t/h

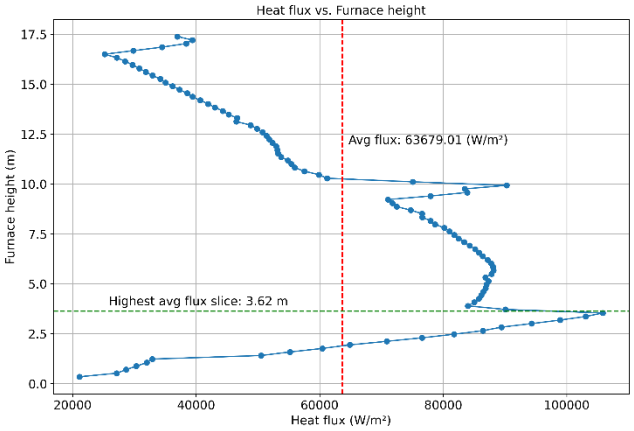

Figure E2.4: *Waterwall furnace heat flux along the furnace height.*

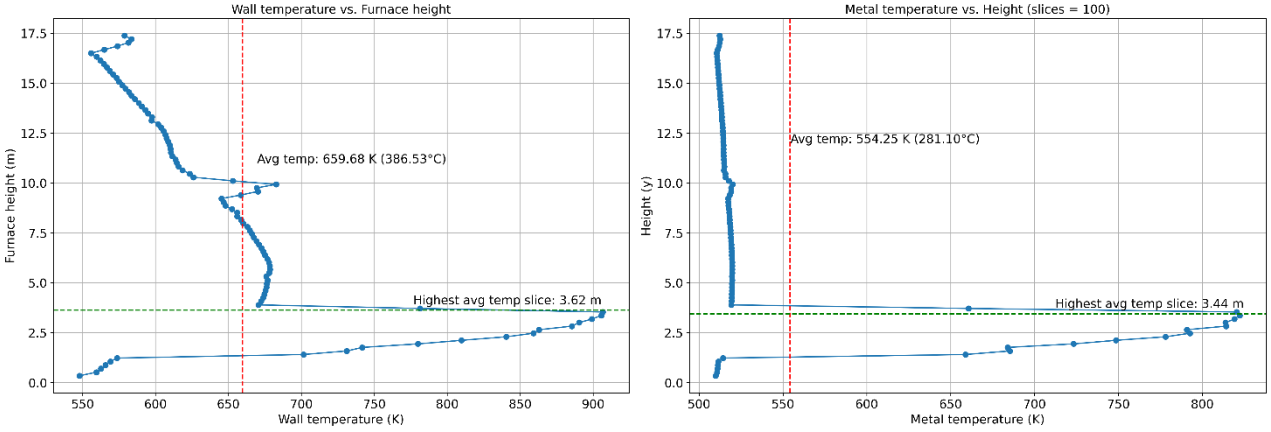

Figure E2.5: *Wall temperature (left) and metal temperature (right) along the furnace height.*

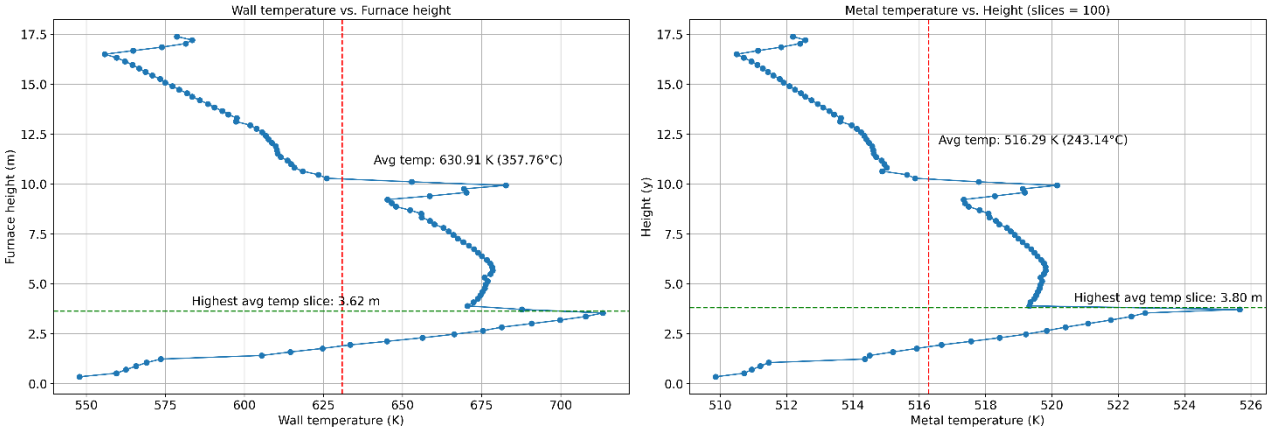

Figure E2.6: *Waterwall temperature (left) and metal temperature (right) along the furnace height.*

Reduced load – 65 t/h

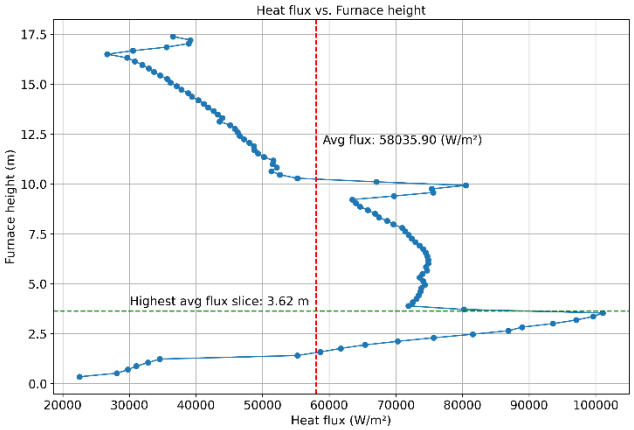

Figure E2.7: *Waterwall furnace heat flux along the furnace height.*

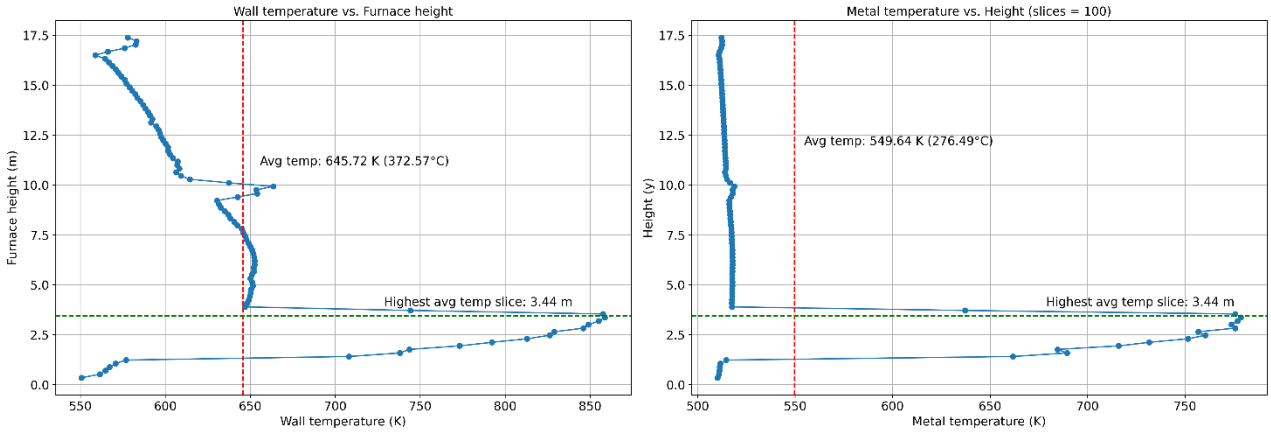

Figure E2.8: *Wall temperature (left) and metal temperature (right) along the furnace height.*

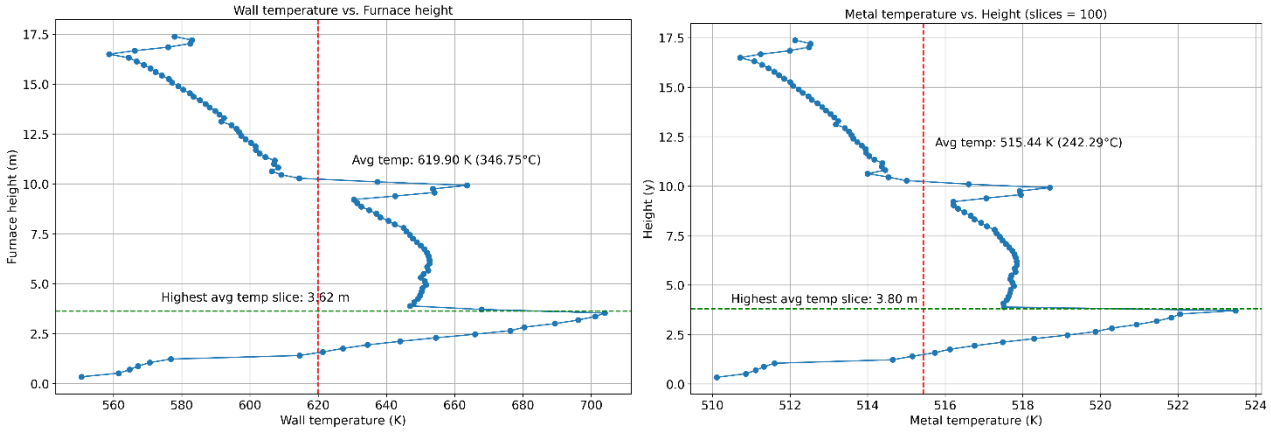

Figure E2.9: *Waterwall temperature (left) and metal temperature (right) along the furnace height.*

Appendix F. Sensitivity Analysis

F.1 Projected Method

Table F-1.1: *Case Study 1 (45 t/h) – Projected method sensitivity at 1% perturbation.*

45 t/h Sensitivity - 1%				Outputs							
				T_fe	h_fg_fe	T_g	Q_dot_fur	Q_dot_ww	Q_dot_rf	Q_dot_fe	Q_dot_fg_fe
	Parameter	Value	Unit	K	kJ/kgK	K	kW	kW	kW	kW	kW
1	eta_fe	0.80		0.0%	0.0%	0.0%	0.0%	-1.3%	0.0%	18.9%	0.0%
2	beta_fe	1.00		0.0%	0.0%	0.0%	0.0%	-0.8%	0.0%	12.1%	0.0%
3	epsilon_g	0.43		-21.0%	-21.0%	-31.8%	21.0%	18.3%	0.7%	8.4%	-21.0%
4	eta_rf	0.64		0.0%	0.0%	0.0%	0.0%	0.0%	2.3%	0.0%	0.0%
5	xi_fur_ww	0.60	m^2K/W	-3.8%	-3.8%	-5.7%	3.8%	9.8%	-0.9%	-11.0%	-3.8%
6	xi_fur_rf	0.10	m^2K/W	-0.1%	-0.1%	-0.2%	0.1%	-0.1%	92.7%	-0.4%	-0.1%
7	xi_fur_fe	1.00	m^2K/W	-0.1%	-0.1%	-0.1%	0.1%	-0.2%	0.0%	9.0%	-0.1%
8	x_fur_ww	0.92		-4.8%	-4.8%	-7.3%	4.8%	8.5%	-0.2%	-2.5%	-4.8%
9	x_fur_rf	1.00		0.0%	0.0%	-0.1%	0.0%	0.0%	1.0%	0.0%	0.0%
10	x_fur_fe	1.00		-0.2%	-0.2%	-0.2%	0.2%	-0.1%	0.0%	9.5%	-0.2%
11	d_fa	20.00	µm	0.0%	0.0%	0.0%	0.0%	0.0%	0.0%	0.0%	0.0%
12	M_flame	0.52		-70.0%	-70.0%	54.5%	70.0%	60.7%	2.2%	28.1%	-70.0%
13	cp_ash	1200.00	J/kg K	0.0%	0.0%	0.0%	0.0%	0.0%	0.0%	0.0%	0.0%
				100.0%	100.0%	100.0%	100.0%	100.0%	100.0%	100.0%	100.0%

Table F-1.2: *Case Study 1 (45 t/h) – Projected method sensitivity at 2% perturbation.*

45 t/h Sensitivity - 2%											
	Parameter	Value	Unit	T_fe	h_fg_fe	T_g	Q_dot_fur	Q_dot_ww	Q_dot_rf	Q_dot_fe	Q_dot_fg_fe
				K	kJ/kgK	K	kW	kW	kW	kW	kW
1	eta_fe	0.80		0.0%	0.0%	0.0%	0.0%	-1.3%	0.0%	19.0%	0.0%
2	beta_fe	1.00		0.0%	0.0%	0.0%	0.0%	-0.8%	0.0%	12.2%	0.0%
3	epsilon_g	0.43		-20.9%	-20.9%	-31.8%	20.9%	18.2%	0.7%	8.4%	-20.9%
4	eta_rf	0.64		0.0%	0.0%	0.0%	0.0%	0.0%	2.3%	0.0%	0.0%
5	xi_fur_ww	0.60		-3.8%	-3.8%	-5.7%	3.8%	9.8%	-0.9%	-10.9%	-3.8%
6	xi_fur_rf	0.10		-0.1%	-0.1%	-0.2%	0.1%	-0.1%	92.7%	-0.4%	-0.1%
7	xi_fur_fe	1.00		-0.1%	-0.1%	-0.1%	0.1%	-0.2%	0.0%	9.0%	-0.1%
8	x_fur_ww	0.92		-4.8%	-4.8%	-7.3%	4.8%	8.5%	-0.2%	-2.5%	-4.8%
9	x_fur_rf	1.00		0.0%	0.0%	-0.1%	0.0%	0.0%	1.0%	0.0%	0.0%
10	x_fur_fe	1.00		-0.2%	-0.2%	-0.2%	0.2%	-0.1%	0.0%	9.5%	-0.2%
11	d_fa	20.00	um	0.0%	0.0%	0.0%	0.0%	0.0%	0.0%	0.0%	0.0%
12	M_flame	0.52		-70.1%	-70.0%	54.5%	70.0%	60.8%	2.2%	28.1%	-70.0%
13	cp_ash	1200.00	J/kg K	0.0%	0.0%	0.0%	0.0%	0.0%	0.0%	0.0%	0.0%
				100.0%	100.0%	100.0%	100.0%	100.0%	100.0%	100.0%	100.0%

Table F-1.3: *Case Study 1 (36 t/h) – Projected method sensitivity at 1% perturbation.*

36 t/h Sensitivity - 1%											
	Parameter	Value	Unit	T_fe	h_fg_fe	T_g	Q_dot_fur	Q_dot_ww	Q_dot_rf	Q_dot_fe	Q_dot_fg_fe
				K	kJ/kgK	K	kW	kW	kW	kW	kW
1	eta_fe	0.80		0.0%	0.0%	0.0%	0.0%	-1.4%	0.0%	19.5%	0.0%
2	beta_fe	1.00		0.0%	0.0%	0.0%	0.0%	-0.9%	0.0%	12.5%	0.0%
3	epsilon_g	0.43		-20.4%	-20.5%	-33.9%	20.5%	17.6%	0.6%	7.8%	-20.5%
4	eta_rf	0.64		0.0%	0.0%	0.0%	0.0%	0.0%	2.4%	0.0%	0.0%
5	xi_fur_ww	0.60	m^2K/W	-3.9%	-3.9%	-6.4%	3.9%	10.2%	-0.9%	-11.4%	-3.9%
6	xi_fur_rf	0.10	m^2K/W	-0.1%	-0.1%	-0.2%	0.1%	-0.2%	92.9%	-0.4%	-0.1%
7	xi_fur_fe	1.00	m^2K/W	-0.1%	-0.1%	-0.1%	0.1%	-0.2%	0.0%	9.2%	-0.1%
8	x_fur_ww	0.92		-4.9%	-4.9%	-8.0%	4.9%	8.7%	-0.2%	-2.7%	-4.9%
9	x_fur_rf	1.00		0.0%	0.0%	-0.1%	0.0%	0.0%	1.0%	0.0%	0.0%
10	x_fur_fe	1.00		-0.2%	-0.2%	-0.3%	0.2%	-0.1%	0.0%	9.7%	-0.2%
11	d_fa	20.00	µm	0.0%	0.0%	0.0%	0.0%	0.0%	0.0%	0.0%	0.0%
12	M_flame	0.52		-70.4%	-70.4%	51.0%	70.4%	60.6%	2.1%	26.8%	-70.4%
13	cp_ash	1200.00	J/kg K	0.0%	0.0%	0.0%	0.0%	0.0%	0.0%	0.0%	0.0%
				100.0%	100.0%	100.0%	100.0%	100.0%	100.0%	100.0%	100.0%

Table F-1.4: *Case Study 1 (27 t/h) – Projected method sensitivity at 1% perturbation.*

27 t/h Sensitivity - 1%											
	Parameter	Value	Unit	T_fe	h_fg_fe	T_g	Q_dot_fur	Q_dot_ww	Q_dot_rf	Q_dot_fe	Q_dot_fg_fe
				K	kJ/kgK	K	kW	kW	kW	kW	kW
1	eta_fe	0.80		0.0%	0.0%	0.0%	0.0%	-1.5%	0.0%	20.0%	0.0%
2	beta_fe	1.00		0.0%	0.0%	0.0%	0.0%	-1.0%	0.0%	12.8%	0.0%
3	epsilon_g	0.44		-20.4%	-20.4%	-37.4%	20.4%	17.4%	0.5%	7.2%	-20.4%
4	eta_rf	0.64		0.0%	0.0%	0.0%	0.0%	0.0%	2.4%	0.0%	0.0%
5	xi_fur_ww	0.60		-3.9%	-3.9%	-7.1%	3.9%	10.6%	-0.9%	-12.2%	-3.9%
6	xi_fur_rf	0.10		-0.1%	-0.1%	-0.3%	0.1%	-0.2%	93.0%	-0.5%	-0.1%
7	xi_fur_fe	1.00		-0.1%	-0.1%	-0.1%	0.1%	-0.3%	0.0%	9.4%	-0.1%
8	x_fur_ww	0.92		-4.9%	-4.9%	-8.9%	4.9%	8.9%	-0.2%	-3.0%	-4.9%
9	x_fur_rf	1.00		0.0%	0.0%	-0.1%	0.0%	0.0%	1.0%	0.0%	0.0%
10	x_fur_fe	1.00		-0.2%	-0.2%	-0.3%	0.2%	-0.2%	0.0%	9.9%	-0.2%
11	d_fa	20.00	um	0.0%	0.0%	0.0%	0.0%	0.0%	0.0%	0.0%	0.0%
12	M_flame	0.52		-70.4%	-70.4%	45.8%	70.4%	60.0%	1.9%	25.0%	-70.4%
13	cp_ash	1200.00	J/kg K	0.0%	0.0%	0.0%	0.0%	0.0%	0.0%	0.0%	0.0%
				100.0%	100.0%	100.0%	100.0%	100.0%	100.0%	100.0%	100.0%

Table F-1.5: *Case Study 2 (100 t/h) – Projected method sensitivity at 1% perturbation.*

100 t/h Sensitivity - 1%				Outputs							
				T_fe	h_fg_fe	T_g	Q_dot_fur	Q_dot_ww	Q_dot_rf	Q_dot_fe	Q_dot_fg_fe
	Parameter	Value	Unit	K	kJ/kgK	K	kW	kW	kW	kW	kW
1	eta_fe	0.80		0.0%	0.0%	0.0%	0.0%	-0.9%	0.0%	19.5%	0.0%
2	beta_fe	1.00		0.0%	0.0%	0.0%	0.0%	-0.6%	0.0%	12.5%	0.0%
3	epsilon_g	0.51		-15.5%	-15.5%	-26.4%	15.5%	13.6%	0.4%	5.8%	-15.5%
4	eta_rf	0.64		0.0%	0.0%	0.0%	0.0%	0.0%	2.3%	0.0%	0.0%
5	xi_fur_ww	0.60		-5.4%	-5.4%	-9.3%	5.4%	11.0%	-0.9%	-11.9%	-5.4%
6	xi_fur_rf	0.10		0.0%	0.0%	-0.1%	0.0%	0.0%	93.1%	-0.1%	0.0%
7	xi_fur_fe	1.00		-0.1%	-0.1%	-0.1%	0.1%	-0.2%	0.0%	9.9%	-0.1%
8	x_fur_ww	0.92		-5.9%	-5.9%	-10.0%	5.9%	9.1%	-0.2%	-2.9%	-5.9%
9	x_fur_rf	1.00		0.0%	0.0%	0.0%	0.0%	0.0%	1.0%	0.0%	0.0%
10	x_fur_fe	1.00		-0.1%	-0.1%	-0.2%	0.1%	-0.1%	0.0%	10.2%	-0.1%
11	d_fa	800.80	µm	0.0%	0.0%	0.0%	0.0%	0.0%	0.0%	0.0%	0.0%
12	M_flame	0.52		-73.0%	-73.0%	54.0%	73.0%	64.4%	2.1%	27.3%	-73.0%
13	cp_ash	1200.00	J/kg K	0.0%	0.0%	0.0%	0.0%	0.0%	0.0%	0.0%	0.0%
				100.0%	100.0%	100.0%	100.0%	100.0%	100.0%	100.0%	100.0%

Table F-1.6: *Case Study 2 (100 t/h) – Projected method sensitivity at 2% perturbation.*

100 t/h Sensitivity - 2%											
	Parameter	Value	Unit	T_fe	h_fg_fe	T_g	Q_dot_fur	Q_dot_ww	Q_dot_rf	Q_dot_fe	Q_dot_fg_fe
				K	kJ/kgK	K	kW	kW	kW	kW	kW
1	eta_fe	0.80		0.0%	0.0%	0.0%	0.0%	-0.9%	0.0%	19.5%	0.0%
2	beta_fe	1.00		0.0%	0.0%	0.0%	0.0%	-0.6%	0.0%	12.5%	0.0%
3	epsilon_g	0.51		-15.4%	-15.4%	-26.3%	15.4%	13.6%	0.4%	5.7%	-15.4%
4	eta_rf	0.64		0.0%	0.0%	0.0%	0.0%	0.0%	2.3%	0.0%	0.0%
5	xi_fur_ww	0.60		-5.4%	-5.4%	-9.3%	5.4%	11.0%	-0.9%	-11.8%	-5.4%
6	xi_fur_rf	0.10		0.0%	0.0%	-0.1%	0.0%	0.0%	93.1%	-0.1%	0.0%
7	xi_fur_fe	1.00		-0.1%	-0.1%	-0.1%	0.1%	-0.2%	0.0%	9.9%	-0.1%
8	x_fur_ww	0.92		-5.9%	-5.9%	-10.0%	5.9%	9.1%	-0.2%	-2.9%	-5.9%
9	x_fur_rf	1.00		0.0%	0.0%	0.0%	0.0%	0.0%	1.0%	0.0%	0.0%
10	x_fur_fe	1.00		-0.1%	-0.1%	-0.2%	0.1%	-0.1%	0.0%	10.2%	-0.1%
11	d_fa	800.80	um	0.0%	0.0%	0.0%	0.0%	0.0%	0.0%	0.0%	0.0%
12	M_flame	0.52		-73.1%	-73.1%	53.9%	73.1%	64.5%	2.1%	27.3%	-73.1%
13	cp_ash	1200.00	J/kg K	0.0%	0.0%	0.0%	0.0%	0.0%	0.0%	0.0%	0.0%
				100.0%	100.0%	100.0%	100.0%	100.0%	100.0%	100.0%	100.0%

Table F-1.7: *Case Study 2 (80 t/h) – Projected method sensitivity at 1% perturbation.*

80t/h Sensitivity - 1%											
	Parameter	Value	Unit	T_fe	h_fg_fe	T_g	Q_dot_fur	Q_dot_ww	Q_dot_rf	Q_dot_fe	Q_dot_fg_fe
				K	kJ/kgK	K	kW	kW	kW	kW	kW
1	eta_fe	0.800		0.0%	0.0%	0.0%	0.0%	-1.0%	0.0%	19.9%	0.0%
2	beta_fe	1.000		0.0%	0.0%	0.0%	0.0%	-0.6%	0.0%	12.8%	0.0%
3	epsilon_g	0.506		-14.7%	-14.7%	-27.4%	14.7%	12.8%	0.4%	5.2%	-14.7%
4	eta_rf	0.641		0.0%	0.0%	0.0%	0.0%	0.0%	2.3%	0.0%	0.0%
5	xi_fur_ww	0.600		-5.7%	-5.7%	-10.6%	5.7%	11.6%	-0.9%	-12.4%	-5.7%
6	xi_fur_rf	0.100		0.0%	0.0%	-0.1%	0.0%	0.0%	93.2%	-0.1%	0.0%
7	xi_fur_fe	1.000		-0.1%	-0.1%	-0.1%	0.1%	-0.2%	0.0%	10.1%	-0.1%
8	x_fur_ww	0.916		-5.9%	-5.9%	-11.0%	5.9%	9.3%	-0.2%	-3.2%	-5.9%
9	x_fur_rf	1.000		0.0%	0.0%	0.0%	0.0%	0.0%	1.0%	0.0%	0.0%
10	x_fur_fe	1.000		-0.1%	-0.1%	-0.2%	0.1%	-0.1%	0.0%	10.4%	-0.1%
11	d_fa	800.8	um	0.0%	0.0%	0.0%	0.0%	0.0%	0.0%	0.0%	0.0%
12	M_flame	0.520		-73.5%	-73.5%	50.6%	73.5%	64.3%	1.9%	25.9%	-73.5%
13	cp_ash	1200.000	J/kg K	0.0%	0.0%	0.0%	0.0%	0.0%	0.0%	0.0%	0.0%
				100.0%	100.0%	100.0%	100.0%	100.0%	100.0%	100.0%	100.0%

Table F-1.8: *Case Study 2 (65 t/h) – Projected method sensitivity at 1% perturbation.*

65 t/h Sensitivity - 1%											
	Parameter	Value	Unit	T_fe	h_fg_fe	T_g	Q_dot_fur	Q_dot_ww	Q_dot_rf	Q_dot_fe	Q_dot_fg_fe
				K	kJ/kgK	K	kW	kW	kW	kW	kW
1	eta_fe	0.80		0.0%	0.0%	0.0%	0.0%	-1.1%	0.0%	20.5%	0.0%
2	beta_fe	1.00		0.0%	0.0%	0.0%	0.0%	-0.7%	0.0%	13.1%	0.0%
3	epsilon_g	0.51		-14.0%	-14.0%	-28.8%	14.0%	12.1%	0.3%	4.6%	-14.0%
4	eta_rf	0.64		0.0%	0.0%	0.0%	0.0%	0.0%	2.3%	0.0%	0.0%
5	xi_fur_ww	0.60		-5.9%	-5.9%	-12.1%	5.9%	12.1%	-0.9%	-13.0%	-5.9%
6	xi_fur_rf	0.10		0.0%	0.0%	-0.1%	0.0%	0.0%	93.4%	-0.1%	0.0%
7	xi_fur_fe	1.00		-0.1%	-0.1%	-0.2%	0.1%	-0.2%	0.0%	10.3%	-0.1%
8	x_fur_ww	0.92		-6.0%	-6.0%	-12.2%	6.0%	9.5%	-0.3%	-3.5%	-6.0%
9	x_fur_rf	1.00		0.0%	0.0%	0.0%	0.0%	0.0%	1.0%	0.0%	0.0%
10	x_fur_fe	1.00		-0.1%	-0.1%	-0.3%	0.1%	-0.1%	0.0%	10.6%	-0.1%
11	d_fa	800.80	um	0.0%	0.0%	0.0%	0.0%	0.0%	0.0%	0.0%	0.0%
12	M_flame	0.52		-73.9%	-73.9%	46.4%	73.9%	64.1%	1.8%	24.3%	-73.9%
13	cp_ash	1200.00	J/kg K	0.0%	0.0%	0.0%	0.0%	0.0%	0.0%	0.0%	0.0%
				100.0%	100.0%	100.0%	100.0%	100.0%	100.0%	100.0%	100.0%

F.2 Direct Method

Table F-2.1: *Case Study 1 (45 t/h) – Direct method sensitivity at 1% perturbation.*

45 t/h Sensitivity - 1%											
	Parameter	Value	Unit	T_fe	T_w	h_fg_fe	Q_dot_fur	Q_dot_fe	Q_dot_fg_fe	Q_dot_ww	Q_dot_rf
				K	K	kJ/kg	kW	kW	kW	kW	kW
1	epsilon_gp	0.42		-82.0%	62.4%	-82.0%	82.0%	-13.9%	-82.0%	82.8%	54.5%
2	epsilon_gp_hx	0.42		-1.1%	-0.5%	-1.1%	1.1%	68.5%	-1.1%	-0.6%	-0.4%
3	alpha_gp	0.52		2.1%	-1.6%	2.1%	-2.1%	0.4%	2.1%	-2.1%	-1.4%
4	alpha_gp_hx	0.48		0.1%	0.0%	0.1%	-0.1%	-6.8%	0.1%	0.1%	0.0%
5	k_fo	1.00	W/mK	-0.1%	-24.7%	-0.1%	0.1%	0.0%	-0.1%	0.1%	-20.7%
6	k_tw	47.00	W/mK	0.0%	0.0%	0.0%	0.0%	0.0%	0.0%	0.0%	0.0%
7	k_rf	1.40	W/mK	0.0%	0.0%	0.0%	0.0%	0.0%	0.0%	0.0%	13.5%
8	h_i	20000.00	W/m2K	0.0%	0.0%	0.0%	0.0%	0.0%	0.0%	0.0%	0.0%
9	x_fur_ww	0.92		-7.8%	6.0%	-7.8%	7.8%	-1.3%	-7.8%	7.9%	5.2%
10	x_fur_rf	1.00		-0.2%	0.2%	-0.2%	0.2%	0.0%	-0.2%	0.2%	0.2%
11	x_fur_fe	1.00		-0.5%	0.0%	-0.5%	0.5%	5.3%	-0.5%	0.0%	0.0%
12	d_fa	20.00	um	0.0%	0.0%	0.0%	0.0%	0.0%	0.0%	0.0%	0.0%
13	T_sat	558.15	K	0.0%	0.0%	0.0%	0.0%	0.0%	0.0%	0.0%	0.0%
14	cp_ash	1200.00	J/kg K	0.0%	0.0%	0.0%	0.0%	0.0%	0.0%	0.0%	0.0%
15	T_w_hx	924.15	K	0.0%	0.0%	0.0%	0.0%	0.0%	0.0%	0.0%	0.0%
16	epsilon_w	0.80		-6.0%	4.6%	-6.0%	6.0%	-1.0%	-6.0%	6.1%	4.0%
17	epsilon_w_hx	0.80		0.0%	0.0%	0.0%	0.0%	2.7%	0.0%	0.0%	0.0%
				100.0%	100.0%	100.0%	100.0%	100.0%	100.0%	100.0%	100.0%

Table F-2.2: *Case Study 1 (45 t/h) – Direct method sensitivity at 2% perturbation.*

45 t/h Sensitivity - 2%											
	Parameter	Value	Unit_x	T_fe	T_w	h_fg_fe	Q_dot_fur	Q_dot_fe	Q_dot_fg_fe	Q_dot_ww	Q_dot_rf
				K	K	kJ/kg	kW	kW	kW	kW	kW
1	epsilon_gp	0.42		-82.0%	62.6%	-82.0%	82.0%	-13.8%	-82.0%	82.8%	54.5%
2	epsilon_gp_hx	0.42		-1.1%	-0.5%	-1.1%	1.1%	68.6%	-1.1%	-0.6%	-0.4%
3	alpha_gp	0.52		2.1%	-1.6%	2.1%	-2.1%	0.4%	2.1%	-2.2%	-1.4%
4	alpha_gp_hx	0.48		0.1%	0.0%	0.1%	-0.1%	-6.8%	0.1%	0.1%	0.0%
5	k_fo	1.00	W/mK	0.0%	-24.5%	0.0%	0.0%	0.0%	0.0%	0.1%	-20.5%
6	k_tw	47.00	W/mK	0.0%	0.0%	0.0%	0.0%	0.0%	0.0%	0.0%	0.0%
7	k_rf	1.40	W/mK	0.0%	0.0%	0.0%	0.0%	0.0%	0.0%	0.0%	13.6%
8	h_i	20000.00	W/m2K	0.0%	0.0%	0.0%	0.0%	0.0%	0.0%	0.0%	0.0%
9	x_fur_ww	0.92		-7.8%	6.0%	-7.8%	7.8%	-1.3%	-7.8%	7.9%	5.2%
10	x_fur_rf	1.00		-0.2%	0.2%	-0.2%	0.2%	0.0%	-0.2%	0.2%	0.2%
11	x_fur_fe	1.00		-0.5%	0.0%	-0.5%	0.5%	5.3%	-0.5%	0.0%	0.0%
12	d_fa	20.00	um	0.0%	0.0%	0.0%	0.0%	0.0%	0.0%	0.0%	0.0%
13	T_sat	558.15	K	0.0%	0.0%	0.0%	0.0%	0.0%	0.0%	0.0%	0.0%
14	cp_ash	1200.00	J/kg K	0.0%	0.0%	0.0%	0.0%	0.0%	0.0%	0.0%	0.0%
15	T_w_hx	924.15	K	0.0%	0.0%	0.0%	0.0%	0.0%	0.0%	0.0%	0.0%
16	epsilon_w	0.80		-6.0%	4.6%	-6.0%	6.0%	-1.0%	-6.0%	6.1%	4.0%
17	epsilon_w_hx	0.80		0.0%	0.0%	0.0%	0.0%	2.7%	0.0%	0.0%	0.0%
				100.0%	100.0%	100.0%	100.0%	100.0%	100.0%	100.0%	100.0%

Table F-2.3: *Case Study 1 (36 t/h) – Direct method sensitivity at 1% perturbation.*

36 t/h Sensitivity - 1%											
	Parameter	Value	Unit	T_fe	T_w	h_fg_fe	Q_dot_fur	Q_dot_fe	Q_dot_fg_fe	Q_dot_ww	Q_dot_rf
				K	K	kJ/kg	kW	kW	kW	kW	kW
1	epsilon_gp	0.42		-81.8%	59.8%	-81.8%	81.8%	-15.8%	-81.8%	82.4%	51.6%
2	epsilon_gp_hx	0.42		-1.1%	-0.6%	-1.1%	1.1%	66.0%	-1.1%	-0.8%	-0.5%
3	alpha_gp	0.52		2.2%	-1.6%	2.2%	-2.2%	0.4%	2.2%	-2.2%	-1.4%
4	alpha_gp_hx	0.48		0.1%	0.1%	0.1%	-0.1%	-7.8%	0.1%	0.1%	0.1%
5	k_fo	1.00	W/mK	0.0%	-27.4%	0.0%	0.0%	0.0%	0.0%	0.1%	-22.7%
6	k_tw	47.00	W/mK	0.0%	0.0%	0.0%	0.0%	0.0%	0.0%	0.0%	0.0%
7	k_rf	1.40	W/mK	0.0%	0.0%	0.0%	0.0%	0.0%	0.0%	0.0%	14.7%
8	h_i	20000.00	W/m2K	0.0%	0.0%	0.0%	0.0%	0.0%	0.0%	0.0%	0.0%
9	x_fur_ww	0.92		-7.9%	5.8%	-7.9%	7.9%	-1.5%	-7.9%	8.0%	5.0%
10	x_fur_rf	1.00		-0.2%	0.2%	-0.2%	0.2%	0.0%	-0.2%	0.2%	0.2%
11	x_fur_fe	1.00		-0.4%	0.0%	-0.4%	0.4%	4.7%	-0.4%	0.0%	0.0%
12	d_fa	0.00	um	0.0%	0.0%	0.0%	0.0%	0.0%	0.0%	0.0%	0.0%
13	T_sat	558.15	K	0.0%	0.0%	0.0%	0.0%	0.0%	0.0%	0.0%	0.0%
14	cp_ash	1200.00	J/kg K	0.0%	0.0%	0.0%	0.0%	0.0%	0.0%	0.0%	0.0%
15	T_w_hx	924.15	K	0.0%	0.0%	0.0%	0.0%	0.0%	0.0%	0.0%	0.0%
16	epsilon_w	0.80		-6.1%	4.5%	-6.1%	6.1%	-1.2%	-6.1%	6.1%	3.8%
17	epsilon_w_hx	0.80		0.0%	0.0%	0.0%	0.0%	2.4%	0.0%	0.0%	0.0%
				100.0%	100.0%	100.0%	100.0%	100.0%	100.0%	100.0%	100.0%

Table F-2.4: *Case Study 1 (27 t/h) – Direct method sensitivity at 1% perturbation.*

27t/h Sensitivity - 1%											
	Parameter	Value	Unit	T_fe	T_w	h_fg_fe	Q_dot_fur	Q_dot_fe	Q_dot_fg_fe	Q_dot_ww	Q_dot_rf
				K	K	kJ/kg	kW	kW	kW	kW	kW
1	epsilon_gp	0.42		-81.9%	57.1%	-81.9%	81.9%	-18.1%	-81.9%	82.2%	48.5%
2	epsilon_gp_hx	0.42		-1.1%	-0.8%	-1.1%	1.1%	63.0%	-1.1%	-1.1%	-0.7%
3	alpha_gp	0.51		2.3%	-1.6%	2.3%	-2.3%	0.5%	2.3%	-2.3%	-1.4%
4	alpha_gp_hx	0.47		0.2%	0.1%	0.2%	-0.2%	-9.5%	0.2%	0.2%	0.1%
5	k_fo	1.00	W/mK	0.0%	-30.5%	0.0%	0.0%	0.0%	0.0%	0.0%	-25.0%
6	k_tw	47.00	W/mK	0.0%	0.0%	0.0%	0.0%	0.0%	0.0%	0.0%	0.0%
7	k_rf	1.40	W/mK	0.0%	0.0%	0.0%	0.0%	0.0%	0.0%	0.0%	16.0%
8	h_i	20000.00	W/m2K	0.0%	0.0%	0.0%	0.0%	0.0%	0.0%	0.0%	0.0%
9	x_fur_ww	0.92		-7.9%	5.5%	-7.9%	7.9%	-1.7%	-7.9%	7.9%	4.7%
10	x_fur_rf	1.00		-0.2%	0.2%	-0.2%	0.2%	-0.1%	-0.2%	0.2%	0.1%
11	x_fur_fe	1.00		-0.4%	0.0%	-0.4%	0.4%	3.8%	-0.4%	0.0%	0.0%
12	d_fa	20.00	um	0.0%	0.0%	0.0%	0.0%	0.0%	0.0%	0.0%	0.0%
13	T_sat	558.15	K	0.0%	0.0%	0.0%	0.0%	0.0%	0.0%	0.0%	0.0%
14	cp_ash	1200.00	J/kg K	0.0%	0.0%	0.0%	0.0%	0.0%	0.0%	0.0%	0.0%
15	T_w_hx	924.15	K	0.0%	0.0%	0.0%	0.0%	0.0%	0.0%	0.0%	0.0%
16	epsilon_w	0.80		-5.9%	4.1%	-5.9%	5.9%	-1.3%	-5.9%	5.9%	3.5%
17	epsilon_w_hx	0.80		0.0%	0.0%	0.0%	0.0%	1.9%	0.0%	0.0%	0.0%
				100.0%	100.0%	100.0%	100.0%	100.0%	100.0%	100.0%	100.0%

Table F-2.5: *Case Study 2 (100 t/h) – Direct method sensitivity at 1% perturbation.*

100t/h Sensitivity - 1%											
	Parameter	Value	Unit	T_fe	T_w	h_fg_fe	Q_dot_fur	Q_dot_fe	Q_dot_fg_fe	Q_dot_ww	Q_dot_rf
				K	K	kJ/kg	kW	kW	kW	kW	kW
1	epsilon_gp	0.49		-73.5%	50.4%	-73.5%	73.5%	-14.5%	-73.5%	74.0%	42.5%
2	epsilon_gp_hx	0.49		-0.7%	-0.4%	-0.7%	0.7%	62.5%	-0.7%	-0.5%	-0.3%
3	alpha_gp	0.63		1.9%	-1.3%	1.9%	-1.9%	0.4%	1.9%	-1.9%	-1.1%
4	alpha_gp_hx	0.58		0.1%	0.0%	0.1%	-0.1%	-5.8%	0.1%	0.1%	0.0%
5	k_fo	1.00	W/mK	0.0%	-31.9%	0.0%	0.0%	0.0%	0.0%	0.0%	-26.0%
6	k_tw	47.00	W/mK	0.0%	0.0%	0.0%	0.0%	0.0%	0.0%	0.0%	0.0%
7	k_rf	1.40	W/mK	0.0%	0.0%	0.0%	0.0%	0.0%	0.0%	0.0%	16.6%
8	h_i	20000.00	W/m2K	0.0%	0.0%	0.0%	0.0%	0.0%	0.0%	0.0%	0.0%
9	x_fur_ww	0.92		-12.4%	8.5%	-12.4%	12.4%	-2.5%	-12.4%	12.5%	7.2%
10	x_fur_rf	1.00		-0.1%	0.1%	-0.1%	0.1%	0.0%	-0.1%	0.1%	0.0%
11	x_fur_fe	1.00		-0.4%	0.0%	-0.4%	0.4%	7.2%	-0.4%	0.0%	0.0%
12	d_fa	800.80	um	0.0%	0.0%	0.0%	0.0%	0.0%	0.0%	0.0%	0.0%
13	T_sat	509.10	K	0.0%	0.0%	0.0%	0.0%	0.0%	0.0%	0.0%	0.0%
14	cp_ash	1200.00	J/kg K	0.0%	0.0%	0.0%	0.0%	0.0%	0.0%	0.0%	0.0%
15	T_w_hx	872.80	K	0.0%	0.0%	0.0%	0.0%	0.0%	0.0%	0.0%	0.0%
16	epsilon_w	0.80		-10.8%	7.4%	-10.8%	10.8%	-2.1%	-10.8%	10.9%	6.3%
17	epsilon_w_hx	0.80		-0.1%	0.0%	-0.1%	0.1%	5.0%	-0.1%	0.0%	0.0%
				100.0%	100.0%	100.0%	100.0%	100.0%	100.0%	100.0%	100.0%

Table F-2.6: *Case Study 2 (100 t/h) – Direct method sensitivity at 2% perturbation.*

100t/h Sensitivity - 2%											
	Parameter	Value	Unit	T_fe	T_w	h_fg_fe	Q_dot_fur	Q_dot_fe	Q_dot_fg_fe	Q_dot_ww	Q_dot_rf
				K	K	kJ/kg	kW	kW	kW	kW	kW
1	epsilon_gp	0.49		-73.5%	50.6%	-73.5%	73.5%	-14.4%	-73.5%	74.0%	42.6%
2	epsilon_gp_hx	0.49		-0.7%	-0.4%	-0.7%	0.7%	62.6%	-0.7%	-0.5%	-0.3%
3	alpha_gp	0.63		1.9%	-1.3%	1.9%	-1.9%	0.4%	1.9%	-1.9%	-1.1%
4	alpha_gp_hx	0.58		0.1%	0.0%	0.1%	-0.1%	-5.8%	0.1%	0.1%	0.0%
5	k_fo	1.00	W/mK	0.0%	-31.7%	0.0%	0.0%	0.0%	0.0%	0.0%	-25.7%
6	k_tw	47.00	W/mK	0.0%	0.0%	0.0%	0.0%	0.0%	0.0%	0.0%	0.0%
7	k_rf	1.40	W/mK	0.0%	0.0%	0.0%	0.0%	0.0%	0.0%	0.0%	16.7%
8	h_i	20000.00	W/m2K	0.0%	0.0%	0.0%	0.0%	0.0%	0.0%	0.0%	0.0%
9	x_fur_ww	0.92		-12.4%	8.6%	-12.4%	12.4%	-2.4%	-12.4%	12.5%	7.2%
10	x_fur_rf	1.00		-0.1%	0.1%	-0.1%	0.1%	0.0%	-0.1%	0.1%	0.0%
11	x_fur_fe	1.00		-0.4%	0.0%	-0.4%	0.4%	7.2%	-0.4%	0.0%	0.0%
12	d_fa	800.80	um	0.0%	0.0%	0.0%	0.0%	0.0%	0.0%	0.0%	0.0%
13	T_sat	509.10	K	0.0%	0.0%	0.0%	0.0%	0.0%	0.0%	0.0%	0.0%
14	cp_ash	1200.00	J/kg K	0.0%	0.0%	0.0%	0.0%	0.0%	0.0%	0.0%	0.0%
15	T_w_hx	872.80	K	0.0%	0.0%	0.0%	0.0%	0.0%	0.0%	0.0%	0.0%
16	epsilon_w	0.80		-10.8%	7.4%	-10.8%	10.8%	-2.1%	-10.8%	10.8%	6.2%
17	epsilon_w_hx	0.80		-0.1%	0.0%	-0.1%	0.1%	4.9%	-0.1%	0.0%	0.0%
				100.0%	100.0%	100.0%	100.0%	100.0%	100.0%	100.0%	100.0%

Table F-2.7: *Case Study 2 (80 t/h) – Direct method sensitivity at 1% perturbation.*

80 t/h Sensitivity - 1%											
	Parameter	Value	Unit	T_fe	T_w	h_fg_fe	Q_dot_fur	Q_dot_fe	Q_dot_fg_fe	Q_dot_ww	Q_dot_rf
				K	K	kJ/kg	kW	kW	kW	kW	kW
1	epsilon_gp	0.50		-72.6%	47.2%	-72.6%	72.6%	-16.2%	-72.6%	73.0%	39.2%
2	epsilon_gp_hx	0.50		-0.7%	-0.5%	-0.7%	0.7%	60.1%	-0.7%	-0.7%	-0.4%
3	alpha_gp	0.63		2.0%	-1.3%	2.0%	-2.0%	0.4%	2.0%	-2.0%	-1.1%
4	alpha_gp_hx	0.58		0.1%	0.1%	0.1%	-0.1%	-6.9%	0.1%	0.1%	0.0%
5	k_fo	1.00	W/mK	0.0%	-35.4%	0.0%	0.0%	0.0%	0.0%	0.0%	-28.3%
6	k_tw	47.00	W/mK	0.0%	0.0%	0.0%	0.0%	0.0%	0.0%	0.0%	0.0%
7	k_rf	1.40	W/mK	0.0%	0.0%	0.0%	0.0%	0.0%	0.0%	0.0%	18.0%
8	h_i	20000.00	W/m2K	0.0%	0.0%	0.0%	0.0%	0.0%	0.0%	0.0%	0.0%
9	x_fur_ww	0.92		-12.8%	8.3%	-12.8%	12.8%	-2.8%	-12.8%	12.8%	6.9%
10	x_fur_rf	1.00		-0.1%	0.1%	-0.1%	0.1%	0.0%	-0.1%	0.1%	0.0%
11	x_fur_fe	1.00		-0.4%	0.0%	-0.4%	0.4%	6.4%	-0.4%	0.0%	0.0%
12	d_fa	0.00	um	0.0%	0.0%	0.0%	0.0%	0.0%	0.0%	0.0%	0.0%
13	T_sat	509.33	K	0.0%	0.0%	0.0%	0.0%	0.0%	0.0%	0.0%	0.0%
14	cp_ash	1200.00	J/kg K	0.0%	0.0%	0.0%	0.0%	0.0%	0.0%	0.0%	0.0%
15	T_w_hx	872.80	K	0.0%	0.0%	0.0%	0.0%	0.0%	0.0%	0.0%	0.0%
16	epsilon_w	0.80		-11.2%	7.3%	-11.2%	11.2%	-2.5%	-11.2%	11.3%	6.1%
17	epsilon_w_hx	0.80		-0.1%	0.0%	-0.1%	0.1%	4.5%	-0.1%	-0.1%	0.0%
				100.0%	100.0%	100.0%	100.0%	100.0%	100.0%	100.0%	100.0%

Table F-2.8: *Case Study 2 (65 t/h) – Direct method sensitivity at 1% perturbation.*

65 t/h Sensitivity - 1%											
	Parameter	Value	Unit	T_fe	T_w	h_fg_fe	Q_dot_fur	Q_dot_fe	Q_dot_fg_fe	Q_dot_ww	Q_dot_rf
				K	K	kJ/kg	kW	kW	kW	kW	kW
1	epsilon_gp	0.50		-72.0%	43.9%	-72.0%	72.0%	-17.9%	-72.0%	72.1%	35.9%
2	epsilon_gp_hx	0.50		-0.7%	-0.6%	-0.7%	0.7%	57.7%	-0.7%	-0.9%	-0.5%
3	alpha_gp	0.63		2.1%	-1.3%	2.1%	-2.1%	0.5%	2.1%	-2.1%	-1.0%
4	alpha_gp_hx	0.58		0.1%	0.1%	0.1%	-0.1%	-8.2%	0.1%	0.1%	0.1%
5	k_fo	1.00	W/mK	0.0%	-39.1%	0.0%	0.0%	0.0%	0.0%	0.0%	-30.8%
6	k_tw	47.00	W/mK	0.0%	0.0%	0.0%	0.0%	0.0%	0.0%	0.0%	0.0%
7	k_rf	1.40	W/mK	0.0%	0.0%	0.0%	0.0%	0.0%	0.0%	0.0%	19.5%
8	h_i	20000.00	W/m2K	0.0%	0.0%	0.0%	0.0%	0.0%	0.0%	0.0%	0.0%
9	x_fur_ww	0.92		-13.0%	7.9%	-13.0%	13.0%	-3.2%	-13.0%	13.0%	6.5%
10	x_fur_rf	1.00		-0.1%	0.1%	-0.1%	0.1%	0.0%	-0.1%	0.1%	0.0%
11	x_fur_fe	1.00		-0.4%	0.0%	-0.4%	0.4%	5.5%	-0.4%	0.0%	0.0%
12	d_fa	800.80	um	0.0%	0.0%	0.0%	0.0%	0.0%	0.0%	0.0%	0.0%
13	T_sat	509.33	K	0.0%	0.0%	0.0%	0.0%	0.0%	0.0%	0.0%	0.0%
14	cp_ash	1200.00	J/kg K	0.0%	0.0%	0.0%	0.0%	0.0%	0.0%	0.0%	0.0%
15	T_w_hx	872.80	K	0.0%	0.0%	0.0%	0.0%	0.0%	0.0%	0.0%	0.0%
16	epsilon_w	0.80		-11.5%	7.0%	-11.5%	11.5%	-2.9%	-11.5%	11.5%	5.7%
17	epsilon_w_hx	0.80		0.0%	0.0%	0.0%	0.0%	4.0%	0.0%	-0.1%	0.0%
				100.0%	100.0%	100.0%	100.0%	100.0%	100.0%	100.0%	100.0%